

A study on the kinetics
of the phase transformation in silicon anodes
in lithium ion batteries

Shaghayegh Rezazadeh Kalehbasti

A dissertation submitted to the School of Engineering in partial fulfillment
of the requirements for the Degree of Doctor of Philosophy

Brown University
Providence, Rhode Island
May 2020

Copyright © 2020 Shaghayegh Rezazadeh Kalehbasti.

All rights reserved.

This dissertation by Shaghayegh Rezazadeh Kalehbasti is accepted in its present form by the School of engineering as satisfying the dissertation requirement for the degree of Doctor of Philosophy.

Date _____

Advisor, Pradeep R. Guduru

Recommended to the Graduate Council

Date _____

Reader, Allan F. Bower

Date _____

Reader, Humphrey J. Maris

Approved by the Graduate Council

Date _____

Dean of Graduate School, Andrew G. Campbell

Curriculum Vitae

Shaghayegh Rezazadeh Kalehbasti received her Bachelor of Science degree in Civil Engineering from Sharif University of Technology in Iran in June 2010. She continued her studies at the same university and received her Master of Science degree in Structural Engineering in June 2012. She started pursuing her graduated studies in the department of solid Mechanics at Brown University in August 2013. She served as a teaching assistant for multiple undergraduate and graduate level courses throughout her years at graduate school and taught the “Intro to engineering and design” course for the summer @ Brown program. She received her Master of Science in Mechanical Engineering in May 2015. Her research as a Doctoral student in the department of Solid Mechanics at Brown University was focused on the real time measurement and simulation of the microstructural evolution in the Li ion battery electrodes.

Journal Publications:

- Rezazadeh-Kalehbasti, S., Liu, L.W., Maris, H., Guduru, P. (2019). In situ measurement of phase boundary kinetics during initial lithiation of crystalline silicon through Picosecond Ultrasonics method. *Journal of Experimental Mechanics*. doi: 10.1007/s11340-018-00460-5.
- Rezazadeh-Kalehbasti, S., Gutkin, M. Y., Shodja, H. M. (2014). Wedge disclinations in the shell of a core-shell nanowire within the surface/interface elasticity. *Mechanics of Materials* 68, 45-63.
- Gutkin, M. Y., Rezazadeh-Kalehbasti, S., Shodja, H. M. (2013). Surface/interface effects on elastic behavior of an edge dislocation in the shell of a core-shell nanowire. *European Journal of Mechanics-A/Solids* 41, 86-100.
- Shodja, H. M., Rezazadeh-Kalehbasti, S., Gutkin, M. Y. (2013). Effect of interface stress on elastic behavior of a wedge disclination dipole in a nanowire embedded to an infinite matrix. *Journal of the Mechanical Behavior of Materials* 22 (5-6), 161-168.

Acknowledgements

I am really grateful that I had Prof. Guduru as my PhD advisor. He has been a magnificent advisor with immense expertise in research and patience towards guiding students. The fruition of this work was not possible without his extensive encouragement and assistance. I also want to thank Prof. Maris for his guidance and mentorship on the picosecond ultrasonics project and introducing me to the realm of laser optics. I sincerely appreciate Prof. Bower for advising me on the phase-field modeling of the phase propagation problem. His enlightening directions made this project feasible.

This work would not have been finished without the help from my fellow researchers at Brown. I am grateful to Dr. Naba Karan for introducing me to the world of experiments and electrochemistry. I would like to thank Dr. Liwei Liu for supervising me on the picosecond ultrasonics technique and his assistance on the integration of this method with the electrochemical system. Special thanks to Dr. Insun Yoon for his perpetual help and encouragement at all levels during my PhD.

I would like to thank my family for all their love and support throughout these years. My friends were the main source of daily moral power. Overcoming the ups and downs of the graduate student's life was not imaginable without them. It was a long journey and I could not have come so far without the generous help of these people along the way.

Table of Contents

List of Tables	viii
List of Figures	ix
1. Introduction.....	1
1.1. Electrode materials in LIB's	2
1.1.1. Silicon anodes	4
1.1.2. Experimental and computational analysis of the lithiation in silicon anodes	6
1.2. Overview of the thesis.....	11
2. Picosecond ultrasonics technique.....	13
2.1. Introduction.....	13
2.2. Picosecond ultrasonics – Optical generation.....	14
2.3. Picosecond ultrasonics – Optical detection.....	24
2.4. Setting up the apparatus for picosecond ultrasonics	26
2.4.1. Adjustments on the laser beam	27
2.4.2. The probe beam.....	29
2.4.3. The pump beam.....	33
2.5. Summary	37
2.6. Appendix.....	37
2.6.1. Steps for aligning the probe beam parallel to the translation stage.....	37
2.6.2. Steps for positioning the probe beam normal to the lens (L1)	39
2.6.3. Optimizing the initial jump at zero probe delay time	40
3. In Situ measurement of the kinetics of phase transformation through picosecond ultrasonics and atomic force microscopy.....	42
3.1. Introduction.....	42
3.2. Experimental technique.....	44
3.2.1. Picosecond ultrasonics measurements- Benchmark experiment.....	44
3.2.2. Signal processing, data analysis, and derivation of the kinetic parameters	48

3.2.3.	Comparison between the velocity of the phase boundary propagation through different crystallographic planes.....	56
3.3.	Atomic force microscopy measurements	64
3.4.	Conclusions.....	72
3.5.	Appendix.....	74
3.5.1.	Deal-Grove model for the diffusion of Li in α -Li _x Si.....	74
3.5.2.	Evolution of potential/current during galvanostatic/potentiostatic measurements	76
3.5.3.	Fabrication procedure for AFM samples	78
4.	Phase-field modeling of the phase transformation in Si due to diffusion of Li	80
4.1.	Introduction.....	80
4.2.	Model of a half cell with crystalline Si anode.....	83
4.2.1.	Mechanical Deformation.....	84
4.2.2.	Thermodynamics and kinetics of Li transport- a phase field approach	87
4.2.3.	A general sharp interface model	89
4.2.4.	Electrochemistry at the electrode/ electrolyte interface	95
4.3.	Model Behavior	98
4.3.1.	Free Energy	101
4.3.2.	Lithium mobility in the lithiated layer	103
4.3.3.	Exchange current density, interface mobility and velocity of the phase boundary.....	106
4.3.4.	Chemical potential, concentration, stress and strain profiles	111
4.3.5.	Variations in the model parameters.....	119
4.3.6.	Energy dissipation in the cell	126
4.3.7.	Rate-limiting processes during the lithiation of Si.....	129
4.2.	Conclusions.....	130
4.3.	Appendix.....	132
4.3.1.	Derivation of Cahn-Hilliard formulation	132
4.3.2.	Finite element implementation for the model equations.....	133
4.3.3.	The evolution of electrochemical and mechanical fields during lithiation of Si wafer with (100) and (110) orientations.....	139
5.	Summary and future works	140
5.1.	Summary	140
5.2.	Future works	142
	References.....	144

List of Tables

Table 1.1 comparison of the density, lithiated phase, specific capacity, and volume change of various anode materials ⁷	3
Table 3.1. Velocity of the phase boundary propagation during galvanostatic lithiation of c-Si with (100) and (110) orientations at 10, 20, and 30 $\mu\text{A}/\text{cm}^2$ and the average velocity of phase boundary propagation during potentiostatic lithiation of c-Si with (100) and (110) orientations at potential values of 80, 95, and 100 mV.	59
Table 3.2. Volumetric strain (ϵv) and Li content after the full lithiation of (100) and (110)-oriented Si at constant potentials of 80, 95, and 100 mV.....	71
Table 4.1. parameters used in defining the evolution of the biaxial modulus and the yield stress of silicon during lithiation.....	86
Table 4.2. phase field model parameters calibrated based on experimental results.....	102
Table 4.3. Comparison between the experimentally measured and computationally simulated values of the velocity of the phase boundary propagation normal to the {100} and {110} orientations during different galvanostatic and potentiostatic lithiation conditions. The velocities are reported in pm/s.	108

List of Figures

- Figure 1.1. Images of the phase boundary between c-Si and a-LixSi using a) ex situ SEM and b) ex situ TEM on partially lithiated Si wafers (Reproduced with permission.^[39] Copyright 2011, American Physical Society). c) HRTEM image of the phase boundary inside a partially lithiated Si nanowire showing the ledge mechanism for the phase boundary propagation. Reproduced with permission. ^[54] Copyright 2012, Macmillan Publishers Ltd. 6
- Figure 1.2. crack propagation during delithiation of Si wafers. a) SEM image of the surface of the wafer after delithiation, b) FIB cross section showing the cracks propagate into the crystalline Si layer. Image Reproduced with permission. ^[39] Copyright 2011, American Physical Society. 8
- Figure 1.3. SEM images of Si nanopillars with different axial orientations: $\langle 100 \rangle$, $\langle 110 \rangle$, and $\langle 111 \rangle$ on the first, second, and third columns, respectively. (a-c) show the pristine state of the nanopillars. (d-f) and (g-i) show the partially and fully lithiated morphology of the nanopillars. Scale bar is 200nm. Reproduced with permission. ^[60] Copyright 2011, American Chemical Society. 8
- Figure 2.1. Schematic of the picosecond ultrasonics measurement technique. The pump and probe light pulses are focused onto the same spot on the Al surface. The application of the pump light pulse results in the generation of an acoustic pulse. The change in the reflectivity due to the returning acoustic echo is detected with a time-delayed probe light pulse. 16
- Figure 2.2. (a) Picosecond ultrasonic setup; the position of the sample on the setup is marked with a red circle, (b) a closer look at the sample position. 18
- Figure 2.3. A schematic diagram of the basic setup for picosecond ultrasonics; the initial laser, pump, and probe laser pulses are shown in yellow, red, and blue, respectively. HWP – Half-wave plate, PBS – Polarized beam splitter, M – Mirror, EOM – Electro-optic modulator, L – Lens, BB – Beam blocker, RR – Retroreflector, NBS – Non-polarized beam splitter. 19
- Figure 2.4. Picosecond ultrasonic measurement on a thin silicon sample. The numbers in the boxes indicate the number of round trips of the echo inside the Si sample up to that time. Each round trip takes 1011 ps. “S” shows the simultaneous arrival of the pump and probe pulses at the surface of the sample and generation of the sound wave. The oscillations arise from the small amplitude sound pulse that propagates from the Al film into the epoxy. 21
- Figure 2.5. Comparison between (a) good and (b) bad quality of the Al film and bonding between the Al film and Si sample. The effects are significant in the heat diffusion properties and the signal-to-noise ratio. 24
- Figure 2.6. PU scan on a GaAs sample. The range of the probe delay time is chosen so that the arrival of two consecutive pump pulses at the surface are detected. Operating frequency of the laser (80 MHz) dictates

the temporal distance between the two pulses. The arrival time of the echo from the surface of this 500 μm thick wafer is beyond the time frame of this measurement. 27

Figure 2.7. (a) Collimation rack and (b) schematic of its operation. The input beam with a width y_1 and divergence angle θ_1 is modified to give an output beam with a width y_2 and divergence angle θ_2 28

Figure 2.8. Halfwave plate (HWP) followed by a polarized beam splitter to separate the pump and the probe beam based on their polarization. 29

Figure 2.9. (a) Placement of the retroreflectors (RR1 and RR2), polarized beamsplitter (PBS), mirrors (M), and temporary mirrors (T1 and T2). (b) larger view of the position of the mirrors. The order in which the probe beam sees the optics is PBS, M1, M2, RR1, M3, M4, RR1, M5, M6, RR2, M7, M8, RR2, M9. 30

Figure 2.10. Lens, CCD camera, and the screen used in the second setup for monitoring the characteristics of the beam spot after traveling through the second setup. 31

Figure 2.11. a) Apparatus and b) schematic of the last portion of the probe beam path. The beam must hit the lens (L1) and the sample at a normal angle of incidence. The ingoing beam is shown in blue and the reflected beam from the surface of the sample is shown in orange. The reflected beam is directed into a lens (not shown) followed by a photodiode. 33

Figure 2.12. Electro optic modulator (EOM) fixed on the optical table using a pitch and yaw platform. The output of the EOM must be optimized to produce modulated waves with a frequency of 1 MHz and maximum amplitude. 34

Figure 2.13. (a) Path of the pump beam towards the sample and (b) the schematic of the path. The angle and position of the pump beam are set so that its position on the surface of the sample coincides with the position of the focused probe beam while hitting lens L3 at a normal angle. 36

Figure 2.14. Front view of the retroreflector with the beam spots inside. To maximize the spacing between the mirrors, one strategy is to send beam inside the RR at spot 1, it will come out of spot 2; send it back in at spot 3, and it will finally come out from spot 4. 38

Figure 3.1. (a) Schematic of the sample used in PU measurements. (b) Cross-section of the custom-made cell designed for the PU studies. The images are not drawn to scale. 46

Figure 3.2. a photograph of the assembled cell. 46

Figure 3.3. Signal recorded from the PU measurement on a pristine Si sample. Arrows I, II, and III mark the initial jump, the second set of BO, and the arrival time of the echo reflected from the surface of the sample. 48

Figure 3.4. a) Lithiation profiles of a (100) oriented Si wafer, b) PU measurements corresponding to each lithiation step, and c) zoomed-in image from (b) indicating the arrival time of the echo; the black line corresponds to the pristine state of the Si wafer. The color of each lithiation step is matched with the corresponding PU measurement. The blue arrow indicates the arrival time of the echo in the pristine state. The signal profiles are stacked vertically for clarity and are not spaced to scale. 49

Figure 3.5. Data processing steps. The black line corresponds to the data acquired after the 3rd step of lithiation (S). The 6th order polynomial background fit (P) is shown in green. The olive line represents the data with background removed. After removing the background and oscillations, the final processed data (in blue) is demonstrating two peaks corresponding to the arrival times of the reflected echoes..... 50

Figure 3.6. Consecutive lithiation/PU measurements on a (100) Si sample. The cell is lithiated galvanostatically at $40 \mu\text{A}/\text{cm}^2$. The black curve corresponds to the pristine state. Beyond the initial state, the first echo is reflected from the interface of c-Si / a-Li_xSi and the second echo is reflected from the free surface of a-Li_xSi. Δtc is the advance in the echo arrival time due to consumption of c-Si and Δta is the travel time of the sound wave in a-Li_xSi layer after each step of lithiation. 51

Figure 3.7. Plots of sound wave velocity in a-Li_xSi layer measured in this work (v_a) and that calculated from the properties of a-Li_xSi from the literature^{75, 76} ($v_{a\text{-computed}}$) vs the thickness of crystalline Si consumed after each step of lithiation (h_c). Variations of x in Li_xSi with the thickness of consumed crystalline Si are shown with red circles 54

Figure 3.8. Thickness of crystalline silicon consumed (blue squares) and thickness of the amorphous lithiated silicon layer produced (red dots) vs the cumulative charge density for consecutive lithiation/ PU measurements on Si sample with (100) orientation 55

Figure 3.9. a) Consecutive lithiation/PU measurements on a (100) Si wafer lithiated at $20 \mu\text{A}/\text{cm}^2$ b) Thickness of crystalline Si with (110) and (100) orientations (in blue and red, respectively) consumed with lithiation time at three different current densities of 10, 20, and $30 \mu\text{A}/\text{cm}^2$ 58

Figure 3.10. Schematic of a steady-state diffusion of Li in a partially lithiated Si anode. The flux at the surface (j) and the current density (I) are constant during galvanostatic lithiation..... 60

Figure 3.11. (a) Schematic of the samples nanofabricated by etching of SOI wafers, (b) top view of the sample, and (c) cross-section of the custom-made cell designed for the in situ AFM studies. The images are not drawn to scale. 66

Figure 3.12. AFM scan of the topography of a Si strip a) at the pristine state and b) after full lithiation. . 68

Figure 3.13. Schematic of the steady-state model for moving phase boundary at the interface of a-Li_xSi and c-Si. Concentration profile is shown with red lines. C -, C_{eq} , and C_s are the concentration of Li at the a-Li_xSi/c-Si interface, equilibrium concentration at the interface of a-Li_xSi/c-Si, and solubility of Li in c-Si, respectively. 75

Figure 3.14. Evolution of potential during consecutive galvanostatic lithiation/PU measurements on (100) and (110) oriented Si wafers. 77

Figure 3.15. Evolution of current during potentiostatic lithiation/PU measurements on (100) and (110) oriented Si wafers. 77

Figure 3.16. fabrication process for creating a double-step stripe pattern on the AFM samples. Starting from an SOI wafer, multiple steps of photolithography and ICP etching are applied to create double-step features with 700 nm and 300 nm heights. The numbers on the red arrows refer to the steps explained in section

3.5.3. The photoresist layers deposited on the sample during photolithography are shown in green. The cross-sections of the samples are not drawn to scale. 79

Figure 4.1. Schematic representing the one-dimensional model of the Li-Si system. The total thickness of the sample is H . The crystalline Si electrode is partially lithiated. The c-Si part ahead of the phase boundary is shown in solid orange and the lithiated Li_xSi part behind the phase boundary is shown with dotted orange pattern. 84

Figure 4.2. Schematic representing the one-dimensional two-phase model for the diffusion of Li in partially lithiated crystalline Si. The amorphous and the crystalline phases are named the α and β , the phase boundary is at a distance “ a ” from the free surface and the thickness of the sample is H . The flux at the surface, behind and ahead of the interface and at $x=H$ are marked with j^0 , j^- , j^+ , and j^H , respectively. 90

Figure 4.3. Current and voltage evolution during galvanostatic, potentiostatic, and open-circuit experiments used to calibrate and determine the Cahn-Hilliard model parameters. 100

Figure 4.4. (a) Normalized homogeneous free energy and (b) its derivative based on calibrations for the free energy function. The energy minima are at $c = 0$ and 3.75 and the lower spinodal point is at $c = 0.8$ 103

Figure 4.5. Linear fit to the evolution of the potential with interface position during constant current experiments at $20 \mu\text{A}/\text{cm}^2$ on the (100) and (110) oriented Si wafers. 104

Figure 4.6. (a) Voltage evolution with state of charge during galvanostatic lithiation of (100) oriented Si at 10, 20, and $30 \mu\text{A}/\text{cm}^2$. (b) relation between the average value of the voltage at a specified state of charge (as shown in (a)) and the current density during constant current experiments on the (100) and (110) oriented Si. 105

Figure 4.7. comparison between experimental measurements (dashed lines) and model predictions (solid lines) for the voltage and current density profiles during lithiation normal to (100) planes. 110

Figure 4.8. comparison between experimental measurements (dashed lines) and model predictions (solid lines) for the voltage and current density profiles during lithiation normal to (110) planes. 110

Figure 4.9. Evolution in the (a, c) chemical potential, (b, d) concentration and stress profiles before ($t \leq 0.07$) and after nucleation during lithiation of Si normal to the {100} (a, b) and {110} (c, d) orientations. The dashed-purple arrows show the jump happening in the chemical potential and concentration near the surface of Si upon nucleation. The blue arrows mark the equilibrium concentration in the $a\text{-Li}_x\text{Si}$ layer. The compressive peaks in the stress at the phase boundary are pointed with pink arrows in (b) and (d). The elastic and plastic regions are indicated at time $t = 0.17$ hr in (b) and (d). The position of the phase boundary at different times is marked with crosses on the chemical potential profiles in (a) and (c). 114

Figure 4.10. The evolution in (a) chemical potential, (b) concentration, (c) biaxial stress, and (d) plastic strain at different stages of lithiation of Si wafer with (110) orientation. Snapshots during galvanostatic $0.2 < t < 7.7$ hr, first potentiostatic $12.7 < t < 17.7$ hr at 0.12 V, and second potentiostatic $22.7 < t < 27.7$ hr at 0.1 V are shown in blue, green, and red colors, respectively. 117

Figure 4.11. The evolution in (a) chemical potential, (b) concentration, (c) biaxial stress, and (d) plastic strain at different stages of lithiation of Si wafer with (100) orientation. Snapshots during galvanostatic $0.2 < t < 7.7$ hr, first potentiostatic $12.7 < t < 17.7$ hr at 0.12 V, and second potentiostatic $22.7 < t < 27.7$ hr at 0.1 V are shown in blue, green, and red colors, respectively..... 118

Figure 4.12. Effect of kappa on the sharpness of the interface. 120

Figure 4.13. Effect of the interface-mobility parameter and exchange current density on the prediction of the model for the electrochemistry of lithiation and comparison with the experimental measurements. (a) voltage profiles during the galvanostatic, first open-circuit, and first potentiostatic (voltage=0.1V) measurements and (b) current density profile during the first potentiostatic lithiation (voltage=0.1V). The experimental results are shown with dashed lines. 122

Figure 4.14. Effect of stress and viscoplastic parameters on the prediction of the model for the changes in (a) the voltage profiles during the galvanostatic lithiation and the first open circuit measurement and (b) the current density profiles during the first potentiostatic lithiation with Voltage=0.1 V. Experimental measurements are shown in dashed lines..... 124

Figure 4.15. Effect of stress exponent and plastic strain rate on (a) the chemical potential, (b) the biaxial stress, and (c) the plastic strain. All the snapshots are taken during the galvanostatic lithiation at $t=1.5$ hr. 125

Figure 4.16. The evolution in (a) chemical potential, (b) concentration, (c) biaxial stress, and (d) plastic strain at different stages of lithiation of Si wafer. $\langle 100 \rangle$ and $\langle 110 \rangle$ directions are shown in solid and dashed lines, respectively. Snapshots during galvanostatic $0.2 < t < 7.7$ hr, first potentiostatic $12.7 < t < 17.7$ hr at 0.12 V, and second potentiostatic $22.7 < t < 27.7$ hr at 0.1 V are shown in blue, green, and red colors, respectively. 139

1. Introduction

Lithium ion batteries (LIBs) have received substantial attention in the recent years due to their wide use in mobile electronics, electric vehicles and grid scale energy storage. LIBs are being used increasingly to meet multiple demands of the modern society such as moving the transportation sector from fossil fuel based internal combustion engines towards electric vehicles; and grid scale storage solutions in the evolving energy landscape where intermittent energy sources such as photovoltaic, wind and photothermal sources will have an increasing role. It has been well-recognized that further enhancements in the energy density, cycle life and calendar life of LIBs are critically needed to tip the economic scales in favor of rechargeable battery technologies in a broad range of applications. New materials are being explored for electrodes, electrolytes and separators, which could increase the energy density. At the same time, a great deal of effort is also devoted to understanding the degradation mechanisms that contribute to the performance degradation during the life of a battery. The degradation mechanisms are often complex, involving the chemistry, mechanics and materials aspects, requiring their study to be inherently interdisciplinary. The focus of this thesis* is on characterizing phase transformations and moving

* The contents of his thesis have appeared in an earlier publication1. Rezazadeh-Kalehbasti, S.; Liu, L. W.; Maris, H. J.; Guduru, P. R., In Situ Measurement of Phase Boundary Kinetics during Initial Lithiation of Crystalline Silicon through Picosecond Ultrasonics. *J. Experimental Mech.* **2019**. Copyright Society for Experimental Mechanics 2019

phase boundaries in LIB electrodes, which result from the electrochemical reactions between lithium (Li) and the electrode materials.

1.1. Electrode materials in LIB's

The positive electrodes (cathode) in commercial Li ion batteries are made of metal oxides and phosphates such as LiCoO_2 , $\text{Li}[\text{NiMnCo}]\text{O}_2$, LiMnO_2 , and LiFePO_4 . Graphite is a typical negative electrode (anode) materials in the present-day LIBs. During charging, Li from the positive electrode migrates across the electrochemical cell and intercalates into the negative electrode. In case of graphite, Li atoms occupy the interstitial sites between the graphene layers. This reversible intercalation between the crystallographic planes of the host material does not break the interplanar covalent bonds of the host matrix nor forms new covalent bonds. Therefore, the atomic structure of the host remains undisturbed during de/insertion of Li from the anode²⁻⁴. Graphite anodes offer good capacity retention and small structural changes during dis/charge cycles. However, in a fully lithiated graphite, the ratio of Li to carbon atoms is only 1:6, which corresponds to a specific capacity⁵ of 372 mAh/g. Another group of materials that have been known to be promising candidates for anodes are the elements in group IV, namely, Si, Ge, and Sn. The storage mechanism of these materials is different from that of intercalating electrodes. Insertion of Li exhibits volume changes in the electrode that could be due to changes in the interplanar spacing, as in the case of intercalating electrodes, or rearrangements in the structure, as reported for the

case of group IV elements⁶. Table 1.1 provides a comparison between the specific capacity and the volume change of carbon, Si, and Sn anodes⁷.

Table 1.1 comparison of the density, lithiated phase, specific capacity, and volume change of various anode materials⁷

<i>Material</i>	<i>C</i>	<i>Si</i>	<i>Sn</i>
<i>Density (g/cm³)</i>	2.25	2.33	7.29
<i>Lithiated phase</i>	LiC ₆	Li _{4.4} Si	Li _{4.4} Sn
<i>Specific capacity (mAh/g)</i>	372	4200	994
<i>Volume change (%)</i>	12	320	260

In contrast to graphite, the group IV elements form alloys with Li, therefore, the specific capacity of anodes made of these materials is not limited by the structure of the host. The resulting alloys can take up to 4.4 Li atoms per atom of the host material that gives a lithium packing density close to that of metallic lithium. The theoretical volume changes associated with these alloys is about 2 or 3 times the original volume⁸. The cycles of Li extraction/insertion result in extreme volume contraction/expansions that lead to acute decay in capacity retention. On one hand, the large strain in the brittle structure of the anode leads to fracture and electrical isolation of parts of the electrode material, thus, converting a previously active mass to an inactive one. On the other hand, volume expansion and fracture expose fresh surfaces to the electrolyte. These surfaces must be stabilized by the formation of solid electrolyte interphase (SEI)⁹. The SEI layer decreases the ionic permeability of the system and the Li consumed in the formation of SEI does not return to the dis/charge cycle. These aggravating effects pose obstacles in practical realization of the promise of the alloying anodes. There has been a great deal of interest in understanding the alloying

mechanisms, stoichiometry of the reaction, structural changes, and mechanical stresses, which is essential in facilitating precise control over the mechanical and electrochemical behavior of these electrodes and harvesting their superior specific energy capacity for reliable, long-lasting Li ion batteries.

1.1.1. Silicon anodes

Silicon is one of the group IV elements that has been extensively researched as a potential anode material for LIBs because of its high lithium insertion capacity at ambient temperature (3579 mAh/g), which is approximately 10 times that of graphite¹⁰, its low discharge potential, and its abundance in the earth's crust. Different Si electrode configurations including composites, thin films, and micro/nanostructures have been devised and evaluated previously. Composite electrodes consist of an electrochemically inactive structural matrix that contains active electrode particles¹¹⁻¹³. This type of electrode sacrifices the amount of active materials in exchange for mechanical stability¹⁴. The matrix accommodates the large volume expansions while providing electrical conductivity. Thin film Si electrodes¹⁵⁻¹⁸ have higher specific energy capacity compared to composite electrodes due to the absence of the binder. However, their performance declines for thicknesses beyond hundreds of nanometers¹⁹ and this limits the total amount of active material of the electrode. Recently, micro/nanostructured anodes have attracted great deal of attention due to their ability to withstand mechanical degradation. Microporous Si particles^{20,21} and Si microposts²² were studied for their capacity retention behavior during de/lithiation cycles. Several nanoscale Si

configurations²³ including nanowires^{24, 25}, nanotubes²⁶, nanoparticles^{11, 12}, core-shell nanotubes^{27, 28}, and yolk-shell nanoparticles²⁹⁻³¹ have been designed and tested for their lifecycle and Li-insertion-induced-strain mitigation mechanisms.

The existing literature on the metallic anodes suggests that:

- i. Research on high capacity electrode materials has directed us to alloying anodes as promising replacements for carbonaceous materials. Among various metallic materials, Si, Sn, and Ge anodes have been vastly studied due to their superior volumetric and gravimetric capacities^{5, 7, 32-34}.
- ii. Different configurations have been explored. Thin films of amorphous Si^{16, 35, 36} and Ge³⁷ anodes show a single-phase reaction, while the Li-Sn^{33, 38} system goes through multiple phases during de/lithiation. On the other hand, crystalline Si^{39, 40} and Ge^{41, 42} structures demonstrate irreversible solid solution phase transformation.
- iii. The high energy density of these anodes results in large volumetric changes (~300%) during cycling which leads to mechanical degradation and fast capacity fade^{7, 39, 43-45}. The failure mechanisms of thin films^{43, 46-48}, composites^{42,43,49}, and micro/nanostructures^{24, 50} have been investigated by several groups.
- iv. Establishing a predictive model that provides a detailed description for the interaction of the electrochemical and mechanical parameters^{15, 51-53} during phase transformation is critical in choice of material and processes to optimize the performance of LIB's.

Being the most abundant and environmentally benign element while possessing the highest gravimetric capacity, Si has been in the forefront of research among these materials. It demonstrates an example of a two-phase system during its first cycle lithiation with crystallographic-orientation-dependent electrochemical and kinetic characteristics. As such, we

have chosen Si as the model material for investigation of the phase transformation in electrode materials. Knowledge of the effects of size, shape, and crystallographic-orientation characteristics of this model material helps in understanding the electrochemical response and its coupling with the volume expansion and stress development that might compromise the efficiency and integrity of these phase transforming electrodes. To be able to predict the behavior of the Li-Si system, this thesis engages in an investigation of the kinetics and thermodynamics of the alloying process through well-defined experiments, combined with computational analysis.

1.1.2. Experimental and computational analysis of the lithiation in silicon anodes

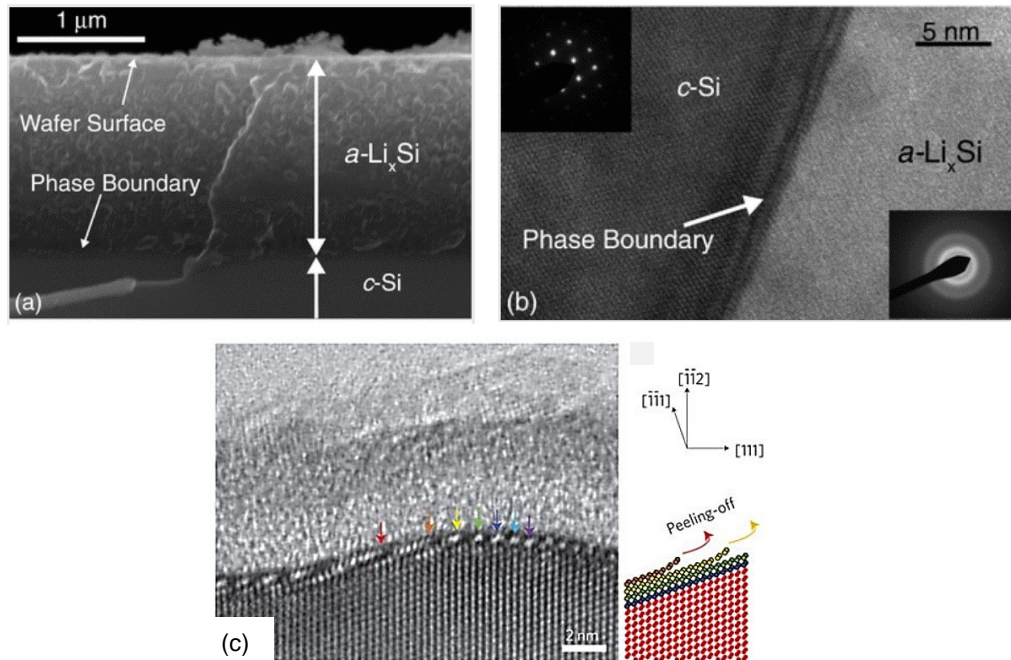


Figure 1.1. Images of the phase boundary between c-Si and a-Li_xSi using a) ex situ SEM and b) ex situ TEM on partially lithiated Si wafers (Reproduced with permission.[³⁹] Copyright 2011, American Physical Society). c) HRTEM image of the phase boundary inside a partially lithiated Si nanowire showing the ledge mechanism for the phase boundary propagation. Reproduced with permission. [⁵⁴] Copyright 2012, Macmillan Publishers Ltd.

Initial lithiation of crystalline silicon results in a phase transformation to a metastable amorphous Li_xSi phase^{55, 56} (x can be as large as 3.75 at ambient temperature), and the material remains amorphous during subsequent delithiation-relithiation cycles. A large volume change, as high as ~300%, is associated with the initial crystalline to amorphous phase transformation¹. Amorphization happens at an atomically sharp phase boundary (Fig. 1.1) where there is a very high concentration of Li in the host Si material. Thus, there is a huge discontinuity in the composition, stress, and plastic strain across the propagating phase boundary between the crystalline Si and amorphous Li_xSi . The resulting stresses in the Li_xSi layer can lead to cracking and pulverization (Fig. 1.2), which in turn contributes to the decline in the coulombic efficiency during subsequent cycling⁵. Acoustic emission measurements during constant current-constant voltage experiments on composite Si electrodes showed that the majority of mechanical failure of the Si particles happen due to stresses forming during the first cycle of lithiation⁵⁷. There have been several investigations^{39, 53, 54, 58-67} on the diffusion induced phase transformation in silicon. Nuclear magnetic resonance (NMR) was applied to study the interactions between Li and Si, the local environment of the atoms, and the Li content of the resulting silicide during first cycle lithiation^{68, 69}. Lee et al.^{60, 61} studied the phase propagation in Si nanopillars with different axial orientations. The electrodes were lithiated potentiostatically. Ex situ scanning electron microscopy (SEM) imaging of the nanopillars revealed that the volume expansion normal to (110)-oriented faces was dominant as shown in figure 1.3. Similar results were concluded from ex situ SEM imaging on lithiated arrays of Si bars etched on the surface of Si wafers²². Another set of experiments used in situ transmission electron microscopy (TEM) for presenting more detailed visualizations of the characteristics of the phase boundary, anisotropic lithiation, and orientation

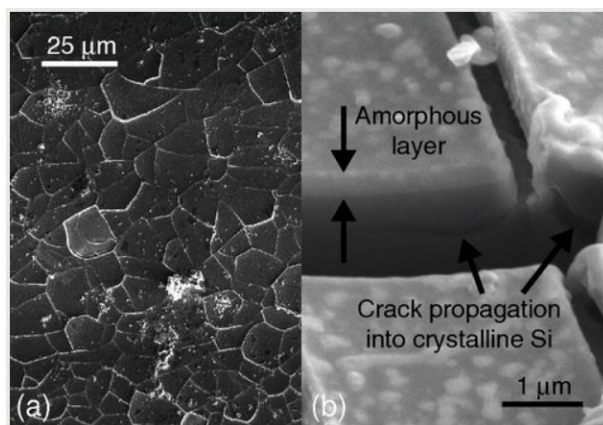


Figure 1.2. crack propagation during delithiation of Si wafers. a) SEM image of the surface of the wafer after delithiation, b) FIB cross section showing the cracks propagate into the crystalline Si layer. Image Reproduced with permission. [39] Copyright 2011, American Physical Society.

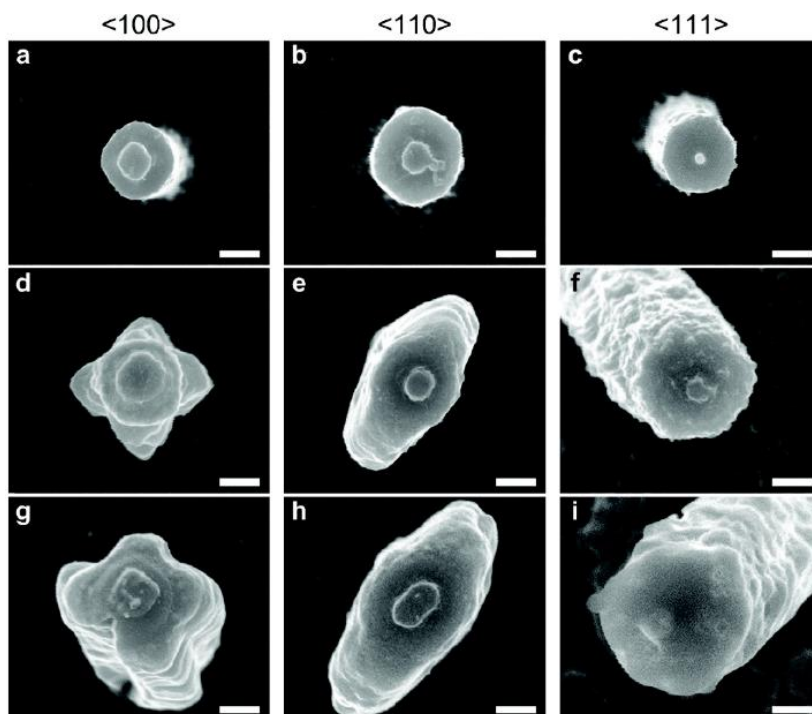


Figure 1.3. SEM images of Si nanopillars with different axial orientations: $\langle 100 \rangle$, $\langle 110 \rangle$, and $\langle 111 \rangle$ on the first, second, and third columns, respectively. (a-c) show the pristine state of the nanopillars. (d-f) and (g-i) show the partially and fully lithiated morphology of the nanopillars. Scale bar is 200nm. Reproduced with permission. [60] Copyright 2011, American Chemical Society.

related volume expansion. Diffusion induced phase transformation in Si nanowires^{54, 70} and nanoparticles⁷¹ have been studied widely in these regards. Chon et al.³⁹ combined ex situ TEM and SEM techniques to study the phase propagation in single crystalline Si wafers (Fig. 1.1a and 1.1b). They measured the biaxial stresses in the amorphous Li_xSi layer during the first cycle de/lithiation using a multibeam optical stress sensor (MOSS) curvature measurement technique.

Computational analysis of the amorphization of Si during lithiation has also received its fair share of attention. Finite element analysis based on theoretical models of a moving phase boundary propagation can be found in the works by Pharr et al.⁵⁹, Zhao et al.⁵³, Di Leo et al.⁷², and Cui et al.⁷³ among others^{6, 12}. Ab-initio molecular dynamics and First-principle density functional theory simulations have also been used to study the structural evolution in crystalline and amorphous Si during Li insertion⁷⁴⁻⁸². The key conclusion from the existing literature can be summarized as

- 1) Phase transformation happens through propagation of sharp phase boundaries; the thickness of the phase boundary is of the order of $\sim 1 \text{ nm}$ ^{39, 54, 83} as shown in figure 1.1b.
- 2) The amorphous phase behind the phase boundary is usually under a compressive stress of the order of 1 GPa^{39, 63, 84, 85}.
- 3) Kinetics of the phase boundary propagation normal to different crystallographic planes ($\{100\}$, $\{110\}$, and $\{111\}$) and the associated volume expansion can vary substantially^{59, 64, 70}; phase boundary propagation is thermodynamically more favorable normal to $\{110\}$, followed by $\{111\}$ and $\{100\}$ (See also Fig. 1.3).
- 4) The mechanism of Li insertion into silicon is proposed to be through diffusion of Li preferentially between $\{111\}$ planes⁵⁴ (Refer to Fig. 1.1c).

Many of these observations (1-3) were arrived at through a variety of indirect measurements, post-experimental observations of changing shape of micro/nano pillar specimens, coupled with computational simulation/modeling^{39, 53, 58-63}.

Experimental measurements on the lithiation of Si nanostructures has shown that as lithiation proceeds, the increase in the hydrostatic pressure decelerates the progression of the phase boundary^{86, 87}. Capturing all the aspects of the phase transformation behavior in the Li-Si solid solution is not possible unless the underlying kinetics, thermodynamics, and mechanics are rigorously researched. Computational simulations based on analytical models inspired by the experimental observations provide the tool for such examinations. It was shown that the electrochemistry of lithiation, concentration gradients, and inhomogeneous volume changes affect the stresses induced inside Si due to the diffusion of Li^{88, 89}. Linear elastic models^{89, 90} have been developed to explain these size and diffusion-rate dependent stresses during lithiation of amorphous Si. These models assumed a Fickian type of diffusion. Ryu et al.⁹¹ considered the effect of large strains on the fracture of Si nanowires and Gao and Zhou⁹² studied the interplay between the stresses and Li diffusion in Si nanowires using a finite deformation model. The large volumetric strain and fracture observed during the lithiation of Si demands the development of more versatile models that would incorporate the plastic flow and irreversible deformations caused by the insertion of large concentrations of Li and breaking of the Si-Si bonds. Bower et al.⁹³ developed a model for a full cell that took into account the Li transport between the cathode and anode plus the interactions with the electrolyte. Their model included the effect of flow stresses and finite strains and its predictions matched well with the stress-potential coupling observed experimentally during lithiation of Si thin films. Cui et al.⁹⁴ introduced a modified chemical potential that included the effect of stresses and applied their model to a spherical amorphous Si particle to study the stresses

during dis/charge cycles. In a later work, Cui et al.⁷³ accounted for the phase transformation in a binary solid solution. They solved a moving phase boundary problem by including the effect of the interface reaction in addition to the bulk diffusion. Anand⁹⁵ developed a Cahn-Hilliard type phase-field model for describing the large elastic-plastic deformations during phase transformation induced by diffusion. These two-phase lithiation models indicated the significance of the effect of the diffusion induced stresses on the phase transformation characteristics of solid solutions, the resulting volume expansion, and the concentration and strain discontinuity at the phase boundary. The dissipation due to plasticity^{63, 96} and the effect of stress concentration on the fracture of electrode materials^{53, 97} are other critical factors to be considered in the lifecycle analysis of a battery.

1.2. Overview of the thesis

The objective of this thesis is to characterize the kinetics of the phase transformation in silicon anodes during the first cycle lithiation in lithium ion batteries and investigate its correlation to the underlying thermodynamics and mechanics through experimental and computational approaches.

The crystallographic orientation dependent kinetics of the amorphization of crystalline silicon is investigated through a novel optical pump-and-probe technique. We introduced the “picosecond ultrasonics” technique as a non-destructive in situ method for real time monitoring of the position of the moving reaction front inside a working battery electrode.

The second chapter is dedicated to the introduction of the picosecond ultrasonics (PU) method and the theoretical background behind its operation. PU is a non-invasive pump-and-probe technique used for thin film metrology. It operates through generation and detection of acoustic waves. In

this chapter, the basic physics of the generation and detection of the acoustic waves, the organization of the optical setup, and the specifics of the function of the apparatus utilized in the setup are described meticulously. Explanation of the signal analysis and an overview on the alignment and optimization process are provided subsequently.

The third chapter deals with the integration of the PU technique with an electrochemical system. This combination allows precise measurement of the kinetics of the phase boundary propagation under diverse driving forces during galvanostatic and potentiostatic lithiation of Si anodes. The velocity of the phase boundary propagation through different crystallographic orientations is reported; the advantages of this technique over the ones previously adopted in the literature and comparisons between the results are provided. A steady-state Deal-grove type model is used to analyze the kinetic parameters of the Li diffusion based on the experimental data. Additionally, an in situ atomic force microscopy (AFM) method is introduced to establish the relation between the volume expansion and the state of charge during lithiation.

In Chapter 4, a moving phase boundary model is calibrated based on the experimental data from the third chapter. To conduct the computational analysis, a modified Cahn-Hilliard type phase-field model is developed that includes the effects of finite deformations, plasticity, and flow stress. A concentration-gradient dependent mobility is introduced to impose finite mobility to the interface. Comparing the results of the simulation with the experiments, the exchange current density of the reactions at the surface, mobility of Li in the Li_xSi layer, interface mobility parameter, and the free energy potential for the Li-Si system are determined.

The last chapter provides a summary of the results and conclusions of this work and discusses some of the possible future works.

2. Picosecond ultrasonics technique

2.1. Introduction

Picosecond ultrasonics (PU) is a pump and probe technique that measures the internal features of the material under study using ultrasounds that are generated and detected optically. A pump pulse is absorbed in a metal thin film and the resulting thermal dilatation creates a sound pulse, the width of which is proportional to the thickness of the metal film. This longitudinal wave travels inside the material with a velocity of few nanometers per picosecond and gets partially reflected when it reaches an interface. When the reflected part of the pulse (echo) returns to the surface, it changes the reflectivity of the metal film, which is constantly measured by the probe beam. The PU technique offers a non-destructive method for identifying the material properties of samples with different geometries. It has been used for measuring the velocity and attenuation of phonons in transparent materials⁹⁸, bonding imperfections in silicon-on-insulator wafers and properties of metal layers in silicon chips⁹⁹, semiconductor heterostructures and nano-cavities¹⁰⁰, and biological cells^{101, 102}. The PU technique also enables precise measurement of the elastic properties of thin films^{103, 104}. The method makes the non-destructive measurements in both solids and liquids¹⁰⁵ possible under conditions where conventional approaches are not applicable. In this chapter, we explain the fundamental physics behind the generation of the acoustic waves due to absorption of the pump pulses in a PU transducer. We follow the path of the pump and probe

beams from the laser to the sample and give detailed explanation of the role of each apparatus on the beams' path in modification and transportation of the beams. The importance of the transducer in the quality of the signal is investigated. Then, a modified version of the Maxwell's equation for the propagation of electromagnetic waves is solved to identify the influence of the strain wave in the reflection/transmission properties of the transducer and hence, the possibility of detection of the changes in the reflectivity of a film by the probe beam is explained. The last section is devoted to the procedures for the alignment of the pump and probe laser beams and optimization of the signal.

2.2. Picosecond ultrasonics – Optical generation

Picosecond ultrasonics is a non-invasive technique that measures the thickness of thin films using ultrasound pulses generated and detected by ultra-fast laser pulses¹⁰⁶. A schematic diagram of the technique is shown in figure 2.1. The Al thin film deposited on top of the Si wafer serves as the transducer. When a pump light pulse (pulse duration of ~ 100 fs) is absorbed by the Al film, the temperature of the film rises, causing a build-up of thermal strain which launches a strain pulse into the Si wafer¹⁰⁶. The energy absorbed in the Al film per pulse and per unit volume at a depth z is

$$W(z) = (1 - R) \frac{Q}{A \xi} e^{-z/\xi} \quad (2.1)$$

where R is the optical reflectivity of the surface, Q the energy per pulse, ξ the absorption depth, and A the area illuminated by the laser light. The energy of the light pulse is given to the electrons in the Al film. These free electrons diffuse very rapidly through the Al film (within a time less than 1 ps) and as a result the temperature rise of the film quickly becomes nearly independent of the distance z from the surface. The temperature change is then

$$\Delta T(z) = \frac{Q(1-R)}{w A \rho_{Al} C_{Al}} \quad (2.2)$$

where ρ_{Al} is the mass density of Al, w is its thickness, and C_{Al} is the specific heat per unit mass. This produces a thermal strain in the z direction within the aluminum film given by

$$\varepsilon_{zz}^T(z) = \frac{\beta Q(1-R)}{w A \rho_{Al} C_{Al}} \equiv \varepsilon_0 \quad (2.3)$$

where β is the linear expansion coefficient of the material. This strain launches two propagating sound pulses, one towards the free surface and the other into the silicon substrate. At the free surface, the zero traction boundary condition results in complete reflection with a sign change. At the Al to Si interface there is almost complete transmission because there is a close match between the acoustic impedance of these two materials. The densities and sound velocities are $\rho_{Al}=2.7$ g/cm³ and $\rho_{Si}=2.33$ g/cm³, and the sound velocities are $v_{Al}=6.3$ nm/ps and $v_{Si}=8.4$ nm/ps (<100> direction). As a result, at time t after the application of the pump light pulse the strain in the silicon is given by

$$\varepsilon_{zz}^T(z, t) = \begin{cases} 0, & vt - w > z \\ -\varepsilon_0/2, & vt > z > vt - w \\ +\varepsilon_0/2, & vt + w > z > vt \\ 0, & z > vt + w \end{cases} \quad (2.4)$$

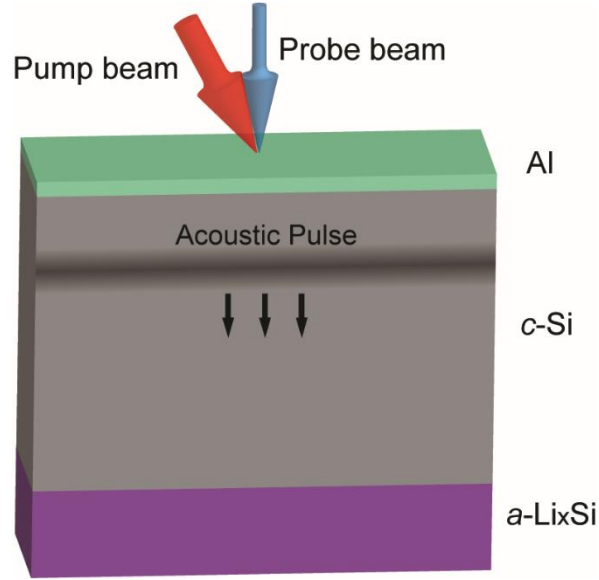


Figure 2.1. Schematic of the picosecond ultrasonics measurement technique. The pump and probe light pulses are focused onto the same spot on the Al surface. The application of the pump light pulse results in the generation of an acoustic pulse. The change in the reflectivity due to the returning acoustic echo is detected with a time-delayed probe light pulse.

Some conditions must be satisfied in order for equation (2.4) to be a reasonable approximation. First, we note that allowance for the partial reflection of sound at the Al to Si interface will give a somewhat more complicated shape for the sound pulse than is given by equation (2.4). The change in temperature generates two strain pulses, one moving in the positive z direction and the other in the negative direction. The sum of the contributions from these two pulses determines the spatial shape of the generated pulse. Thomsen et al.¹⁰⁶ showed that these contributions are mainly governed by the ratio of the heat diffusivity to the product of sound velocity and the absorption

depth of the transducer. Second, we have taken the sound propagation to be in one dimension. This will be a good approximation provided that the distance the sound travels is less than $L \equiv d^2/\lambda$, where d is the diameter of the region onto which the pump is incident, and λ is the sound wavelength. If we consider the sound to be a single cycle of a wave, then $\lambda = 2w$ and so $L \equiv d^2/2w$. Since $d \sim 10 \mu\text{m}$ and $w = 25 \text{ nm}$, we have $L = 4 \text{ mm}$, i.e., substantially greater than the thickness of the silicon wafer. It is also assumed that the increase in the temperature occurs instantaneously, i.e., the duration of the light pulse is very small relative to the temporal length of the strain pulse. The duration of the laser pulses is about 100 fs whereas the time for the sound to make one trip through the Al film is 4 ps. From Eq. 2.2, the change in the temperature of the Al layer is about 10 K.

The total stress can be calculated as

$$\sigma_{zz}(z, t) = 3 \frac{1-\vartheta}{1+\vartheta} B \varepsilon_{zz}(z, t) - 3B\beta(1-R) \frac{Q}{A\xi\rho C} e^{-z/\xi} \quad (2.5)$$

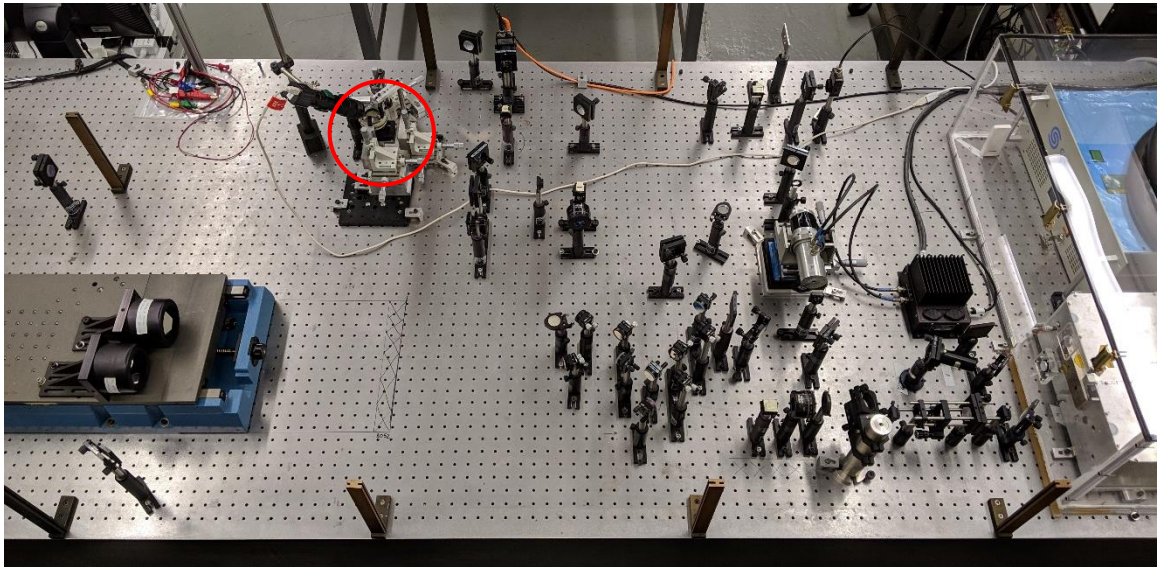
where, ϑ is the Poisson's ratio and $\varepsilon_{zz}(z, t) = u_{z,z}$. The equation of the motion in the z direction has the form $\rho \frac{\partial^2 u_z}{\partial t^2} = \sigma_{zz,z}$. Combining equation 2.5 with the equation of motion and using zero stress boundary condition at the free surface and zero strain initial condition give the profile of the resulting strain field as a function of the depth and time¹⁰⁶:

$$\varepsilon_{zz}(z, t) = (1-R) \frac{Q\beta}{A\xi\rho C} \frac{1+\vartheta}{1-\vartheta} \left[e^{-z/\xi} \left(1 - \frac{1}{2} e^{-vt/\xi} \right) - \frac{1}{2} e^{-|z-vt|/\xi} \text{sgn}(z-vt) \right] \quad (2.6)$$

This strain pulse is partially reflected and partially transmitted at surfaces/interfaces where there is a mismatch in the acoustic impedance. The optical “constants” of the materials change due to

the strain. As a result, when a reflected strain pulse returns to the Al film, the optical constants of the Al film change, which leads to a change in the optical reflectivity of the film.

(a)



(b)

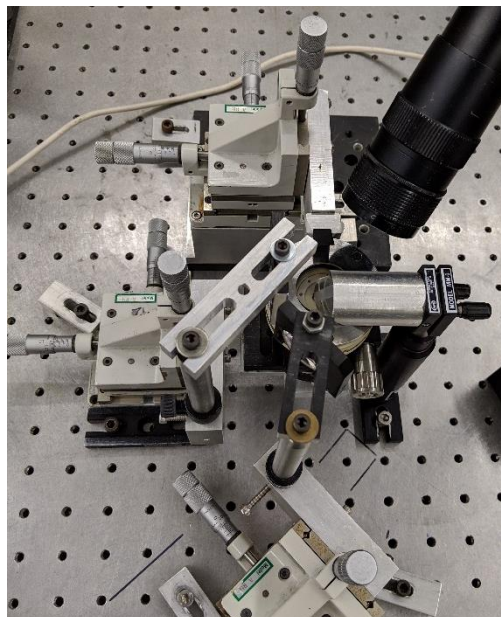


Figure 2.2. (a) Picosecond ultrasonic setup; the position of the sample on the setup is marked with a red circle, (b) a closer look at the sample position.

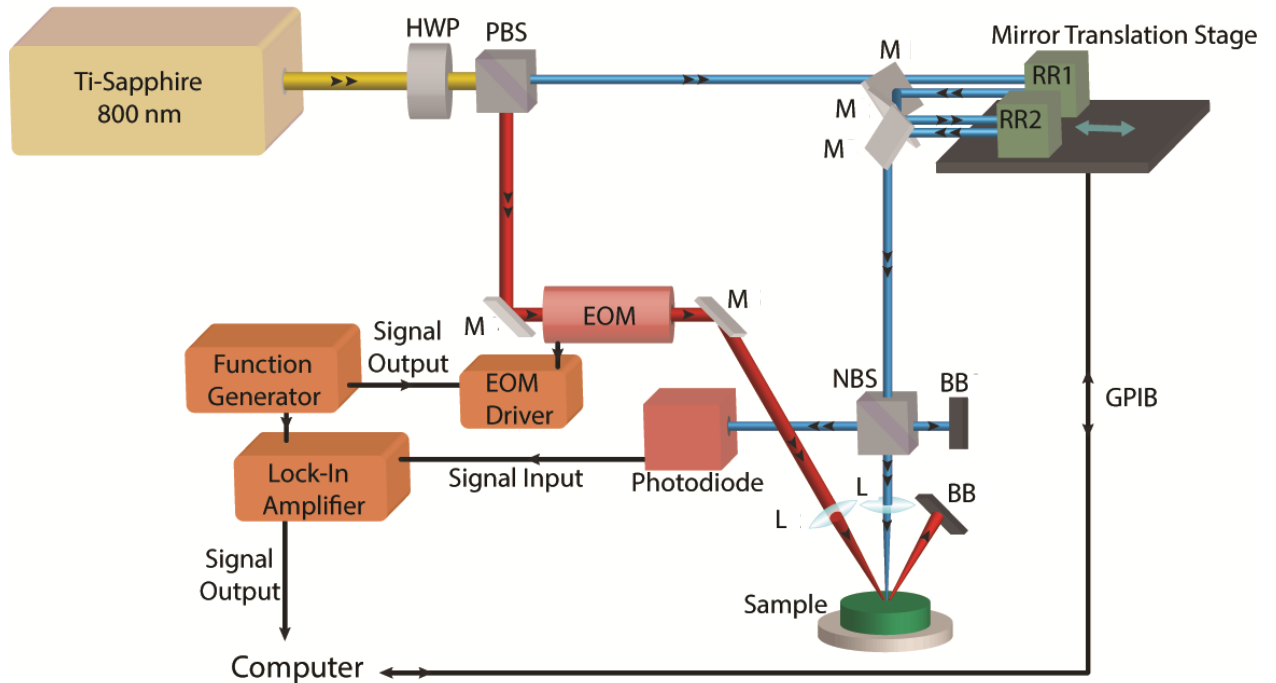


Figure 2.3. A schematic diagram of the basic setup for picosecond ultrasonics; the initial laser, pump, and probe laser pulses are shown in yellow, red, and blue, respectively. HWP – Half-wave plate, PBS – Polarized beam splitter, M – Mirror, EOM – Electro-optic modulator, L – Lens, BB – Beam blocker, RR – Retroreflector, NBS – Non-polarized beam splitter

This change in reflectivity is detected by a time-delayed probe light pulse. The arrival time of these reflected echoes can be measured by repeating the experiment over a range of delay times for the probe light pulse. An image of the optical setup and a closer look at the sample position are given in figure 2.2. A schematic diagram of the optics comprising the picosecond ultrasonics setup is shown in figure 2.3. The laser source is a mode-locked Ti-Sapphire pulsed laser with the operating wavelength tuned to 800 nm. The pulse duration is about 100 fs. The repetition rate is 80 MHz, so

a laser pulse is generated once every 12.5 ns. The laser output is split into two beams, the pump beam and the probe beam, via a half-waveplate (HWP), immediately followed by a polarized beamsplitter (PBS). After the PBS, the pump beam passes through an electro-optic modulator (EOM). The EOM modulates the intensity of the pump beam at 1 MHz, so that lock-in detection can be used to improve the signal-to-noise ratio. Modulating the pump beam results in a modulation of the change in reflectivity due to the strain generated by the pump beam. The lock-in amplifier will then amplify the 1 MHz component in the signal from the intensity of the probe beam reflected from the sample. To vary the delay time of the probe beam with respect to the generating pump beam, the probe beam is directed to a pair of retroreflectors (RR) mounted on a translation stage. The delay stage modifies the path length of the probe beam so that scanning of the surface of the Al film over diverse time ranges is facilitated. The relative arrival time of the probe pulse is controlled by translating the RR's parallel to the probe beam path. It is important to carefully optimize the probe beam path to enter and exit each retroreflector at a normal angle to avoid lateral displacement of the beam especially during longer scans. Lateral displacement of the beam will move the position of the focused probe beam on the surface of the sample and leads to the appearance of an additional background component – called the “beam walk” – to the recorded signal.

Both the pump beam and the probe beam are then focused onto the surface of the sample, with the probe beam at normal incidence and the pump beam at a selected angle of incidence. The beams are arranged at different angles and polarizations so that the signal from the scattered pump beam can be reduced. A non-polarized beamsplitter (NBS) is installed before the lens of the probe beam, so that the probe beam reflected from the sample can be directed to a photodiode. The signal from the photodiode is then fed into the lock-in amplifier, locking-in at 1 MHz. The lock-in amplifier is

synchronized to the EOM via a reference signal from the same function generator that drives the EOM. Finally, the output from the lock-in amplifier goes to a data acquisition (DAQ) card installed in a computer. The computer also controls the translation stage via a GPIB interface. By synchronizing the position of the translation stage and the data collected from the lock-in amplifier, the computer records the change in reflectivity as a function of the probe delay time.

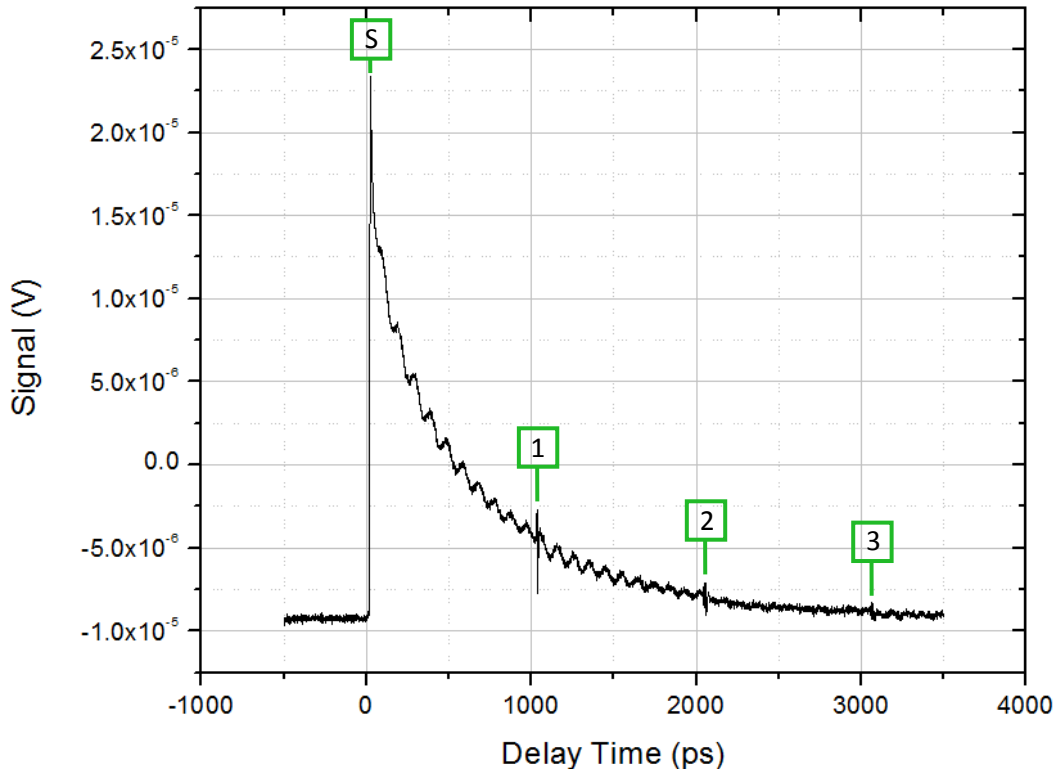


Figure 2.4. Picosecond ultrasonic measurement on a thin silicon sample. The numbers in the boxes indicate the number of round trips of the echo inside the Si sample up to that time. Each round trip takes 1011 ps. “S” shows the simultaneous arrival of the pump and probe pulses at the surface of the sample and generation of the sound wave. The oscillations arise from the small amplitude sound pulse that propagates from the Al film into the epoxy.

In order to demonstrate the measurement, we have done a PU measurement on a thin crystalline Si wafer attached to a fused silica substrate using transparent epoxy. An Al film with 25 nm

thickness is deposited on top of Si, which serves as the transducer. The result is shown in figure 2.4. The jump at zero probe delay time (marked with “S” in Fig. 2.4) corresponds to the simultaneous arrival of the pump and probe pulses at the surface of the sample and generation of the sound wave. Absorption of the pump light pulse in the Al film causes a sudden thermal expansion of the film. Following the initial jump, the signal has two components, a slowly decreasing background component and oscillations with small amplitude. The background component comes from the change in the temperature of the Al film. It decreases with time as heat diffuses into the crystalline Si. The smaller amplitude oscillations are called “Brillouin Oscillations” (BO)⁹⁸, and arise from the small amplitude sound pulse that propagates from the Al film into the epoxy. Such oscillations appear whenever the probe light interrogates the transducer film through a transparent medium (here, the transparent epoxy) that is well-bonded to the transducer film. The sound pulse in the transparent epoxy causes a local and moving change in the refractive index. This acts as a weakly-reflecting moving mirror. The probe light reflected from this moving mirror interferes with the probe light reflected from the interface between the epoxy and the Al, resulting in constructive/destructive interferences, giving rise to the oscillations. It is straightforward to show that the period of the oscillations is

$$T = \lambda(2v_E\sqrt{n^2 - \sin^2\theta})^{-1} \quad (2.7)$$

where θ is the angle of incidence of the probe beam, λ the wavelength of the laser beam, n the refractive index of the epoxy, and v_E the sound velocity in the epoxy. In our experiment, the laser wavelength is 800 nm and the probe beam hits the surface at a normal angle of incidence. The index of refraction of the transparent epoxy¹⁰⁷ is 1.5, and the measured period of the BO is 96 ps.

It follows from equation 2.7 that the sound velocity in the epoxy should be 2.8 nm/ps. The amplitude of the BO decreases as the sound pulse is attenuated inside the transparent epoxy.

Another feature of the recorded signal is the equally spaced pulses, marked with green boxes in figure 2.4. They are indicative of the travel time of the echo during round trips inside the Si sample.

The numbers in the boxes show the number of round trips up to that point. Arrival of the echo to the surface after each round trip produces a new set of BO's that are superimposed on top of the existing BO's. In the demonstration experiment shown in Fig. 2.4, the round trip travel time is 1011 ps.

The longitudinal sound wave velocity in the <100> direction of c-Si is known to be 8.4 nm/ps. Therefore, we can measure the thickness of the Si wafer to be 4.25 μm . The precision of these measurements is about ten nanometers. The decrease in the amplitude of the pulses is due to attenuation of the stress pulse and also transmission of part of the pulse into the film at the interface.

The ratio of the reflected to transmitted pulses at the interface is controlled by the acoustic impedance mismatch (Z) at the interface. If the bonding at the interface is perfect, the reflection coefficient is given by $\frac{Z_{Al}-Z_{Si}}{Z_{Al}+Z_{Si}}$, where Z_i is the acoustic impedance of material i and is defined as the product of the longitudinal wave speed and the mass density.

Figure 2.5 depicts the significance of the quality of the Al film and bonding between the film and Si wafer. Bad bonding results in slow heat diffusion and accumulation of the heat in the film. The quality of the film affects its optical constants and results in a much weaker initial jump, i.e. a reduced signal-to-noise ratio.

The signal in figure 2.5b is so weak that the BO's are not recognizable from the noise.

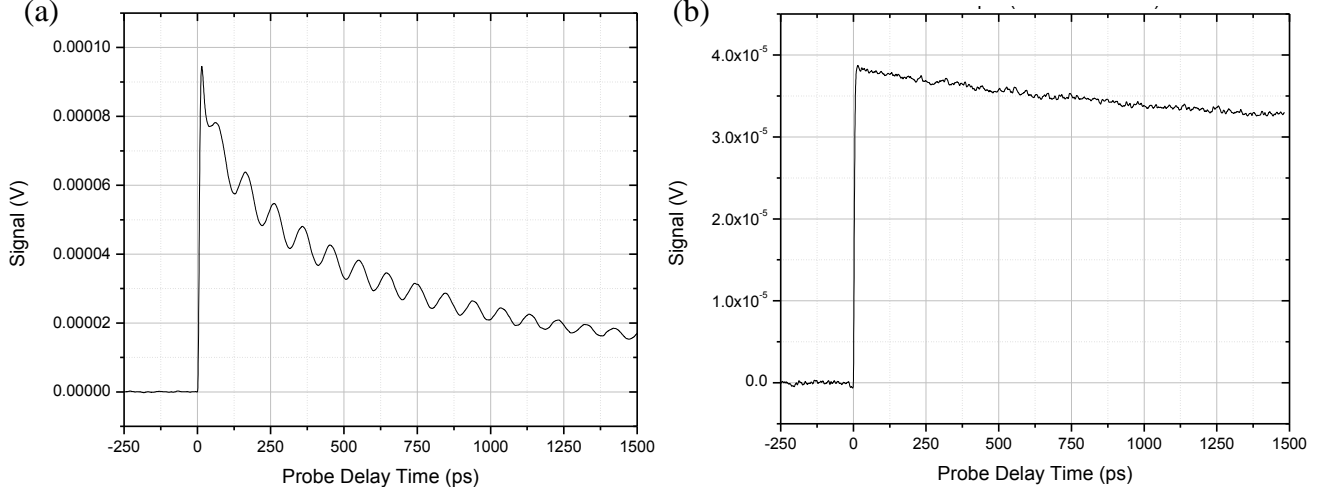


Figure 2.5. Comparison between (a) good and (b) bad quality of the Al film and bonding between the Al film and Si sample. The effects are significant in the heat diffusion properties and the signal-to-noise ratio.

2.3. Picosecond ultrasonics – Optical detection

To minimize the scanning time, we focus our measurements on the time range that we expect the strain pulse reflected from the surface of the sample to return. The reflected strain pulse modifies the optical constants of the film and, hence, results in a change (ΔR) in the reflected intensity of the probe beam. The changes in the real and imaginary parts of the index of refraction are related to strain as $\Delta n = \frac{\partial n}{\partial \varepsilon_{zz}} \Delta \varepsilon_{zz}$ and $\Delta \kappa = \frac{\partial \kappa}{\partial \varepsilon_{zz}} \Delta \varepsilon_{zz}$ respectively.

In the absence of strains, we can think of the probe beam as an electromagnetic wave with polarization in the x direction (E_x) traveling in the z direction in air

$$E_x = E_0 e^{i(k_0 z - \omega t)} \quad (2.8)$$

Upon reaching the surface of the film, the reflected and transmitted waves are identified as

$$E_x^{(r)} = r_0 E_0 e^{i(-k_0 z - \omega t)} \quad (2.9)$$

$$E_x^{(t)} = t_0 E_0 e^{i(k z - \omega t)} \quad (2.10)$$

with $k = k_0(n + i\kappa)$ and k_0 are the wave numbers in the film and air, respectively. $r_0 = \frac{k_0 - k}{k_0 + k} =$

$\frac{1-n-i\kappa}{1+n+i\kappa}$ and $t_0 = \frac{2k_0}{k_0 + k} = \frac{2}{1+n+i\kappa}$ are the reflection and transmission coefficients, respectively.

Presence of strain changes the reflection coefficient of the film (r), which in turn modifies the reflectivity (R) of the material. Maxwell's equation in the presence of strain has the form

$$\frac{\partial^2 E_x(z,t)}{\partial z^2} = \frac{1}{c} \frac{\partial^2 E_x(z,t)}{\partial t^2} = -\frac{\omega^2}{c^2} (\epsilon + \Delta\epsilon(z,t)) E_x(z,t) \quad (2.11)$$

where $\epsilon = (n + i\kappa)^2$ is the dielectric constant of the film which varies with strain according to

$$\Delta\epsilon(z,t) = 2(n + i\kappa) \left(\frac{\partial n}{\partial \epsilon_{zz}} + i \frac{\partial \kappa}{\partial \epsilon_{zz}} \right) \epsilon_{zz}(z,t) \quad (2.12)$$

For a strain pulse at a distance z' from the interface, $\Delta\epsilon = F\delta(z - z')$, equation 2.11 gives a reflection coefficient of $r_1 = \frac{ik_0^2}{2k} F$. The wave transmitted into the film is partially reflected at the

strain wave and part of it gets transmitted back to the air with a transmission coefficient $t_2 = \frac{2k}{k+k_0}$.

So, the total reflected wave has the form

$$E_x^{(r)} = (r_0 + t_0 r_1 t_2 e^{2ikz'}) E_0 e^{i(-k_0 z - \omega t)} \quad (2.13)$$

Integrating over z' for an arbitrary wave gives

$$r \equiv r_0 + \Delta r = r_0 + \frac{ik_0^2}{2k} t_0 t_2 \int_0^\infty e^{2ikz'} \Delta\epsilon(z', t) dz' \quad (2.14)$$

Finally, the change in the reflectivity is

$$\Delta R = |r|^2 - |r_0|^2 = \int_0^\infty f(z) \epsilon_{zz}(z, t) dz \quad (2.15)$$

where, $f(z)$ is called the sensitivity function and depends on the absorption depth, the index of refraction of the transducer, and the wavelength of the incident light. This function determines the changes in the reflectivity of the film due to strains at different depths inside the film. If the film is thick enough ($d \gg \xi$), one may assume that ϵ , $\frac{\partial n}{\partial \epsilon_{zz}}$, and $\frac{\partial \kappa}{\partial \epsilon_{zz}}$ are constants. Then, the sensitivity function will take the shape of an exponentially damped oscillation and goes to zero for $z \gg \xi$, i.e. the absorption depth determines the range of the sensitivity function.

2.4. Setting up the apparatus for picosecond ultrasonics

GaAs wafers are used as samples for setting up and optimizing the beam path as this material has a large refractive index and thermal diffusion with a small absorption depth. An example of the signal recorded from scanning a GaAs sample is given in figure 2.6. In this measurement, the delay

time of the probe with respect to the generating pump beam is set so that the arrival of the next pump beam is also detected. The arrival time of the two pump beams are separated by 12500 ps which is dictated by the operating frequency of the laser (80 MHz). It must be noted that the arrival time of the echo from the surface of this 500 μm thick wafer is beyond the time frame of this measurement. All of the optics used in this setup are compatible with ultrafast lasers pulses. The mirrors, lenses, and beamsplitters are specialized for wavelengths near infrared.

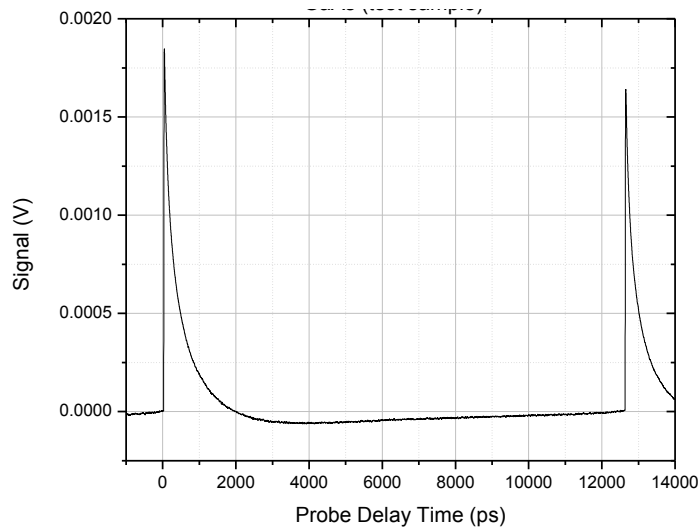


Figure 2.6. PU scan on a GaAs sample. The range of the probe delay time is chosen so that the arrival of two consecutive pump pulses at the surface are detected. Operating frequency of the laser (80 MHz) dictates the temporal distance between the two pulses. The arrival time of the echo from the surface of this 500 μm thick wafer is beyond the time frame of this measurement.

2.4.1. Adjustments on the laser beam

At a wavelength of 800 nm, the laser produces beams with an average power of 4 watts. However, a total power of 1 watt is sufficient for the purpose of our experiments. Therefore, a beamsplitter

is placed right after the laser that delivers a transmitted to reflected beam ratio of 3:1. The transmitted part is sent to a beam dump and the reflected part is directed to a collimation rack. The beam must pass parallel and centered with respect to the collimation rack (See figure 2.7). This is assured by placing two pinholes at the beginning and end of the rack. The rack holds a combination of a plano-concave lens with focal length $f_1=5$ cm and a convex lens with focal length $f_2=10$ cm. The purpose of collimation of the beam is to reduce its divergence in order to minimize its dispersion as it travels long distances. In the case of coincident focal points, these lenses deliver an expansion ratio of $\frac{y_2}{y_1} = \frac{f_2}{f_1} = 2$ and a divergence $\frac{\theta_2}{\theta_1} = \frac{f_1}{f_2} = \frac{1}{2}$. Figure 2.7b shows the schematic of the expansion of the image size from y_1 to y_2 and the divergence from θ_1 to θ_2 .

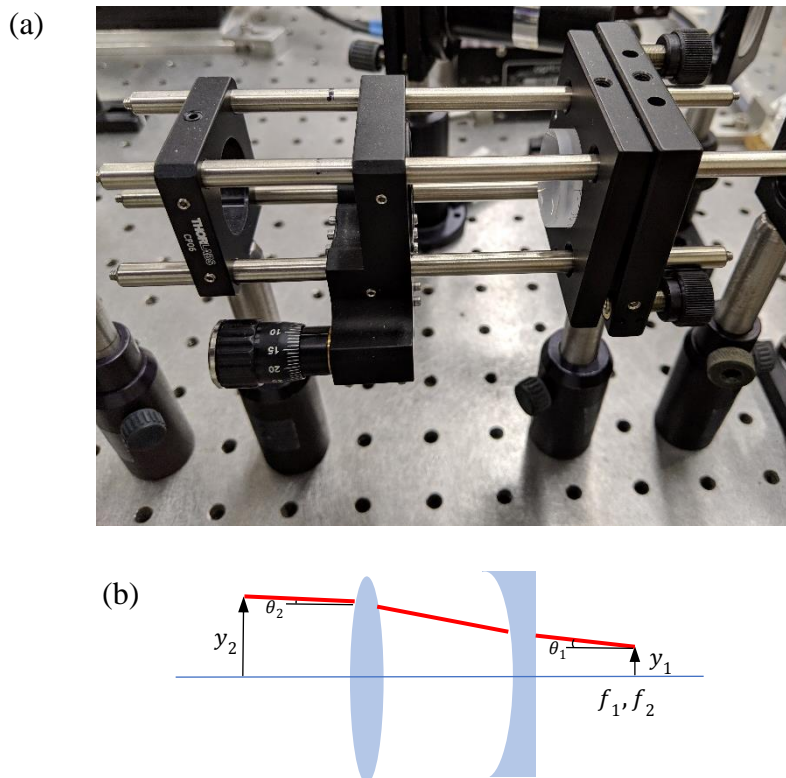


Figure 2.7. (a) Collimation rack and (b) schematic of its operation. The input beam with a width y_1 and divergence angle θ_1 is modified to give an output beam with a width y_2 and divergence angle θ_2 .

After collimation, the polarization of the laser beam is changed with a halfwave plate so that we can use a cubic polarized beamsplitter to separate the initial laser beam to a pump beam and a probe beam based on their polarizations. Figure 2.8 shows this arrangement. Changing the polarization also sets the power of the portion of the laser beam that is allocated to the pump beam.

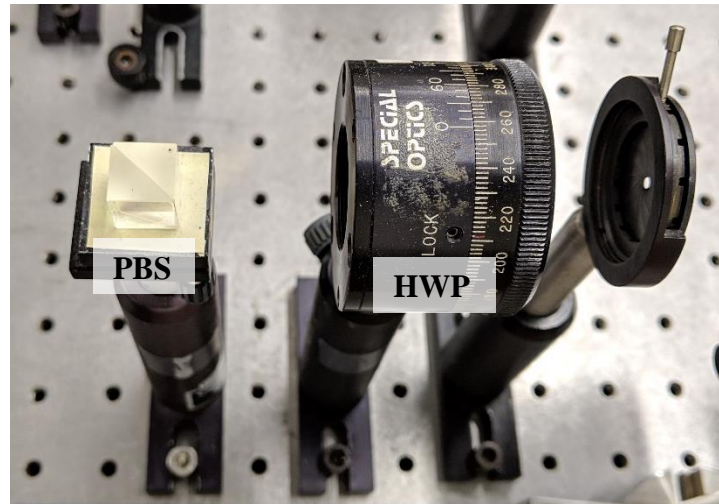
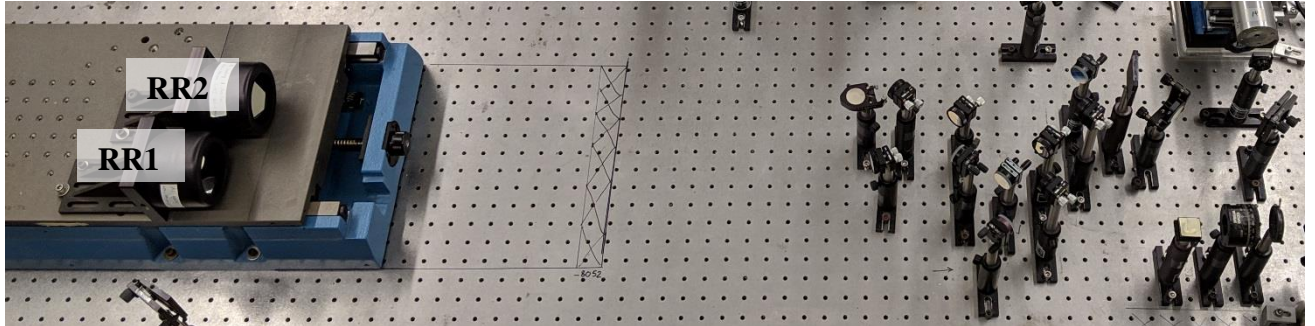


Figure 2.8. Halfwave plate (HWP) followed by a polarized beam splitter to separate the pump and the probe beam based on their polarization.

2.4.2. The probe beam

The probe beam is directed into the first retroreflector (RR1) using mirror M2 and gets reflected back to mirror M3 which leads the beam to mirror M4. This mirror sends the beam into RR1 for a second time (Refer to Fig. 2.9). Optimizing the angle of incidence of the beam from M2 to RR1 is done by setting a temporary mirror (T1) in front of M3 to send the beam to a second setup (Fig. 2.10) besides the main one.

(a)



(b)

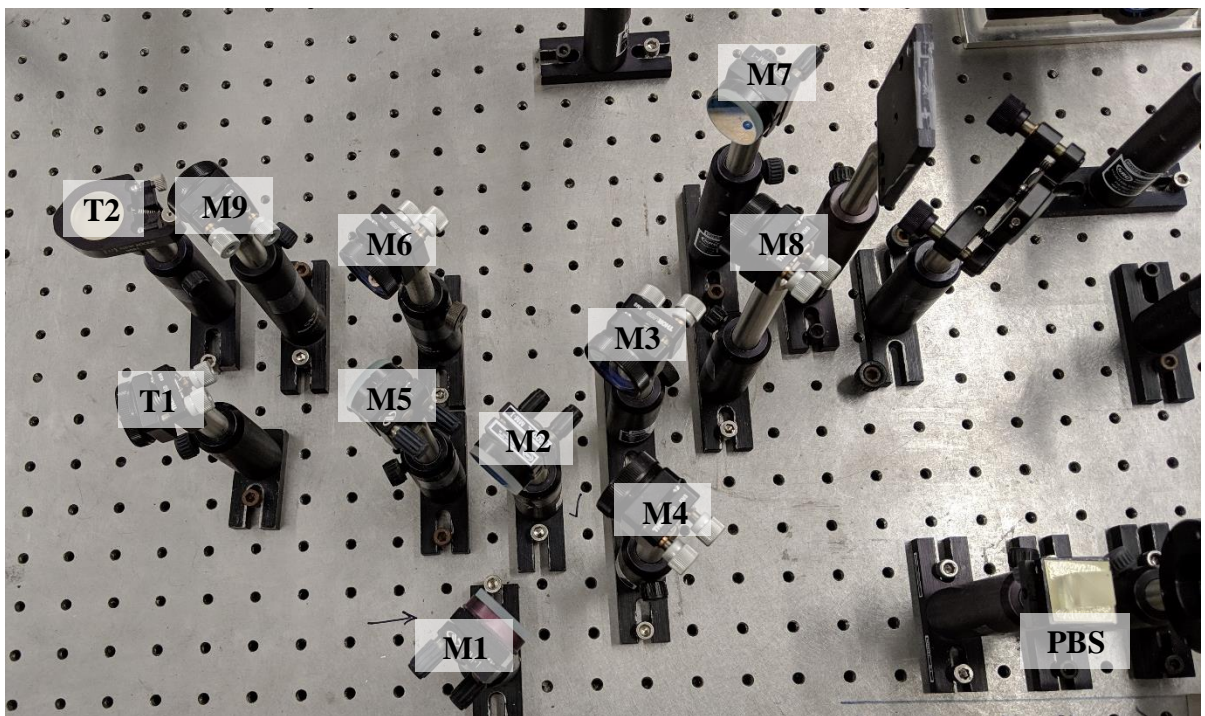


Figure 2.9. (a) Placement of the retroreflectors (RR1 and RR2), polarized beamsplitter (PBS), mirrors (M), and temporary mirrors (T1 and T2). (b) larger view of the position of the mirrors. The order in which the probe beam sees the optics is PBS, M1, M2, RR1, M3, M4, RR1, M5, M6, RR2, M7, M8, RR2, M9.

The purpose of the second setup is to minimize the lateral movement of the beam during the translation of the retroreflectors mounted on the translation stage. The Dove software[†] controls the motion of the translation stage. The second setup provides a path length of about 30 meters, passes the beam through a lens and projects the resulting image on a screen that is monitored by a CCD camera. This long beam path and its unique monitoring process magnifies the lateral motion of the beam during the translation of the RR's to make it identifiable to the naked eye. As mentioned before, beam walk will be minimized if the beam enters the RR's at a normal angle of incidence (and parallel to the translation stage). The details of this alignment procedure are explained in the appendix.

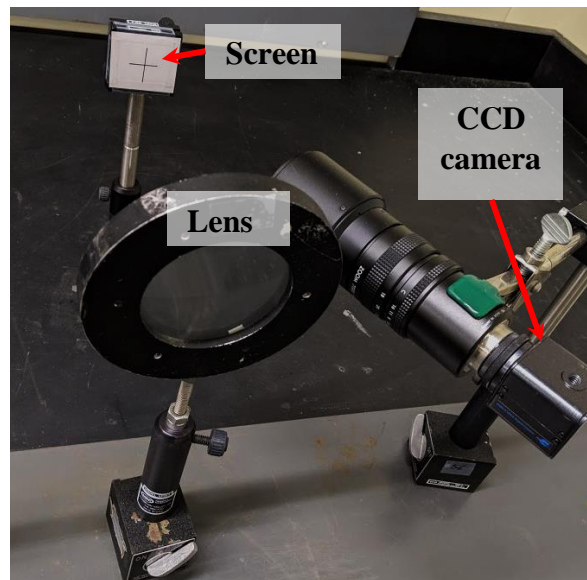


Figure 2.10. Lens, CCD camera, and the screen used in the second setup for monitoring the characteristics of the beam spot after traveling through the second setup.

[†] Developed by Li-Wei Liu, department of Physics, Brown University

Once mirrors M2 and M4 that send the beam to RR1 and the two mirrors (M6 and M8) that send the beam into RR2 are adjusted, the probe beam is sent into a halfwave plate followed by a polarized beam splitter. As explained before, this combination provides the ability of adjusting the power of the beam through modifying its polarization. The unused part of the beam is directed into a beam dump. The ratio of the power of the pump to probe must be above three to eliminate the effect of probe beam in the generation of the acoustic wave.

The remaining part of the beam passes through the lens (L1) and is focused on the sample as shown in figure 2.11b with blue arrows. To avoid beam walk, it is critical that the probe beam hit the lens (L1) and the sample at a normal angle of incidence (a detailed description of this process is given in the appendix). The beam reflected from the surface of the sample (orange arrows in Fig. 2.11b) is directed to a lens (L2) that focuses the beam at the center of the photodiode (see also Fig. 2.13a). To prevent other scattered beams from entering the photodiode, a cylindrical cover made of black paper is fixed between L2 and the photodiode.

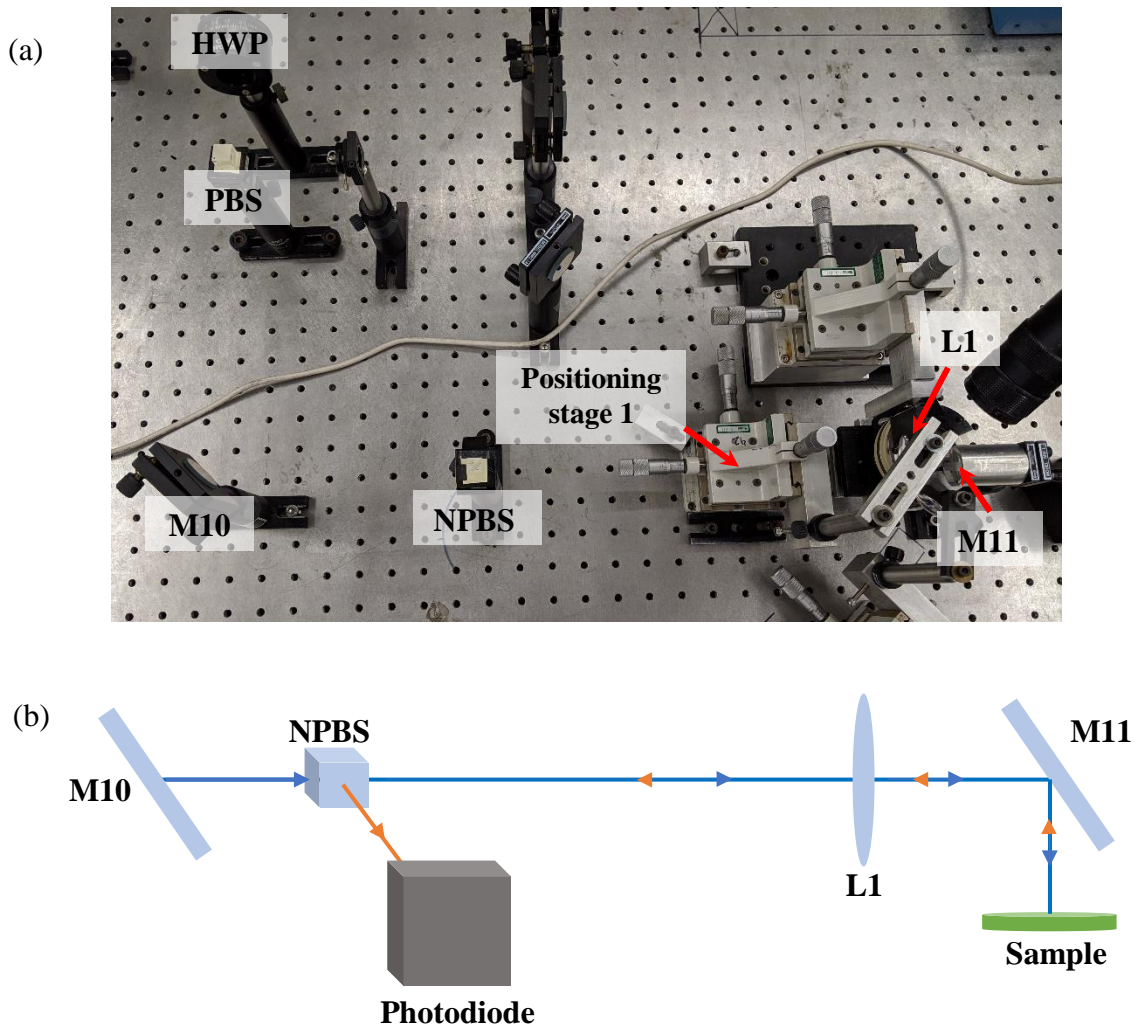


Figure 2.11. a) Apparatus and b) schematic of the last portion of the probe beam path. The beam must hit the lens (L1) and the sample at a normal angle of incidence. The ingoing beam is shown in blue and the reflected beam from the surface of the sample is shown in orange. The reflected beam is directed into a lens (not shown) followed by a photodiode.

2.4.3. The pump beam

In this section the path of the pump beam from the EOM to the sample is described. Coming out of the polarized beamsplitter, the pump beam is sent into an EOM. The beam must pass through

the EOM parallel to its cylindrical body. If it is not parallel, the beam might get scattered or cutoff inside the tool and the output intensity is significantly reduced. Figure 2.12 shows the EOM mounted on a tilt platform to provide adjustment for the pitch and yaw.

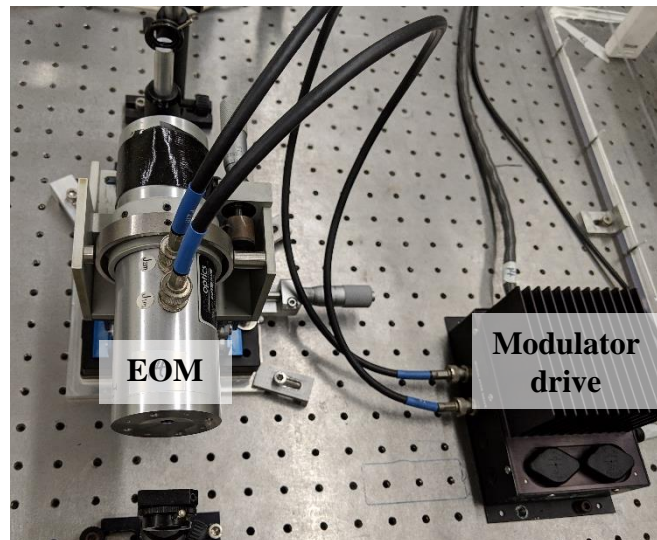
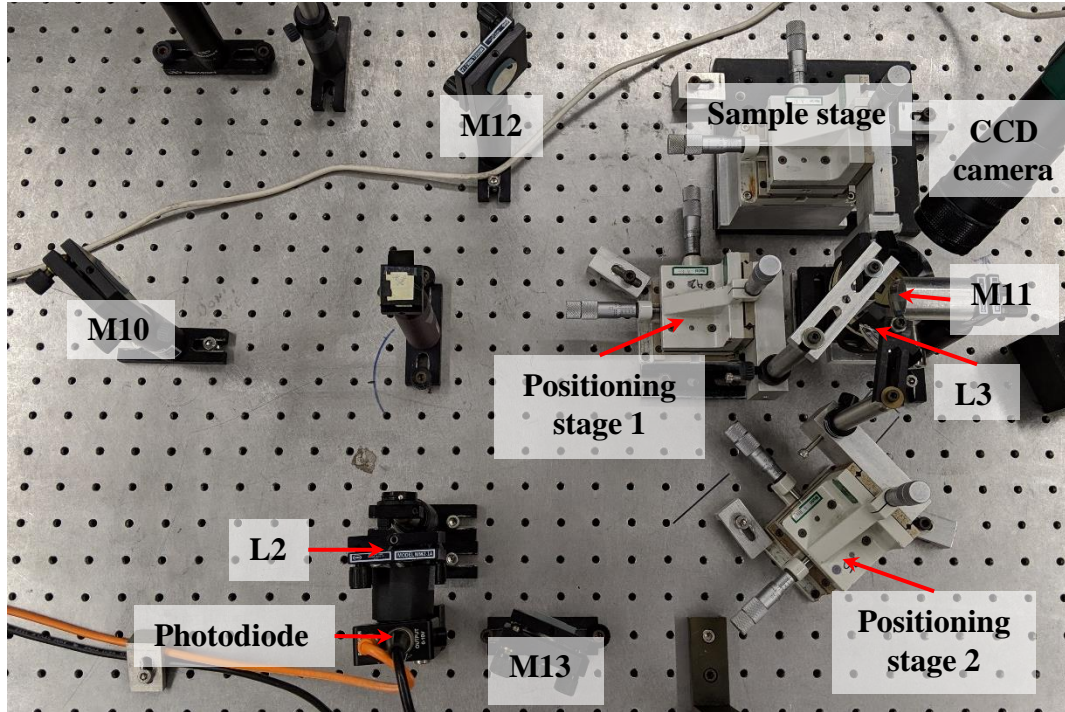


Figure 2.12. Electro optic modulator (EOM) fixed on the optical table using a pitch and yaw platform. The output of the EOM must be optimized to produce modulated waves with a frequency of 1 MHz and maximum amplitude.

The function generator and the Lock-in amplifier are set at 1 MHz. The output of the EOM (Fig. 2.12) must be optimized to produce modulated waves with a frequency of 1 MHz and maximum amplitude. This setting can be done by sending its output to a photodiode and examining the signal using an oscilloscope. The maximum input voltage of the photodiode must be noted because passing this limit might damage the device. To decrease the power, a beamsplitter is recommended. The output of the beamsplitter must pass through a lens that focuses the beam on the sensor of the photodiode. The signal on the oscilloscope must look like a sine wave with a period of $1 \mu\text{s}$ and maximum possible amplitude. To achieve it, the DC bias of the EOM plus the offset and amplitude of the function generator are tuned simultaneously.

The path length of the pump beam must be determined based on our choice for the position of the zero probe delay time. Here, we will consider the case where the zero is in the middle of the detection range. For this case, the translation stage is positioned in the middle of its range and the path length of the probe beam is measured as best as possible. Then, the path of the pump beam from the EOM to the sample is elongated enough to provide the same path length for the pump and the probe beams. Using the last two mirrors (M12 and M13) before mirror M11, the angle (using M13) and position (using M12) of the pump beam are set so that its position on the surface of the sample coincides with the position of the focused probe beam (Refer to Fig. 2.13). At the same time, the pump beam is set to be perpendicular to lens L3; the pinhole and rail method that is discussed in section 2.6.2 may be used to position the beam parallel to the optical table. Once the path of the pump beam is set, the positioning stage (2) carrying the lens is mounted on the table parallel to the pinholes' rail so that the lens is positioned perpendicular to the beam. Consequently, the pump beam is perpendicular to L3 both vertically and horizontally. The coincidence of the focused pump and probe beams can be achieved macroscopically using a CCD camera looking at the surface of the sample. For microscopic adjustments, a PU scan is done over a time range of approximately -1000 and 1000 ps to find the initial jump in the signal that represents the simultaneous arrival of the pump and probe beam. Once the time corresponding to the jump is identified, the "home" position of the translation stage in the Dove software is modified to represent the zero probe delay time. One way for optimizing the initial jump is to set the zero (home) position right before the jump and try to maximize the jump in the magnitude of the signal between zero and ~10 ps. The procedure for optimizing the initial jump is given in the appendix.

(a)



(b)

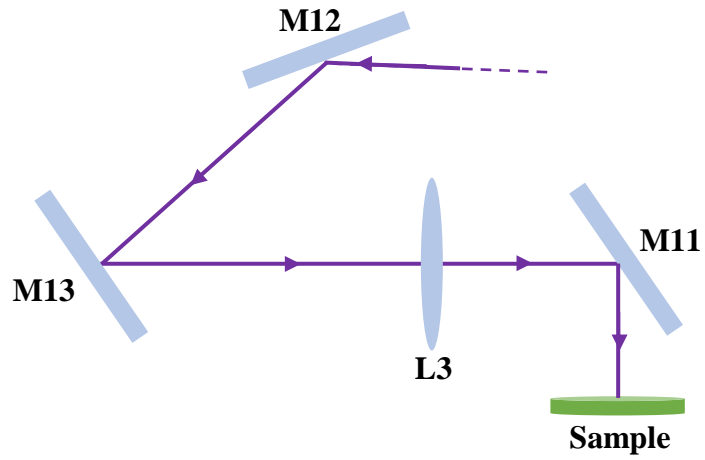


Figure 2.13. (a) Path of the pump beam towards the sample and (b) the schematic of the path. The angle and position of the pump beam are set so that its position on the surface of the sample coincides with the position of the focused probe beam while hitting lens L3 at a normal angle.

2.5. Summary

This chapter introduced the Picosecond Ultrasonics technique and laid out an overview of its operating principles and the experimental apparatus. The basic theories for the generation and detection of acoustic waves using femtosecond lasers are described and the contribution of each of the optical devices used in the setup is explained. Finally, a detailed guide to the alignment procedures is provided.

2.6. Appendix

2.6.1. Steps for aligning the probe beam parallel to the translation stage

- i. Mark the position of the beam on the screen with the translation stage at the closest position to the mirror that needs adjustment (M2 in figure 2.10).
- ii. Move the translation stage to its farthest position from the mirror and monitor the movement of the image on the screen.
- iii. Adjust the angle of the mirror to fix the observed beam walk.

Note 1: It is possible for the angle of incidence to be very far from 90 degrees at the beginning of the alignment causing the beam to move far off from the optics on the second setup during translation of the retroreflectors. To get an initial estimate of the correct angle, one might use a pinhole and adjust the mirror (M2) so that the beam passes through the pinhole with the RR at its closest and farthest positions. Micro adjustments can be done subsequently according to the above steps.

Note 2: Caution must be taken to avoid the creases on the RR's. If the beam ends up at one of the creases, the position of the beam on the mirror (that is being adjusted) may be changed using the mirror on the upstream to provide enough of space between the beam spot and the crease on the RR. Then, adjustments according to the above steps maybe restarted.

Note 3: The space in front of the RR's is very populated with mirrors. So, it is possible for the mirrors to block the path of the beam. One proper strategy would be to send the beam inside the RR at spot 1 (See Fig. 2.14), it will come out of spot 2; send it back in at spot 3, and it will finally come out from spot 4. Therefore, maximum spacing between the mirrors is provided.

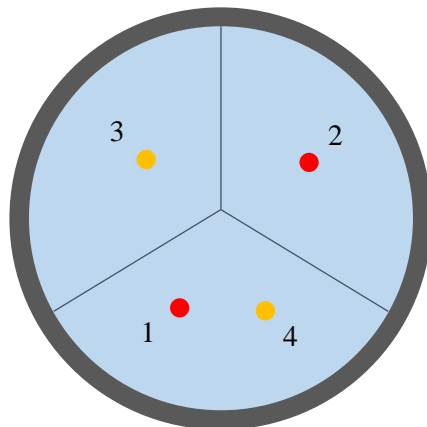


Figure 2.14. Front view of the retroreflector with the beam spots inside. To maximize the spacing between the mirrors, one strategy is to send beam inside the RR at spot 1, it will come out of spot 2; send it back in at spot 3, and it will finally come out from spot 4.

Note 3: The second setup can also be used to specify the divergence of the beam coming out of the collimation rack. Since the initial divergence of the laser beam is unknown, this setup provides a visual way of making sure the beam spot does not expand beyond a reasonable size with respect to the size of the optics used in the setup.

2.6.2. Steps for positioning the probe beam normal to the lens (L1)

- i. The lens is removed and the angle is adjusted using mirror M10 (Refer to figure 2.11); a convenient method for checking the angle is to pass the beam through two pinholes mounted on a rail. The pinholes must have the same height to ensure the vertical alignment and the rail must be fixed parallel to the holes on the optical table to ensure the horizontal alignment.
- ii. Mirror M11 is adjusted by making sure that the ingoing and outgoing probe beams coincide perfectly on the beamsplitter (NPBS).
- iii. Now, the lens is placed normal to the path of the beam with the beam passing through its center. To do so, the positioning stage (1) is fixed parallel to the holes on the table.
- iv. Once the lens is back in place, the position and focus of the beam can be adjusted by moving the lens using the positioning stage (1).

2.6.3. Optimizing the initial jump at zero probe delay time

As explained before, GaAs wafers have specific optical characteristics that facilitates its use for signal optimization. As a starting point, a downstream pump and probe power of about 100 and 20 mW may be used for this type of material. The choice of the power depends on the damage tolerance of the material. If the power is too high, the DC voltage measured by the photodiode becomes unstable, showing that the pump beam is damaging (burning) the material. The optimization process is as follows:

- i. To calibrate the focus of the pump and probe on the sample, one must use the out-of-plane adjustment knobs on the positioning stages (see figures 2.11 and 2.13).
- ii. To calibrate the coincidence, use the knobs for in-plane motion of the positioning stage holding the pump beam lens (L3).
- iii. Perform as many iterations on steps i and ii as necessary to maximize the jump.
- iv. Switch the lock-in amplifier from its default setting of measuring the in-phase component to magnitude measurement and adjust the power of the probe using the halfwave plate to get to the maximum signal. Then, switch back to the default setting.
- v. Repeat step iii.
- vi. Tune the DC bias of the EOM plus the amplitude and offset of the function generator iteratively to maximize the jump. These iterations must not lead to major changes in the settings already done during the optimization of the EOM. Otherwise, it is recommended to repeat the EOM settings with an oscilloscope.
- vii. Repeat steps iii, iv, and vi.

To get reasonable signal-to-noise ratios, an initial jump of above 1 Volt is recommended; depending on the precision of the alignment and the properties of the sample larger maximum values may be achieved. Once the initial jump is maximized, a longer scan (3000 ps or more) is done to evaluate the beam walk. The beam walk appears as a polynomial background component in the signal. Generally, a first order polynomial with a slope less than 10^{-8} V/ps is in the acceptable range. Otherwise, further adjustments on the alignment of the probe beam would be required; it is recommended to start with reoptimizing the alignment on the downstream of mirror M10 and if that did not address the beam walk problem, realignment must be considered from mirror M2 down to the sample.

3. In Situ measurement of the kinetics of phase transformation through picosecond ultrasonics and atomic force microscopy

3.1. Introduction

There are three main approaches in studying the mobility of the phase boundary between the crystalline and lithiated phases in Si:

1. In situ transmission electron microscopy to image the moving phase boundary during lithiation of silicon nanowires at the atomic length scale^{54, 70, 71} (Fig. 1.1c). This approach provides real-time visualization of the atomic-scale processes. However, the electrochemical parameters such as the local potential and the local Li flux within the field of the view of the TEM are usually unknown. As a result, it is not possible to extract quantitative information that can help develop predictive models.
2. Employing planar single crystal wafer samples such as Si wafers in which a planar phase boundary front propagates uniformly through the thickness of the sample. Measurement of the evolution of the sample curvature in real time is used to infer the state of the stress in the lithiated phase. Additionally, ex situ observations of the sample thickness by TEM or scanning electron microscopy is used to measure the final position of the phase boundary³⁹

(figures 1.1a and 1.1b). The simple planar geometry of the sample allows accurate control and measurement of the electrochemical parameters that drive the phase boundary. However, since the position of the phase boundary inside the specimen is unknown during the experiment, additional assumptions about its progression are required to extract the relevant kinetic parameters.

3. Lithiation of micro/nanostructures of the crystalline Si and post-experimental observations of change in their cross-sectional geometry^{60, 70, 108} (Fig. 1.3); the relevant kinetic parameters are extracted through computational simulations by fitting the simulation results with the observations^{16, 53, 58-61}.

Ideally one would like an experimental technique that would combine the geometric simplicity and precise control of the electrochemical parameters in approach (2) with an ability to visualize the progression of the phase boundary in real time as in approach (1). To meet these objectives, we employ a technique that combines PU with an electrochemical cell as a precise in situ method to measure the phase boundary propagation in crystalline Si anodes. The technique can be applied to other materials undergoing phase transformation through moving phase boundaries as well. There have been efforts in the recent literature on alternative approaches to meet these objectives through x-ray⁶⁵ and neutron reflectivity⁶⁶ measurements which report in situ studies on the early stage propagation (approximately 100 nm) of the phase boundary in (100) crystalline Si. The PU techniques can be viewed as a versatile technique that can extend the measurements to arbitrarily large phase propagation distances. Here, in situ picosecond ultrasonics and atomic force microscopy techniques are coupled to directly measure the velocity of the phase boundary propagation through different crystallographic orientations of Si and the resulting volume expansion of the lithiated layer. The proposed integrated technique maintains precise control on

the electrochemistry of the lithiation, avoids assumptions on the kinetics of the reaction, retains the simple geometry of the electrode, and offers a resolution of ~10 nm in determining the position of the phase boundary.

This chapter is organized as follows. First, the in situ PU experiments are explained through lithiation of a {100} oriented Si wafer at a current density of 40 $\mu\text{A}/\text{cm}^2$. The procedures for signal processing, data analysis, and evaluation of the relevant kinetic parameters are also described in this section. It is followed by a comparative study of the phase boundary propagation across two different crystallographic orientations of Si during several galvanostatic and potentiostatic lithiations. Next, the experimental procedures for the combined electrochemistry and AFM experiments for the purpose of evaluating the volumetric strains are described. Finally, the conclusions are presented.

3.2. Experimental technique

3.2.1. Picosecond ultrasonics measurements- Benchmark experiment

A custom electrochemical cell was designed and fabricated in order to perform PU measurements on specimens undergoing electrochemical reactions in real time. A schematic diagram of the cell is shown in Fig. 3.1a. The cells are assembled and sealed in an argon filled glovebox with O_2 and H_2O levels less than 0.1ppm and transferred to ambient environment for performing the lithiation/PU measurements. They are designed to provide perfect isolation from the outside

environment. The working electrode is a Si wafer of {100} orientation, with a 25 nm thick Al film sputter-deposited on one side and a current collector microfabricated on the other side. The thickness of the wafer is chosen to be approximately 40 μm . From the perspective of the signal-to-noise ratio of the echo, a smaller sample thickness is more favorable. However, from the perspective of ease of sample handling and maintaining the mechanical integrity of the sample during phase boundary propagation, thicker samples are preferred. The choice of the thickness is determined as a compromise between these two conflicting requirements. As shown in Fig. 3.1a, the bottom surface of the Si wafer specimen is in contact with the electrolyte and its top surface (the Al film) is glued to a fused silica substrate with a transparent epoxy adhesive. The thickness of the transparent epoxy adhesive is of the order of 5 μm . The epoxy also serves as a protective layer for the Al film by preventing any electrochemical reactions. Additionally, a black insulating epoxy is applied on the periphery of the Si sample to prevent any undesired chemical or electrochemical reactions happening along the lateral surfaces.

The sound pulse from the Al film entering Si is partially transmitted and partially reflected at the moving phase boundary. The transmitted pulse is then reflected at the specimen/electrolyte interface. During electrochemical cycling a thin (10-20 nm)¹⁰⁹ solid electrolyte interphase layer forms at the Si/electrolyte interface. The relatively large travel distance of the acoustic pulse introduces some noise in the signal that makes distinguishing the echoes reflected from the interfaces between the Si/SEI and the SEI/electrolyte difficult and beyond the scope of our experiments. The current collector is a square Ni grid deposited with electron beam evaporation; the grid lines are 30 nm thick and 10 μm wide with a pitch of 200 μm . Lithium metal at the bottom of the cell acts as the counter and reference electrode. A woven Celgard C2500 separator (thickness = 21 μm) is placed between the sample and the lithium slab. A solution of 1.2 molar lithium

hexafluorophosphate in ethylene carbonate/diethyl carbonate (1:2 by weight) is used as the electrolyte. The sample is fixed at the center of a beaker cell made of polyether ether ketone (PEEK) (Fig. 3.1b). The electrochemical cycling of the cell is carried out using an Autolab PGSTAT128N potentiostat. An image of the assembled cell is shown in Fig. 3.2.

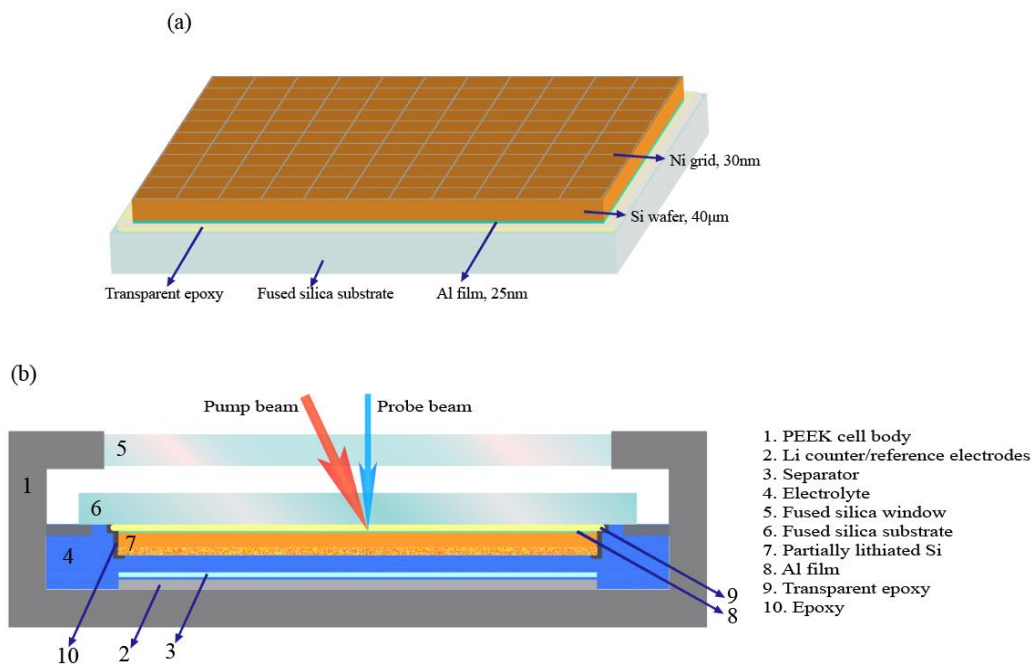


Figure 3.1. (a) Schematic of the sample used in PU measurements. (b) Cross-section of the custom-made cell designed for the PU studies. The images are not drawn to scale.

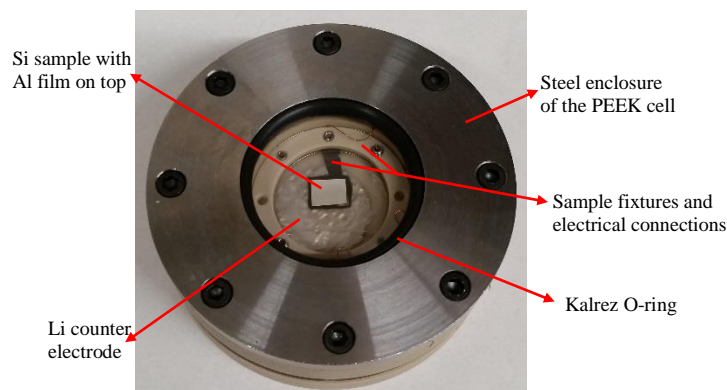


Figure 3.2. a photograph of the assembled cell.

Two types of samples are used for the work presented in this section. The first one was used for measurements outside the electrochemical cell and the second type was used for consecutive electrochemistry/PU measurements. A PU measurement was made on the first sample before lithiation, the recorded signal from which is shown in Fig. 3.3. As explained in the previous chapter, the initial jump in the signal shows the simultaneous arrival of the pump and probe pulses to the surface of the sample and generation of the acoustic wave. Due to the presence of the transparent epoxy, a set of Brillouin oscillations starts at that point. At a delay time of 10.950 ns, another set of Brillouin oscillations appears (arrow II). A peak is observed leading each BO; one at zero probe delay time and another at 10.950 ns (indicated by arrows I and III, respectively). The peak at III marks the time when a change in the reflectivity of the Al film occurred due to the arrival of the returning strain pulse from the free surface of Si. Using the longitudinal sound velocity in the <100> direction of c-Si (8.4 nm/ps), the thickness of the Si wafer in the first sample is found to be 46.00 μm . A PU measurement is always taken on all samples before lithiation to determine the initial thickness of the wafer.

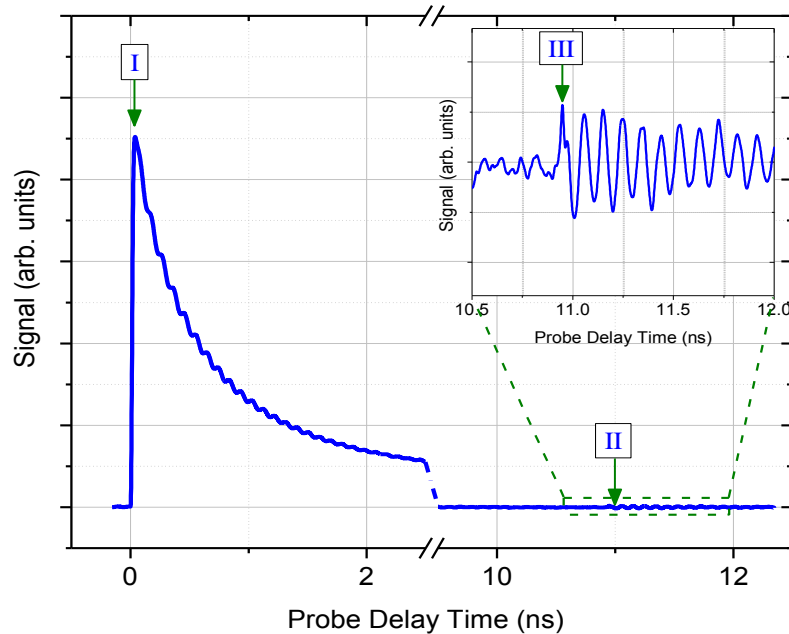


Figure 3.3. Signal recorded from the PU measurement on a pristine Si sample. Arrows I, II, and III mark the initial jump, the second set of BO, and the arrival time of the echo reflected from the surface of the sample.

3.2.2. Signal processing, data analysis, and derivation of the kinetic parameters

To study the progression of the phase boundary of the lithiated layer, a silicon wafer with (100) orientation (sample 2) was lithiated in successive steps, and PU measurements were taken after each step. As shown in Fig. 3.4a, the sample was lithiated through the following procedure:

- i. A constant current was applied to bring the potential down to 100 mV.
- ii. The potential was then held at 100 mV for 1.5 hr to allow the amorphous Li_xSi layer to nucleate and the current density to stabilize.
- iii. A constant current was then applied for all subsequent lithiation steps to drive the phase boundary further.

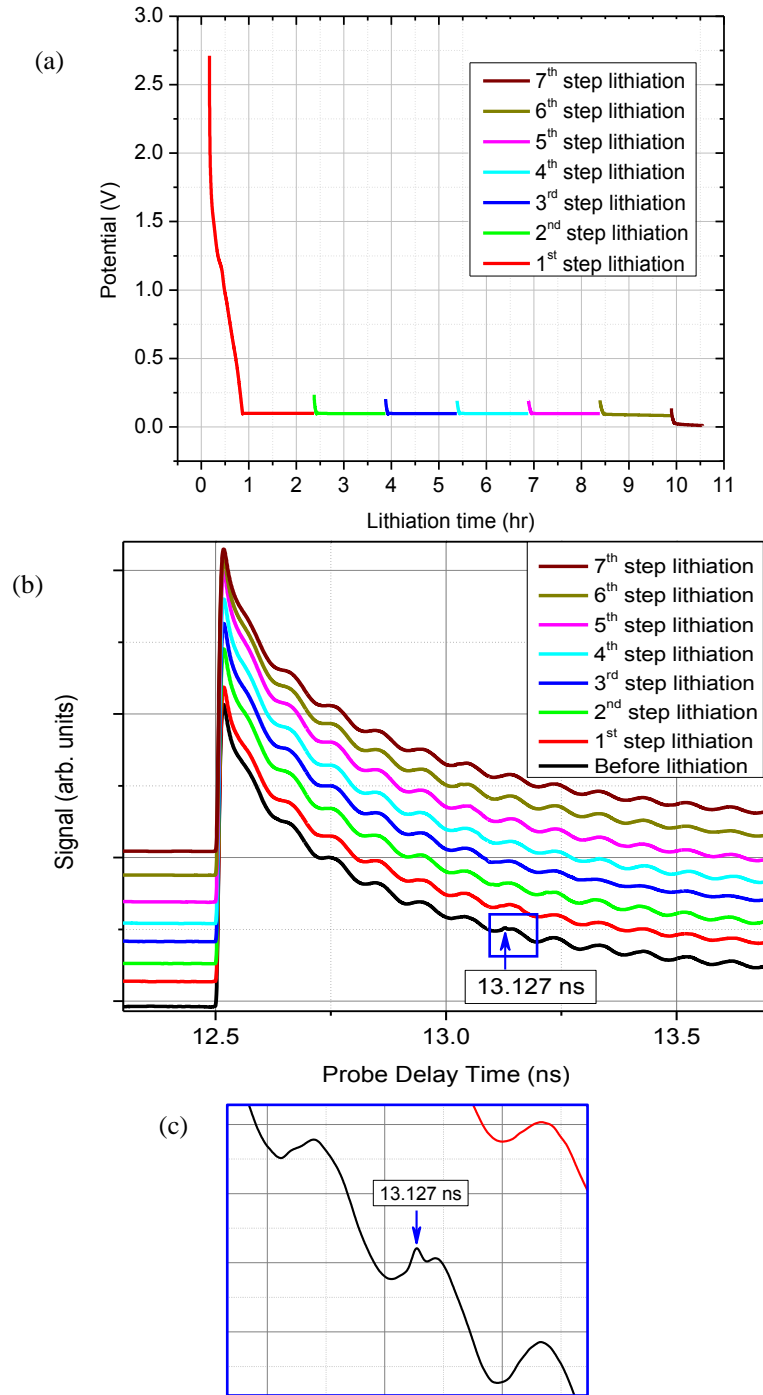


Figure 3.4. a) Lithiation profiles of a (100) oriented Si wafer, b) PU measurements corresponding to each lithiation step, and c) zoomed-in image from (b) indicating the arrival time of the echo; the black line corresponds to the pristine state of the Si wafer. The color of each lithiation step is matched with the corresponding PU measurement. The blue arrow indicates the arrival time of the echo in the pristine state. The signal profiles are stacked vertically for clarity and are not spaced to scale.

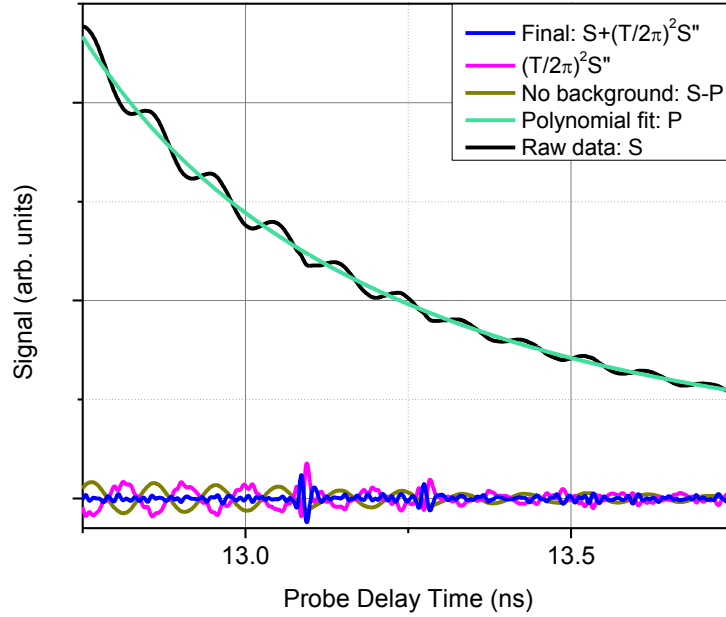


Figure 3.5. Data processing steps. The black line corresponds to the data acquired after the 3rd step of lithiation (S). The 6th order polynomial background fit (P) is shown in green. The olive line represents the data with background removed. After removing the background and oscillations, the final processed data (in blue) is demonstrating two peaks corresponding to the arrival times of the reflected echoes.

Figure 3.4b shows the signal recorded after each lithiation step. The color of each lithiation step in Fig. 3.4a is matched with that of the corresponding PU measurement signal in Fig. 3.4b. A constant current density of $40 \mu\text{A}/\text{cm}^2$ is applied to drive the phase boundary. The blue arrow indicates the arrival time of the echo in the pristine state. Note that sample (2) is thicker than sample (1) and the echo arrival time in the pristine state is at 13.127 ns (Fig. 3.4c) which corresponds to a thickness of $55.13 \mu\text{m}$. As a result, the echo has arrived after the next pump pulse. The BO's and peaks due to the echoes returning from the phase boundary and the free surface are buried inside the BO of the initial jump. The effects of the initial expansion of the Al film, the thermal decay, and the initial BO starting at zero probe delay time must be removed from the recorded data so that the peaks corresponding to the returning pulses become recognizable (Refer

to figure 3.5). To remove the contribution from the initial jump and the thermal decay from the background, a 6th order polynomial is subtracted from the data. This so-called “background fit” does not change the oscillatory component of the signal. The remaining part of the signal (S) has the form of a sinusoidal wave with period $T=96$ ps and a decreasing amplitude. The second derivative (S'') is then calculated and the data is modified by adding $(\frac{T}{2\pi})^2 S''$ to S in order to remove the oscillatory component. This ignores the fact that the amplitude of the oscillations slowly decreases with time, but the effect is small. The BO's starting after the arrival of the reflected echoes are not considered in the data processing since their effects in the result are negligible.

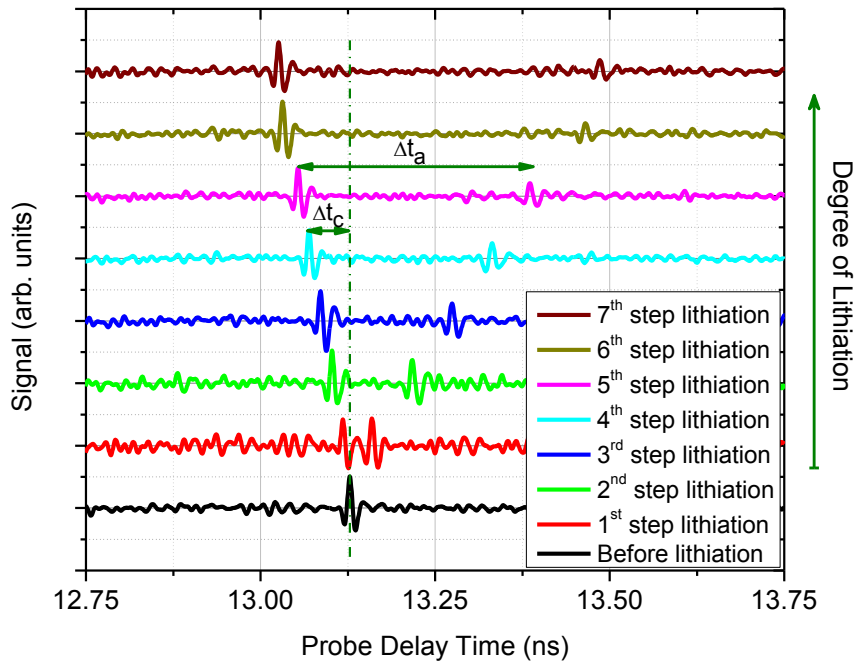


Figure 3.6. Consecutive lithiation/PU measurements on a (100) Si sample. The cell is lithiated galvanostatically at 40 $\mu\text{A}/\text{cm}^2$. The black curve corresponds to the pristine state. Beyond the initial state, the first echo is reflected from the interface of c-Si / a-Li_xSi and the second echo is reflected from the free surface of a-Li_xSi. Δt_c is the advance in the echo arrival time due to consumption of c-Si and Δt_a is the travel time of the sound wave in a-Li_xSi layer after each step of lithiation.

The processed signals obtained from the multi-step lithiation of sample (2) is shown in Fig. 3.6. Each PU measurement after the initial one shows two distinct echoes. The earlier echo is from the crystalline Si (*c*-Si)/ amorphous Li_xSi (*a*-Li_xSi) interface, and the latter echo is from the *a*-Li_xSi/electrolyte interface, which can be considered to be traction free. The plots are displaced vertically for clarity and are not spaced to scale. The shifts (Δt_c in Fig. 3.6) of the earlier echoes correspond to the migration of the phase boundary. By comparing the arrival time of these earlier echoes to the arrival time of the echo before lithiation, one can calculate the thickness of *c*-Si consumed by the phase transformation. The sound velocity for propagation in the <100> direction of crystalline Si (v_c) is known to be 8.4 nm/ps. So, the difference in the arrival time of the first echo in each step from that corresponding to the pristine state gives the thickness of the *c*-Si consumed up to that stage. ($h_c = \Delta t_c \cdot v_c / 2$, where h_c is the thickness of the crystalline Si consumed). The time difference between the arrival times of the two echoes in each plot (Δt_a in Fig. 3.6) is the round-trip time for the sound pulse to travel inside the *a*-Li_xSi layer. The thickness of the amorphous layer can be inferred using the sound velocity in amorphous Si ($h_a = \Delta t_a \cdot v_a / 2$, where, h_a is the thickness of the *a*-Li_xSi layer and v_a is the sound velocity in that layer). However, the current PU results do not have an independent measurement of either h_a or v_a . The thickness of the lithiated Si layer can be determined from the experimentally measured values of the state of charge (x in Li_xSi) and h_c , and the relation between x and the volumetric strain (ϵ_v) of *a*-Li_xSi from the literature ($h_a = h_c [1 + \epsilon_v(x)]$). The value of x can be determined by integrating the current density measurement from the potentiostat during lithiation after correcting it for the contribution for the formation of the SEI. From Nadimpalli et al.⁹, the charge contributed to SEI formation is approximately 0.1C/cm². The average value of x as shown in Fig. 3.7 (red dots) at various stages of the experiment where the PU measurements were made is 3.73. The corresponding volumetric

strain is $2.85^{18, 58}$. The wave velocity is calculated by dividing h_a at each stage with half of the corresponding Δt_a from the PU measurements; the calculated wave speeds (v_a) are also shown in Fig. 3.7 (blue squares). Barring the first data point, there is remarkable consistency in the wave velocity values. The average values of the wave speed v_a in the lithiated layer is 7.15 ± 0.09 nm/ps. In the recent literature, there have been reports of computed dependence of the Young's modulus, the Poisson's ratio, and the density of $a\text{-Li}_x\text{Si}$ as functions of x . These reports employed different computational techniques such as molecular dynamics and density functional theory. There are significant differences in the predictions based on these different techniques. For comparison, we calculate the longitudinal wave speed predicted by the computational results by Shenoy et al.⁷⁶ (for the elastic constants) and Kim et al.⁷⁵ (for the density). Fig. 3.7 shows the computed wave speeds ($v_{a\text{-computed}}$) as well. Note that there is a significant difference between the wave speeds from the PU measurements and those predicted by the computations. The computational predictions are approximately 16% smaller than the observed value in the experiment. This difference might originate from different sources such as the dependence of the computational results to the accuracy of the potentials used in the computations and the approximation used in determining the value of x in Li_xSi in the experiments. Additional refinements to the experimental method to directly determine the value of h_a are necessary for a more accurate measurement of the properties of $a\text{-Li}_x\text{Si}$. These uncertainties are addressed with in situ atomic force microscopy (AFM) measurements, which are described in Section 3.3.

Fig. 3.8 shows the evolution of the thickness of the consumed $c\text{-Si}$ (h_c) and that of $a\text{-Li}_x\text{Si}$ (h_a) as a function of the cumulative charge density (which is proportional to the mass of Li inserted per unit area) during lithiation. In calculating the cumulative charge density from the potentiostat data the contribution from before the formation of the potential plateau is subtracted to partially account

for the charge loss due to SEI formation. It should be noted that, since SEI continues to form during the potential plateau, this correction is an approximation only.

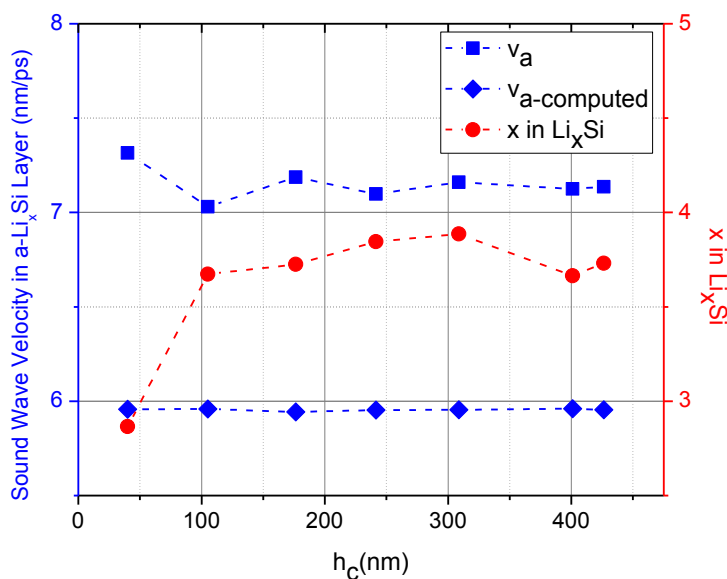


Figure 3.7. Plots of sound wave velocity in $a-Li_xSi$ layer measured in this work (v_a) and that calculated from the properties of $a-Li_xSi$ from the literature^{75, 76} ($v_{a-computed}$) vs the thickness of crystalline Si consumed after each step of lithiation (h_c). Variations of x in Li_xSi with the thickness of consumed crystalline Si are shown with red circles

It is seen that the thicknesses vary approximately linearly with the cumulative charge density and the positions of the peaks corresponding to the echoes returning from the interface of $c-Si / a-Li_xSi$ and the surface of $a-Li_xSi$ can be distinguished readily after lithiating ~ 426 nm of $c-Si$ and producing ~ 1641 nm of $a-Li_xSi$, i.e. the resolution of the method is high enough for detecting lithiated layers with micron-scale thicknesses. The velocity of the phase boundary is an important kinetic parameter that can be extracted from the slope of the thickness of $c-Si$ consumed with the cumulative charge density (Fig. 3.8). At the current density used in the experiment ($40 \mu A/cm^2$), the velocity of the phase boundary is measured to be 12.1 ± 0.2 pm/s. There have been reports of the measurement of the phase boundary velocity during lithiation in the literature. Chon et al.³⁹

inferred the phase boundary velocity from the measurement of the phase boundary position from post-experiment cross-sectional SEM imaging. In (100) oriented Si wafers lithiated at $12.5 \mu\text{A}/\text{cm}^2$, they reported a value of $\sim 3.5 \text{ pm/s}$. Pharr et al.⁵⁹ derived the relative velocities of the phase boundary in different orientations of Si wafer by fitting experimental data from galvanostatic lithiation (current densities in a range of $6.25\text{-}100 \mu\text{A}/\text{cm}^2$) to a modified Deal-Grove model. The value of x in Li_xSi used in their simulations was 3.5. They showed that the velocities of the phase boundary normal to the (110), (111), and (100) planes are 163, 70.5, and 25.4 pm/s, respectively. We used a Deal-Grove type model for thermal oxidation of $c\text{-Si}^{110}$ to extract the reaction rate of Li with crystalline Si at the interface from our experimental observations⁴⁴. The details of this model are given in the appendix. The reaction rate coefficients that can be measured for different crystallographic orientations are necessary to model phase boundary propagation in Si particles with complex geometries in practical applications.

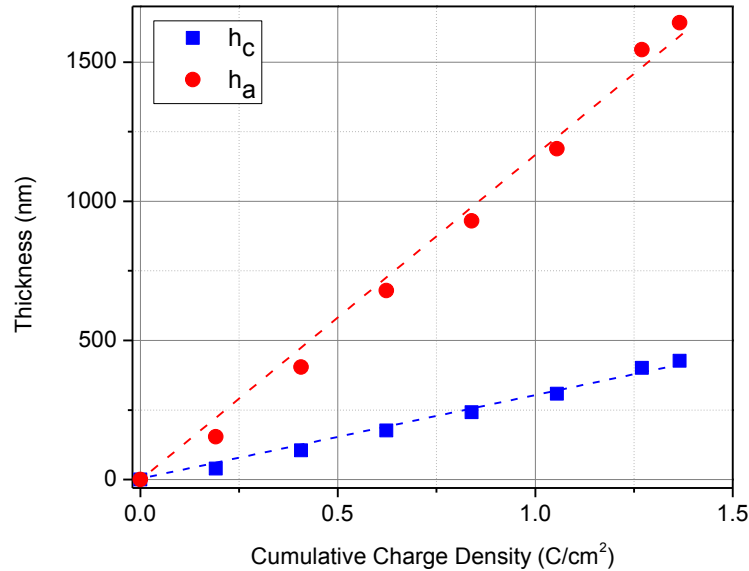


Figure 3.8. Thickness of crystalline silicon consumed (blue squares) and thickness of the amorphous lithiated silicon layer produced (red dots) vs the cumulative charge density for consecutive lithiation/ PU measurements on Si sample with (100) orientation

3.2.3. Comparison between the velocity of the phase boundary propagation through different crystallographic planes

Having established the measurement technique, attention is now turned to a comparative study of the phase boundary propagation kinetics across Si samples with (100) and (110)[‡] orientations. To our best knowledge, there has been no report of a systematic in situ experiment on the rate of progression of the phase boundary in Si with different crystallographic orientations under well controlled potential and current density conditions prior to this work. In situ PU measurements are done using custom-made electrochemical cells (Fig. 3.1b) with three electrodes: Li foil as counter and reference electrodes and *c*-Si as the working electrode. Si wafers with c.a. 40 μm thickness and (100) and (110) orientations are used. The (100) wafers are P-doped with a resistivity of 0.01-0.02 Ohm.cm and (110) wafers are N-doped with a resistivity of 0.005-0.02 Ohm.cm. The sample is submerged in an electrolyte with 1M Lithium hexafluorophosphate in a solution of ethylene carbonate and diethyl carbonate (3:7 weight percent). The rest of the cell specifications are the same as those explained in the previous section.

The first set of experiments focus on galvanostatic lithiation of *c*-Si samples. An example of the signal recorded during consecutive lithiation/PU measurements of a (100) oriented Si wafer at 20 $\mu\text{A}/\text{cm}^2$ is given in Fig. 3.9a. All samples are lithiated with the following recipe. The values in the parentheses are related to the (110) oriented samples:

[‡] The (111) orientation is excluded due to the extreme roughness observed on the surface upon lithiation^{11,12}.

- i. A constant current was applied to bring the potential down from its initial open-circuit value, which is approximately 3.2 V to 120 (140) mV.
- ii. The potential was then held at 100 (120) mV for 1 hr to allow the amorphous Li_xSi layer to nucleate and the current density to stabilize.
- iii. A constant current was then applied for all subsequent lithiation steps to drive the phase boundary further ahead.

The first step is included to partly account for the SEI formation due to the reduction of the electrolyte before the nucleation of the amorphous layer. The cut-off voltages in this step are chosen high enough to avoid nucleation and phase transformation while low enough to minimize the loss due to the SEI formation in the following steps. Three different current densities of 10, 20, and 30 $\mu\text{A}/\text{cm}^2$ are employed on each orientation. The plots corresponding to the evolution of potential during these experiments are given in the appendix (section 3.5.2). An example of the signal recorded and processed after consecutive PU measurement and lithiation at 20 $\mu\text{A}/\text{cm}^2$ on a (100) oriented Si wafer is given in figure 3.9a. The evolution in the thicknesses of the *c*-Si consumed with the lithiation time is shown in Fig. 3.9b with (100) and (110)-oriented samples in red and blue symbols, respectively. The plots exhibit an approximately linear trend conveying that the amount of Si consumed normal to these crystallographic planes increases linearly with the amount of alloyed Li. Linear increase in the thickness of the amorphous lithiated layer under galvanostatic lithiation regime has been reported previously in experimental⁶⁵ and computational⁷⁷ studies. The slope of the lines in Fig. 3.9b represents the velocity of the phase boundary propagation during lithiation of Si. The results for the velocity of the phase boundary propagation through the examined orientations at different current densities are summarized in Table 3.1.

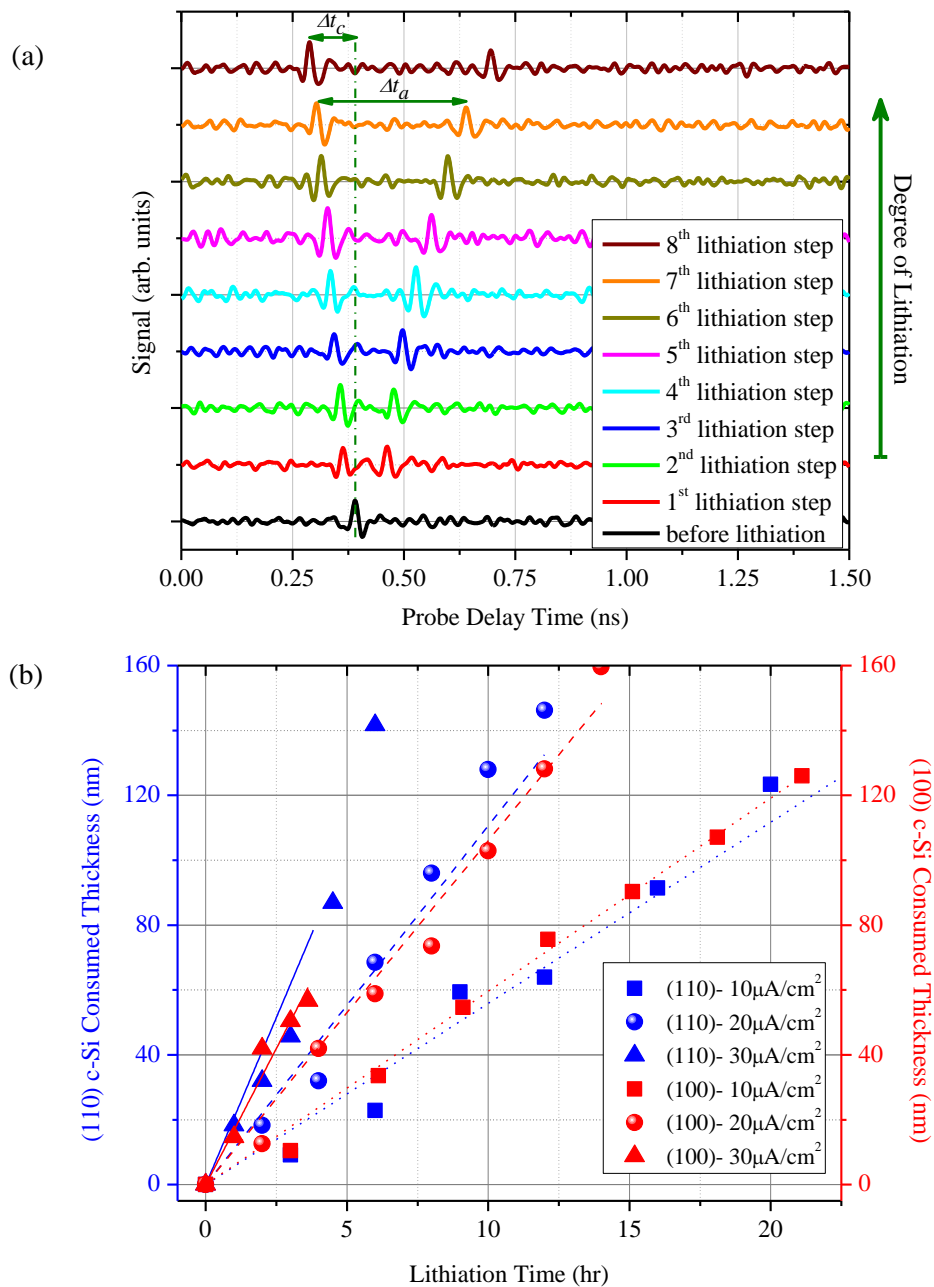


Figure 3.9. a) Consecutive lithiation/PU measurements on a (100) Si wafer lithiated at $20 \mu\text{A}/\text{cm}^2$ b) Thickness of crystalline Si with (110) and (100) orientations (in blue and red, respectively) consumed with lithiation time at three different current densities of 10, 20, and 30 $\mu\text{A}/\text{cm}^2$.

Table 3.1. Velocity of the phase boundary propagation during galvanostatic lithiation of *c*-Si with (100) and (110) orientations at 10, 20, and 30 $\mu\text{A}/\text{cm}^2$ and the average velocity of phase boundary propagation during potentiostatic lithiation of *c*-Si with (100) and (110) orientations at potential values of 80, 95, and 100 mV.

	Velocity of phase boundary propagation (pm/s)					
	Galvanostatic lithiation			Potentiostatic lithiation		
	10 $\mu\text{A}/\text{cm}^2$	20 $\mu\text{A}/\text{cm}^2$	30 $\mu\text{A}/\text{cm}^2$	80 mV	95 mV	100 mV
(100)	1.65±0.03	2.94±0.08	4.67±0.25	35.6	25.7	5.8
(110)	1.72±0.07	3.34±0.11	5.78±0.40	106.1	79.4	19.1

During galvanostatic experiments, the average velocity of the phase boundary propagation is observed to be independent of the orientation at each current density while approximately linearly dependent on the current density; $v_{10}:v_{20}:v_{30} = 1:1.9:3.2$ with v_i representing the average velocity of phase boundary propagation at current density i . A steady-state description of the Li diffusion in a partially lithiated Si sample can be used to find the relation between the flux and the velocity of the phase boundary. In steady-state diffusion of Li through $\alpha\text{-Li}_x\text{Si}$, the Li flux (j) through the bulk is equal to the flux at the surface (figure 3.10) and at the interface between *c*-Si and $\alpha\text{-Li}_x\text{Si}$.

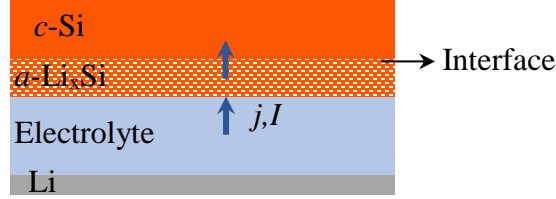


Figure 3.10. Schematic of a steady-state diffusion of Li in a partially lithiated Si anode. The flux at the surface (j) and the current density (I) are constant during galvanostatic lithiation.

Mass balance at the interface relates the flux to the jump in the concentration of Li at the interface (Δc) and the velocity of the phase boundary (v_i) as

$$j = v_i \Delta c \quad (3.1)$$

The jump in the concentration is the driving force of the phase boundary during the first cycle lithiation. In a galvanostatic lithiation, a constant current density (I) is applied at the surface. Flux is related to the current density through $j = -\frac{I}{\rho F}$ where ρ is the mass density of Si and F is the Faraday's constant. Therefore, during these experiments the velocity of the phase boundary is constant and proportional to the current density ($v_i = -\frac{I}{\rho F \Delta c}$).

Previous studies have reported the velocity of the phase boundary propagation in c -Si using different methods. In an ex situ SEM measurement of a (100) Si wafer lithiated at $12.5 \mu\text{A}/\text{cm}^2$, Chon et al.³⁹ inferred a velocity of $\sim 3.5 \text{ pm/s}$ which is 1.77 times larger than the prediction of the results presented here. X-ray reflectivity measurements⁶⁵ on the initial stages of lithiation of Si wafers under galvanostatic lithiation at $25 \mu\text{A}/\text{cm}^2$ has shown a linear increase in the thickness of

the amorphous lithiated silicide layer at a rate of 11.2 pm/s normal to the (100) orientation. By fitting experimental data from the lithiation of Si wafers at current densities of 6.25-100 $\mu\text{A}/\text{cm}^2$ to a modified Deal-Grove model, Pharr et al.⁵⁹ extracted the relative velocity of the phase boundary propagation through (100), (110), and (111) planes to be 1:6.4:2.8. Due to the broad range of current densities chosen for the fitting, it is difficult to directly compare their results with the ones reported here. In a recent study by Seidlhofer et al.⁶⁶, neutron reflectometry is used to conduct in situ studies on the kinetics of the first two cycles of de/lithiation of a (100)-oriented Si sample lithiated at 2 $\mu\text{A}/\text{cm}^2$. It is observed that the lithiated layer grows linearly with time at a rate of ~ 2 pm/s during the lithiation cycles. There are some differences between this result and the measurements reported here. The relative growth rate, i.e. the ratio of the growth rate of the lithiated layer to the lithium flux in their result is 20% smaller than what we observe in our experiments. They report the value of x in Li_xSi to have a gradient from 0.1 to 2.5 from the phase boundary to the sample/electrolyte interface. The PU measurements reported here are not sensitive to any gradient in Li concentration in Li_xSi . The sources of the differences between their results and our observations reported here are unknown at present and remain to be investigated. Kim et al.⁸³ used molecular dynamics simulations with a Reactive Force Field potential on the lithiation of *c*-Si at 1200 K and showed that the phase boundary evolution happens at a relative rate of 1:1.07:1.10 for planes normal to the (100), (110), and (111) orientations. Their results are in close agreement with our observations. Constant current experiments inferred that regardless of the crystallographic orientation of the Si sample, the velocity of the phase boundary propagation is governed by the flux at the surface. In order to distinguish the differences in the thermodynamics of phase transformation normal to different crystallographic planes, the remaining part of this section is devoted to potentiostatic experiments on crystalline Si samples.

In the second set of experiments, Si wafers with (100) and (110) orientations were lithiated potentiostatically at selected potentials of 100, 95, or 80 mV for 1 hour according to the following method:

- i. A constant current was applied to bring the potential down from its initial open-circuit value – about 3.2 V – to 120 (140) mV.
- ii. The potential was then held at the specified potential for 1 hr to nucleate the amorphous Li_xSi layer and move the phase boundary forward.

Cyclic voltammetry experiments on *c*-Si showed that phase transformation in planes normal to (100) and (110) start at 100 and 125 mV, respectively. The plots corresponding to the evolution of current during these experiments are given in the appendix (section 3.5.2). To facilitate comparison between the two orientations, the experiments are done at potentials below 100 mV where both orientations exhibit alloying reactions with Li. Lowering the potential below 80 mV induces extremely high current densities at the surface of the sample that results in crack nucleation. To avoid fracture in the sample and propagation of non-uniform phase boundaries, the potentials are selected to be above 80 mV.

PU measurements are made before and after the potentiostatic lithiation step. The thickness of the *c*-Si consumed can be inferred from the location of the peak returning from the interface of *c*-Si/*a*- Li_xSi in the recorded signals; dividing the thickness values by the lithiation time gives the average velocity of the phase propagation during the potentiostatic lithiation of Si with different orientations (See Table 3.1). The reduction of the velocity by raising the potential can be explained by the lower concentration of Li maintained at the phase boundary at higher potentials. At each potential, the relative velocity of phase boundary propagation is $v_{110}:v_{100} \approx 3:1$ which confirms the higher reaction rate of the planes normal to the (110) orientation compared to other orientations

reported previously^{59, 111}. Such observations in the anisotropy of the reaction rate through different crystallographic planes are well established in the thermal oxidation¹¹² and wet etching process of Si¹¹³. The faster reaction rate normal to the {110} planes is explained to be due to larger channels that result in lower energy barrier for Li diffusion compared to other orientations⁶⁰. Previously, in situ Raman spectroscopy during lithiation of Si wafers through cyclic voltammetry has concluded the same order for the reaction rate; with the <110> direction taking c.a. 5 times more charge than <100> direction²².

Pharr et al.⁵⁹ inferred the relative velocity of phase propagation through different facets of Si nanopillars by fitting the results of a Deal-Grove type model to the experimental report by Lee et al.⁶⁰(See Fig. 1.3). The experiments consisted of ex situ SEM imaging on lithiated Si nanopillars with <100>, <110>, and <111> axial orientations and initial circular cross-sections. The samples were lithiated potentiostatically and different final cross-sections were observed after lithiation which was related to higher diffusion rate in the <110> direction compared to other directions. Although the experiments and modeling provided a good visualization of the kinetics of first cycle lithiation of Si, lack of control on the current density and potential on the surface of the sample made the judgement about the relative kinetics of lithiation through different planes more difficult. In another set of experiments, Astrova et al.¹¹¹ utilized ex situ secondary-ion mass spectroscopy on galvanostatically lithiated Si wafers to assess the Li mobility. By comparing the observed lithiation potentials, they calculated the ratio of the velocity of the phase boundary propagation normal to the (100) and (110) crystallographic planes to be $v_{110}:v_{100} \approx 3.1:1$ which is in good agreement with our observation. Application of the PU technique for studying the lithiation of crystalline Si wafers provides precise control on the electrochemistry by separating the contribution to the thermodynamics and kinetics of lithiation from different planes while releasing

the assumptions on the kinetics through real-time observation of the phenomena. This technique maintains its high resolution during measurement of internal layers with micron-scale thickness, proving it more advantageous for studying samples with multiscale features over the x-ray⁶⁵ and neutron⁶⁶ reflectivity methods that have been applied previously.

3.3. Atomic force microscopy measurements

Volume expansion is a significant characteristic of lithiation of Si. The volumetric strain values reported in the literature are based on experimental measurements on the lithiation of amorphous Si^{18, 109, 114} and first principle simulations^{58, 78, 82}. As explained in the PU experiments sections, the velocity of sound propagation through different crystallographic orientations of Si are well known. However, there is no report in the literature on the velocity of sound propagation in $a\text{-Li}_x\text{Si}$ at different states of charge to facilitate conversion of the PU measurements on the travel time of the echo in $a\text{-Li}_x\text{Si}$ to the thickness of this layer. Therefore, obtaining a complete picture of the kinetics of lithiation in crystalline Si and growth of $a\text{-Li}_x\text{Si}$ under different lithiation conditions is not possible unless the volume expansion due to phase transformation in $c\text{-Si}$ is precisely determined using well-defined experimental techniques. In this section, we present a systematic in situ study on the volumetric expansion of $c\text{-Si}$ by employing the atomic force microscopy technique. These results provide insight into the development of electrodes for high performance lithium ion batteries by controlling the kinetics of lithiation and the expansion rate.

The choice of sample configuration is a critical factor in AFM studies; the structure must facilitate precise measurement of the volumetric strain due to lithiation of crystalline Si while removing the contribution from the thickness of the SEI that forms at the interface of Si and electrolyte. Moreover, it must be under a plane state of stress so that the results are comparable with those obtained during lithiation of Si wafers. A double-step stripe pattern on an insulating silicon oxide layer is designed to satisfy these requirements. A schematic of the silicon on insulator (SOI) wafers etched to the desired pattern for the AFM experiments is shown in Fig. 3.11a. Electrochemical measurements and in situ AFM scans are performed in open cells (Fig. 3.11c) custom designed with three electrodes, Si as the working and Li as the counter and reference electrodes. The cells are assembled and cycled in an argon filled glovebox with O₂ and H₂O levels less than 0.1ppm. Contact mode AFM scans were conducted with silicon nitride probes to provide electrical insulation. Si strips with 50 mm length and 50 μm width (Fig. 3.11b) are fabricated from the device layer using reactive-ion etching. By adding additional etching steps, double-step features are created on the existing stripe pattern, so that the smaller step is ~300 nm and the larger one is ~700 nm in height. The fabrication steps are demonstrated in the appendix. A Ni grid similar to the PU samples is deposited on top of the sample as the current collector and the sample is glued to a fused silica substrate using a black insulating epoxy to prevent reactions on the sides and at the bottom. A solution of 1M LiPF₆ in ethylene carbonate is used as the electrolyte.

The volumetric strain due to lithiation of *c*-Si with different orientations is determined through in situ AFM measurements performed on the device layer of these SOI wafers with (100) and (110) crystallographic orientations. These samples are lithiated potentiostatically according the following recipe:

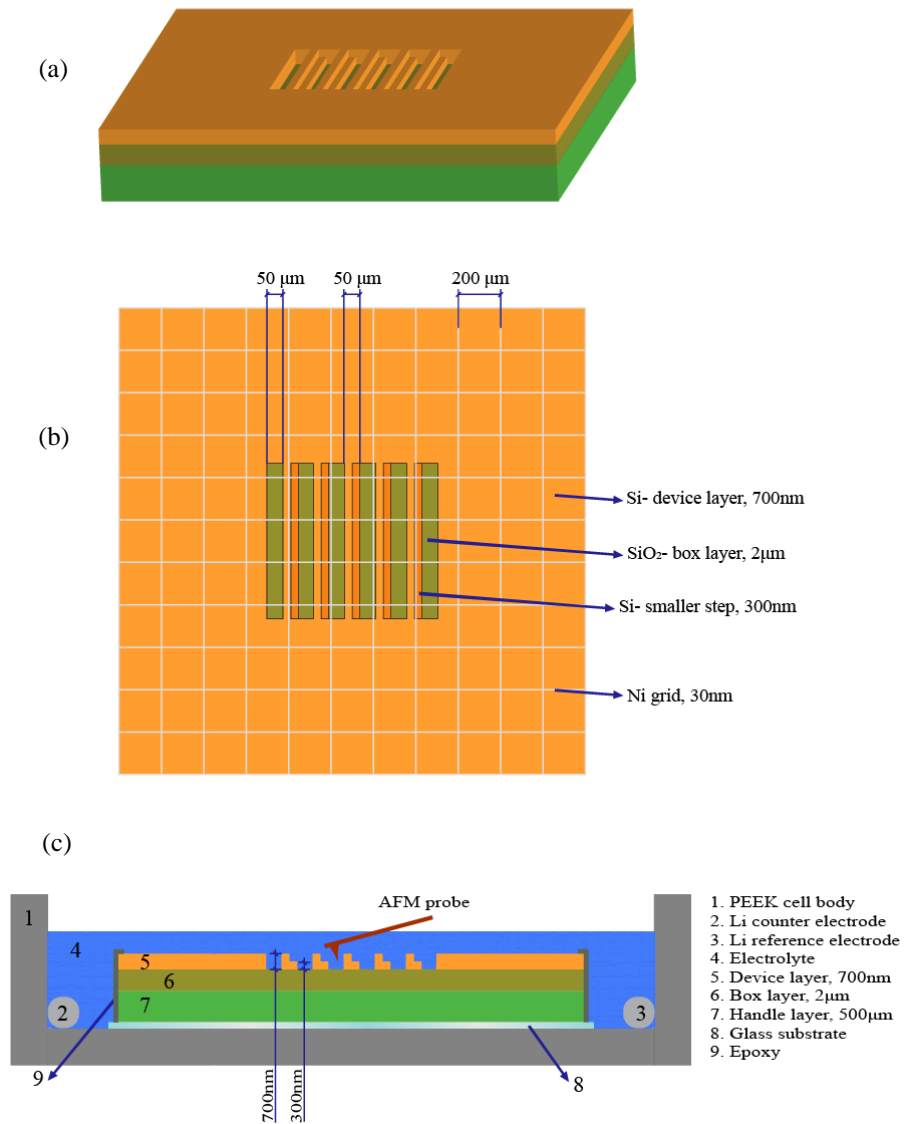


Figure 3.11. (a) Schematic of the samples nanofabricated by etching of SOI wafers, (b) top view of the sample, and (c) cross-section of the custom-made cell designed for the in situ AFM studies. The images are not drawn to scale.

- i. The potential is initially brought down to 120 (140) mV for samples with {100} ({110}) orientations by applying a constant current.

- ii. Potentiostatic lithiation at 80, 95, and 100 mV voltages are performed until the current goes below 1 μ A and the Si features on the insulating oxide layer of the SOI wafer are fully lithiated.

To be consistent with the potentiostatic lithiation process used in the PU experiments (section 3.2.3), the same cutoff and lithiation potentials are employed in these AFM studies.

AFM scans are performed at the pristine state and after full lithiation. An example of the profiles scanned using in situ atomic force microscopy is provided in figure 3.12; figure 3.12a demonstrates the strip in its pristine state before lithiation and figure 3.12b shows the same region after full lithiation. During these scans, we are interested in the height difference between the large and the small step. The ratio of the measured height difference after lithiation to its value before lithiation gives the volume expansion ratio. The advantage of this type of sample design is that the double-step configuration facilitates a precise and direct measure of the volumetric strain in Si while excluding the thickness of the SEI layer that inevitably forms on top of the Si steps during lithiation¹⁰⁹.

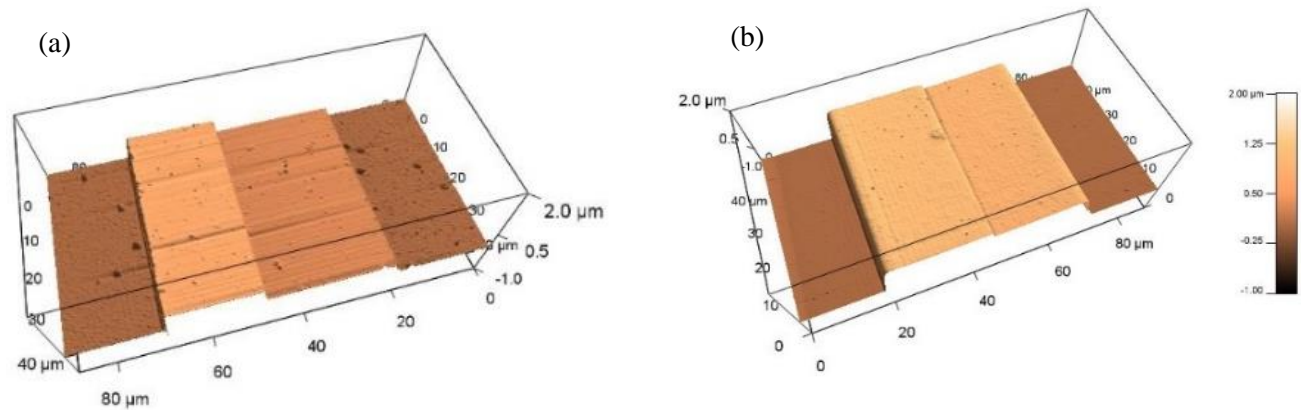


Figure 3.12. AFM scan of the topography of a Si strip a) at the pristine state and b) after full lithiation.

The values of the volumetric strain due to lithiation of planes normal to the $\langle 100 \rangle$ and $\langle 110 \rangle$ directions at the applied lithiation potentials are given in Table 3.2. At lower potentials, higher concentration of Li is available for reaction at the phase boundary, i.e. the driving force for the alloying reaction at the phase boundary becomes larger. Hence, at lower potentials Si transforms at an elevated rate into an amorphous silicide with higher Li content and larger volume⁷⁵. Comparing the results of the volumetric strain normal to the (100) and (110) facets, one can imply that the magnitude of volume expansion is independent of orientation. The observed anisotropic volume expansion behavior observed during potentiostatic lithiation of Si nanopillars⁶⁰ (See Fig. 1.3) could be attributed to the differences in the thermodynamics of the lithiation through the exposed facets of the nanowires. Since the potential and current densities applied on different faces with different crystallographic orientation were not well-controlled in those experiments, comparison between the kinetics of lithiation through these faces becomes complicated. Additionally, differential capacity experiments on single crystalline Si wafers have shown that two-phase characteristics occur at higher potentials for the (110) facet than others, so at each

potential larger lithiation and growth rates are expected normal to {110} surfaces. In the same way, during galvanostatic lithiation of Si microstructures²² with multiple crystallographic faces, the (110) oriented planes start reacting with Li at higher potentials. The alloying process through these (110) planes keep the potential above the limit needed by other planes to pass the energetic barrier for nucleation. Therefore, a lower reaction rate is observed in the <111> direction than that of <110> direction. Our reported volume expansion ratios show good agreement with previous studies on the lithiation of amorphous Si^{18, 82}.

Previous experimental reports on the volume expansion due to lithiation of Si are restricted to studies on the alloying reaction of amorphous Si with Li. Choi et al.¹¹⁴ made cross-sections on lithiated Si thin film using ex situ focused ion beam (FIB) to establish the relation between the volume expansion and the state of charge. Considering the charge loss to the SEI, they reported a volume change ratio of 2.8 during galvanostatic lithiation at 100 $\mu\text{A}/\text{cm}^2$. Yoon et al.¹⁰⁹ investigated the effect of composition of electrolyte on the volume expansion of amorphous patterned Si strips using in situ AFM studies. They inferred an average volume expansion ratio of c.a. 3.75 and measured the thickness of the SEI during their experiments. The relation between volume expansion and lithiation potential during cycling of patterned amorphous sputter-deposited Si was reported in a study by Beaulieu et al.¹⁸. They performed in situ AFM studies during galvanostatic de/lithiation cycles and observed reversible volume change during charge and discharge cycles. The thickness of the SEI layer was not included in their volume expansion measurements. $\text{Li}_{3.75}\text{Si}$ is reported to be the fully lithiated amorphous stoichiometry that can be reached at room temperature with an associated volumetric strain of c.a. 300%^{18, 58}.

The experimental reports on the charge loss to SEI and other side reactions vary significantly depending on the sample configurations, cell geometries, composition of the electrolyte, etc. For

example, the reported values for the charge loss to SEI during lithiation of Si nanowires²⁴ is 31% whereas this value increases to 40% during lithiation of Si thin films⁹. On the other hand, first principle calculations by several groups inferred consistent values for the relation between the Li content and the volumetric strain due to lithiation of Si with different crystallographic orientations^{58, 75, 77, 82}. Consequently, we used the latter calculations to relate the observed volumetric strains in the a -Li_xSi layers to their Li content (x) at various potentials (refer to Table 3.2). In our experiments, the fully lithiated Si exhibited almost the same volumetric strain under the same potential in both examined crystallographic orientations. The first principle calculations predict similar volume expansions for the same Li contents (x in Li_xSi) in the $\langle 100 \rangle$ and $\langle 110 \rangle$ crystallographic direction. Hence, the constant concentrations of Li provided at the surface of Si during potentiostatic lithiation induces the production of a -Li_xSi with the same Li content under the same volumetric strain conditions regardless of the crystallographic orientation.

Integration of in situ AFM measurements of the volume expansion during lithiation of c -Si with PU experiments provide a comprehensive picture of the kinetics of lithiation of crystalline Si and formation of the amorphous silicide layer. Our studies suggest that:

- i. Due to lack of existing literature on the velocity of sound propagation in a -Li_xSi at different states of charge, the measured travel time of the echo in the lithiated layer during lithiation of Si could not be directly converted to the thickness of the lithiated layer. To address this issue, we designed in situ AFM experiments to get solid experimental results on the growth of the a -Li_xSi layer and the corresponding volume expansion.
- ii. The thermodynamics of the lithiation normal to different crystallographic planes govern the alloying reaction of the Li-Si system. Accurate comparison between the alloying

processes through different planes is possible through experiments conducted on samples with simple geometries to separate the contributions from different orientations. The choice of sample configuration is critical in maintaining well-defined electrochemical conditions.

- iii. The AFM experiments revealed that the volumetric strain through different crystallographic orientations and the resulting stoichiometry of the amorphous silicide are determined by the concentration of Li at the surface of the electrode, i.e. the applied potential during the experiment dictates the characteristics of the transformed Si.
- iv. At lower lithiation potentials, a larger current density and concentration of Li is available at the surface of the electrode which lead to faster reaction rate at the phase boundary and larger volume expansion accompanied with higher Li contents in the a - Li_xSi layer.

Our well-controlled experimental technique is able to distinguish between the underlying thermodynamic mechanisms and provides a precise tool for comparing the kinetics of Lithiation through different planes. It paves the way towards extraction of accurate kinetic parameters, which are necessary for modeling the phase boundary propagation in arbitrarily shaped Si particles and nanowires.

Table 3.2. Volumetric strain (ϵ_v) and Li content after the full lithiation of (100) and (110)-oriented Si at constant potentials of 80, 95, and 100 mV.

	(100)		(110)	
	ϵ_v	x in Li_xSi	ϵ_v	x in Li_xSi
80 mV	2.84	3.89	2.72	3.73
95 mV	2.47	3.38	2.41	3.30
100 mV	1.98	2.72	1.86	2.55

3.4. Conclusions

Study of phase boundary kinetics in electrode materials requires accurate measurement of phase boundary velocity under well-defined electrochemical conditions. In this chapter, we have introduced a non-destructive, in situ method that combines the picosecond ultrasonic metrology technique with an electrochemical cell for real-time measurement of the migration of the phase boundary between crystalline Si and amorphous Li_xSi during lithiation under well controlled potential and current density conditions with a resolution of about ten nanometers. Using this method, essential parameters of the phase propagation such as consumption of the crystalline Si and growth of the amorphous Li_xSi during lithiation are precisely determined and the position of the phase boundary at different states of charge is monitored. It is observed that the phase boundary propagates approximately linearly with charge density at a rate of ~ 12 pm/s under the current density of $40 \mu\text{A}/\text{cm}^2$. Lithiation of Si under the conditions of this experiment has transformed Si to Li_xSi with x equal to 3.73 and a corresponding volume expansion ratio of 3.85. Using the volume expansion ratio and the travel time of the echo inside $a\text{-Li}_x\text{Si}$ after each step of lithiation, the average longitudinal velocity of sound propagation in the lithiated layer is calculated to be about 7.15 nm/ps. Direct measurement of the phase boundary velocity facilitates extraction of the kinetic parameters of the lithiation through setting up and solving a phase boundary model. We have adopted a simple Deal-Grove type model to estimate the reaction rate coefficient ($4.5 \times 10^{-5} \frac{\text{mm}^4}{\text{mol.s}}$) and the growth rate of $a\text{-Li}_x\text{Si}$. The signal-to-noise ratio in the lithiated layer is high enough to resolve layers with micron scale thicknesses.

We used this method, in combination with in situ AFM experiments, to study the phase transformation in Si due to diffusion of Li through two different crystallographic orientations under multiple driving forces imposed during galvanostatic and potentiostatic lithiation. The velocity of the phase boundary and volumetric strains in the lithiated layer under these lithiation processes are reported. This novel approach can maintain precise control on the electrochemical parameters while retaining a simple planar geometry and avoiding assumptions on the kinetics of the lithiation. A double-step stripe-patterned crystalline Si sample is employed to eliminate the effect of the SEI thickness on the volume expansion measurements. Based on the experimental observations, we can conclude that:

- i. Lithiation at constant current results in nearly identical phase transformation behavior in planes normal to $\langle 100 \rangle$ and $\langle 110 \rangle$ directions with equal velocity of the phase boundary propagation that is directly proportional to the current density.
- ii. During constant potential experiments, the velocity of the phase boundary propagation is 3 times faster in the $\langle 110 \rangle$ crystallographic direction than the $\langle 100 \rangle$ direction.
- iii. These crystallographic orientations can host approximately the same amount of Li (same x in Li_xSi) at their fully lithiated state at every specified lithiation potential.
- iv. The Li content and the volume expansion ratio increase as the lithiation potential decreases.

A more detailed analysis of the phase transformation behavior during lithiation of crystalline Si and the relevant kinetic parameters is conducted in the next chapter by adopting a moving phase boundary model and calibrating it to our experimental data.

3.5. Appendix

3.5.1. Deal-Grove model for the diffusion of Li in a -Li_xSi

A simple steady state model might be useful in estimating the growth rate of the Li_xSi layer. Under a steady-state assumption (shown in the schematic in Fig. 3.13), the flux of Li through the electrolyte/sample interface (J) is equal to those passing through the a -Li_xSi layer (J_1) and the a -Li_xSi/ c -Si interface (J_2). the flux (J) is equal to the current density (I) divided by the elementary charge (q). conservation of mass requires that the change in the thickness of a -Li_xSi layer (dh_a) during time dt is equal to $dh_a = J_2 \cdot dt \cdot V_{Li_xSi} / x$ where $V_{Li_xSi} = (1 + \epsilon_v) V_{Si}$ is the volume of a -Li_xSi and V_{Si} is the volume occupied by each Si atom in c -Si. Rearranging the equation gives:

$$\frac{1}{I} \frac{dh_a}{dt} = \frac{V_{Li_xSi}}{q \cdot x} \quad (3.A)$$

$\frac{1}{I} \frac{dh_a}{dt}$ is the corresponding value of the growth rate of the a -Li_xSi which is $\sim 1.2 \frac{\mu m}{C/cm^2}$ at a current density of $40 \mu A/cm^2$ (the slope of h_a versus the cumulative charge density in Fig. 3.8). The right-hand side of Equation 3.A gives a growth rate of $1.3 \frac{\mu m}{C/cm^2}$ which is in close agreement with the experimental observations. In the study by Cao et al.⁶⁵, Si wafers with (100) orientation are lithiated at a constant current density of $25 \mu A/cm^2$ while x-ray reflectivity measurements are done on the sample. It was reported that the growth rate of the a -Li_xSi layer is about $120 \frac{nm}{C/cm^2}$. Note

that the current density in their study is approximately 0.63 times the current density in our study, yet their growth rate was smaller by a factor of approximately 10. The value of x in Li_xSi is reported to increase during phase transformation from 0.17 to 3.75 and $\text{Li}_{3.75}\text{Si}$ is the final product of lithiation. The PU measurements reported here are not sensitive to the fine structural details of different layers. The difference between their observations and the present report could be due to any unaccounted charge losses to side reactions in the experiments and other unknown sources, which remain to be investigated further.

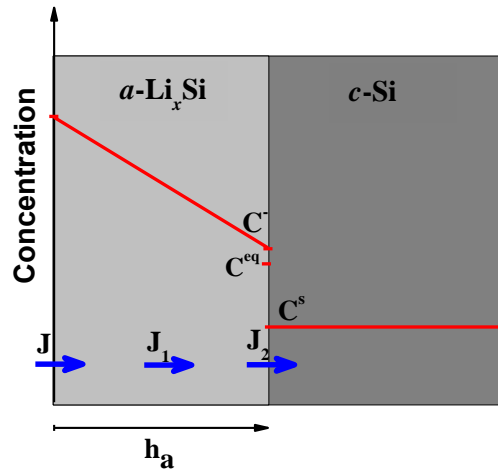


Figure 3.13. Schematic of the steady-state model for moving phase boundary at the interface of $a\text{-Li}_x\text{Si}$ and $c\text{-Si}$. Concentration profile is shown with red lines. C^- , C^{eq} , and C^s are the concentration of Li at the $a\text{-Li}_x\text{Si}/c\text{-Si}$ interface, equilibrium concentration at the interface of $a\text{-Li}_x\text{Si}/c\text{-Si}$, and solubility of Li in $c\text{-Si}$, respectively.

We used a Deal-Grove type model for thermal oxidation of $c\text{-Si}$ ¹¹⁰ to extract the reaction rate of Li with crystalline Si at the interface from the experimental observations⁴⁴ (A schematic of the model is given in Fig. 3.13). Assuming the solubility of Li in crystalline Si (C^s) to be negligible compared to the concentration of Li at the $a\text{-Li}_x\text{Si}/c\text{-Si}$ interface (C^-) in the amorphous layer, C^- can be calculated as J_2/v . The velocity of the phase boundary and the supersaturation at the interface are related through $v = K(C^- - C^{eq})$, where K is the reaction rate coefficient and C^{eq}

the equilibrium concentration at the interface of a -Li_{*x*}Si/ c -Si in the amorphous layer; this quantity can be estimated as $C^{eq} = x/V_{Li_xSi}$. Using these concentrations and the velocity of the phase boundary, the reaction rate coefficient K is estimated to be $4.5 \times 10^{-5} \frac{mm^4}{mol.s}$. The constant velocity of the phase boundary propagation under the experimental conditions reported here suggests that lithiation of c -Si in this study is interface-reaction-rate controlled. Note that the direct measurement of the phase boundary velocity through PU measurements facilitates extraction of the reaction rate coefficient without complicated computational simulations.

3.5.2. Evolution of potential/current during galvanostatic/potentiostatic measurements

Figures 3.14a and 3.14b demonstrate the evolution of potential during consecutive galvanostatic lithiation/PU measurements on (100) and (110) oriented Si wafers.

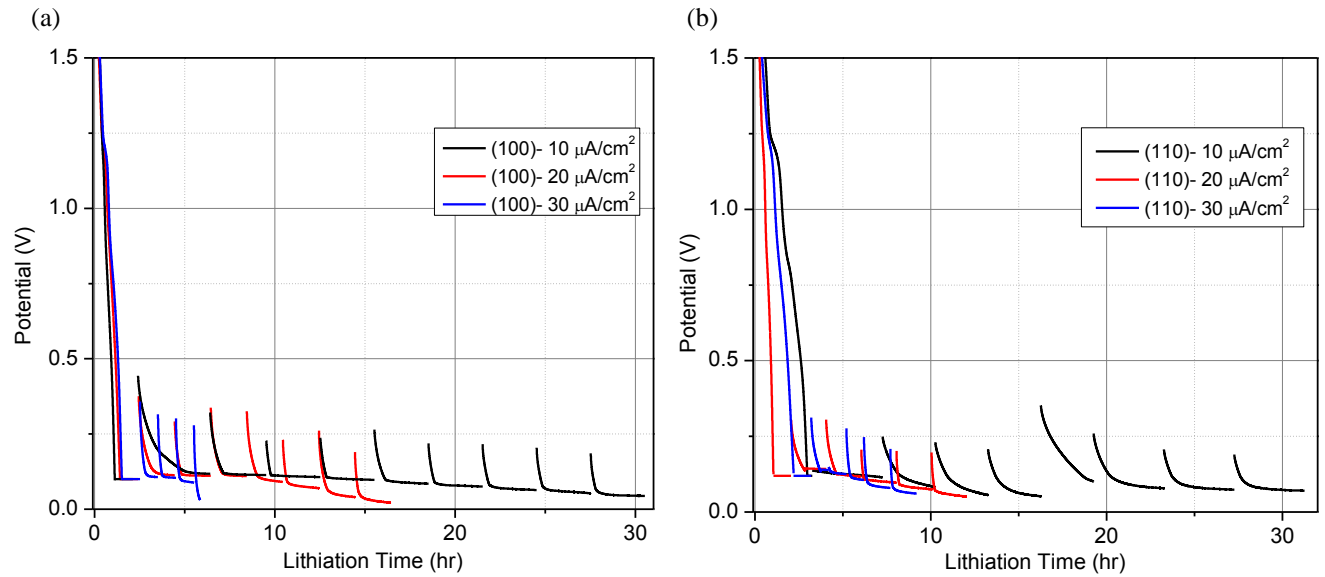


Figure 3.14. Evolution of potential during consecutive galvanostatic lithiation/PU measurements on (100) and (110) oriented Si wafers.

Figure 3.15 demonstrates the evolution of current during potentiostatic lithiation/PU measurements on (100) and (110) oriented Si wafers.

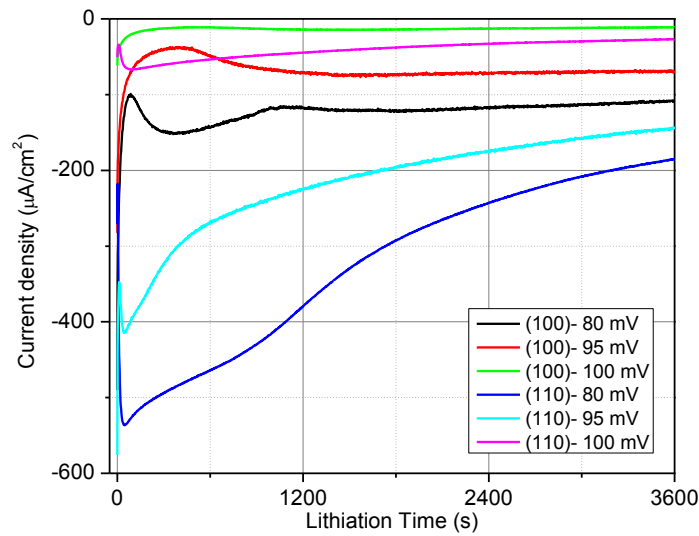


Figure 3.15. Evolution of current during potentiostatic lithiation/PU measurements on (100) and (110) oriented Si wafers.

3.5.3. Fabrication procedure for AFM samples

SOI wafers with 4" diameter are cut into 1.5×1.5 cm pieces using a dicing saw. The thickness of the device, box, and handle layers are 2 μm, 1 μm, and 500 μm, respectively. The process to create double steps on the device layer of the SOI pieces is as follows (See also Fig. 3.16):

- i. Photoresist S1818 is spin-coated on the device layer and a stripe pattern is created on the photoresist using a photolithography mask with a stripe pattern.
- ii. The sample is hard baked and etched using an inductively coupled plasma - reactive ion etching (ICP-RIE) tool.
- iii. The remaining part of the photoresist is removed, and another etching step is added.

The combined etching time of the steps (ii) and (iii) must be optimized based on the conditions of the RIE device in order to produce a stripe pattern with step height of 700 nm.

- iv. In order to create the double-step pattern, step (i) is repeated with the photolithography mask aligned to have an offset of 25 μm in the direction normal to the stripe pattern.
- v. The sample is hard baked, and another etching step is added to reduce the height of the exposed part of the step to 300 nm.

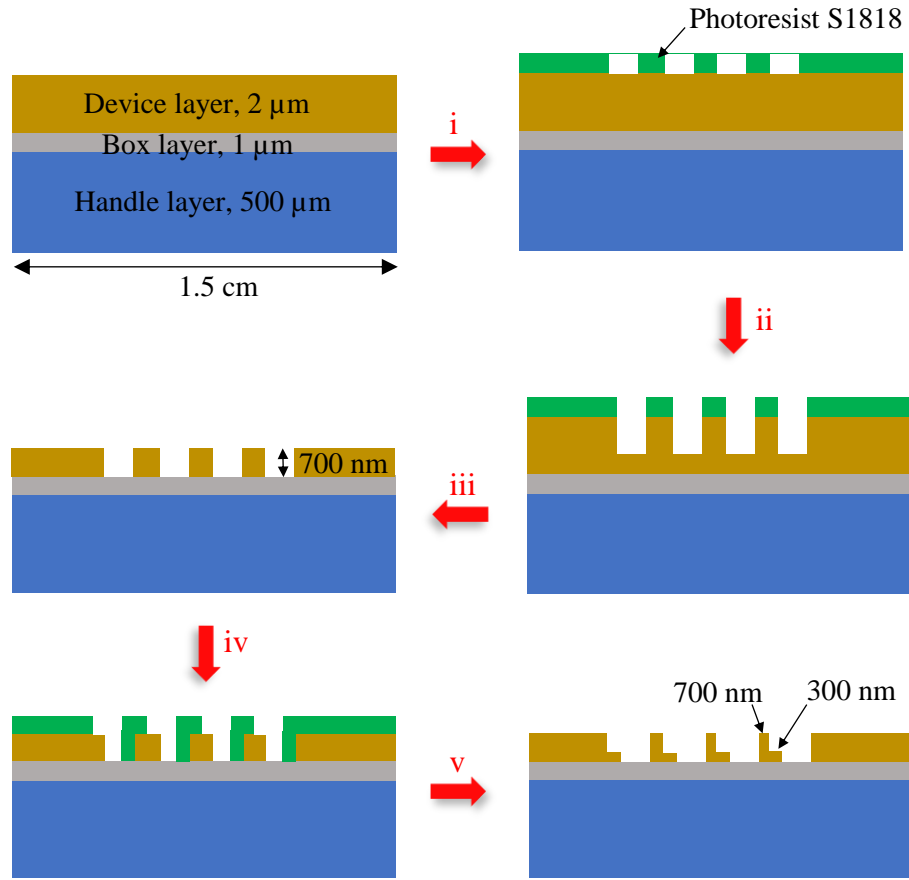


Figure 3.16. fabrication process for creating a double-step stripe pattern on the AFM samples. Starting from an SOI wafer, multiple steps of photolithography and ICP etching are applied to create double-step features with 700 nm and 300 nm heights. The numbers on the red arrows refer to the steps explained in section 3.5.3. The photoresist layers deposited on the sample during photolithography are shown in green. The cross-sections of the samples are not drawn to scale.

To create the Ni grid, S1818 photoresists is spin-coated on the surface of the sample and a mask aligner tool is used to fabricate a grid pattern on the photoresist. A Ni layer with 30 nm thickness is deposited on the surface using the e-beam evaporation technique. Finally, the sample is cleaned and secured to a glass substrate with an epoxy adhesive.

4. Phase-field modeling of the phase transformation in Si due to diffusion of Li

4.1. Introduction

Silicon is one of the promising candidates for replacing graphite anodes because of its superior gravimetric capacity (3579 mAh/g) which is tenfold that of graphite. During lithiation, Lithium atoms initially fill the tetrahedral interstitial sites⁵⁵. Further lithiation results in breaking the bonds between Si atoms, transforming the crystalline phase to an amorphous one. The final stoichiometry of this amorphous phase at room temperature is $\text{Li}_{3.75}\text{Si}$ with a volume about 4 times^{13, 115} that of the original lattice. The in-plane compressive stresses that arise in the lithiated layer due to the volumetric strain associated with the phase transformation have been shown to be large enough to result in plastic strains^{16, 19, 24}. Upon delithiation, the stresses become tensile causing fracture of the anode and loss of active materials. Additionally, fracture exposes fresh surfaces to the electrolyte, which is passivated by the formation of solid electrolyte interphase (SEI) that further decreases the available lithium and the cycling efficiency of the battery. Moreover, stresses contribute to the chemical potential of lithium, thus influencing the driving force for diffusion. Diffusion coupled with stresses in Li ion batteries is studied in the recent literature^{85, 116}. Several

atomistic simulations have been reported to simulate Li insertion in Si^{76, 117, 118}. Computational models employing the finite element method and other numerical techniques have been developed to capture the large plastic deformations observed during charge/discharge cycles^{15, 53, 73, 93, 94}. When the free energy of the system depends on the gradients of its state variables, Fickian description of diffusion is not valid anymore and new kinetic theories are required. The phase field modeling approach used in this study employs a continuous phase field (state) variable that is a function of time and position and its behavior follows the transport equations. The interface between the two phases is described by the gradients of the phase field variable varying between its equilibrium values in the neighboring phases. The method attributes a diffuse region with a finite width to the interface where the phase field variable changes smoothly between its equilibrium values. The limit of an infinitesimal interface width can recover the sharp interface description of the system. The advantage of a phase field model to the sharp interface description is that the location of the interface emerges from the solution to the phase field variable without posing an extra boundary condition or explicit need for tracking it. The Cahn-Hilliard¹¹⁹⁻¹²³ model is a phase-field description for the distribution of a conserved variable, e.g. local lithium concentration. This approach has been used by Han et al.¹²⁴ to study the non-Fickian effects on the kinetic coefficients during GITT and PITT experiments. Singh et al.¹²⁵, Cogswell et al.¹²⁶, and Bai et al.¹²⁷ studied the phase separation due to diffusion of Li in the olivine structure of LiFePO₄. Hulikal et al.⁵² modified the classical Cahn-Hilliard approach to extract the kinetic parameters of phase transformation in tin anodes used in Li ion batteries. Anand⁹⁵ developed a Cahn-Hilliard type theory which combined diffusion with finite strains and Di Leo et al.⁷² implemented the theory in a finite element model to investigate the spinodal decomposition and diffusion in electrode particles.

A Cahn-Hilliard model is used in this chapter to describe the phase transformation behavior of crystalline Si with different crystallographic orientations during the first cycle lithiation. By comparing the predictions of the model with our experimental data, the parameters of the model are calibrated. The classical Cahn-Hilliard model are applicable to diffusion-controlled phase transformation behavior where the phase boundary has infinite mobility. We use a modified version of the Cahn-Hilliard model that incorporates the non-equilibrium behavior of the interface by introducing finite mobility to the interface through a concentration-gradient dependent mobility¹²⁸. The calibration of the model identified the free energy potential of the Li-Si system, the mobility of Li in the lithiated phase, the surface reaction parameters from the Butler-Volmer equation, and the interface mobility parameter. The contributions of stresses and finite deformations in the phase transformation behavior are integrated into the model. The concentration, chemical potential, stress, and plastic strain during nucleation and phase propagation inside crystalline Si samples with different crystallographic orientations are investigated in details and comparisons are provided with the experimental observations. To the best of our knowledge, this is the first time that the interface mobility parameter is determined for the alloying reaction between Li and *c*-Si. A sharp interface limit of the phase field equation can help in understanding the interface behavior, extracting the model parameters, and determination of the boundary conditions at the interface. Therefore, to assess the interface parameters and the dissipation of the energy due to its propagation, an energy-based sharp-interface model is compared with the results of the perturbation analysis of the governing equations of the Cahn-Hilliard model. Finally, a discussion on the dynamics of the processes involved in the phase propagation and the energy efficiency of the electrode is provided.

4.2. Model of a half cell with crystalline Si anode

We are interested in modeling the lithiation of Si in an electrochemical half cell. The model starts with a pure crystalline Si phase. The difference in the electrical potential delivers the driving force for the electrochemical reaction at the interface of electrolyte/electrode and diffusion of Li atoms into the Si lattice. Initially, the Li atoms occupy the tetrahedral interstitial⁵⁵ sites until the molar density ratio of Li to Si reaches a critical value where a metastable amorphous phase nucleates and starts propagating. This critical concentration is reported to be about 0.1^{55, 129}. Lithiation of Si is accompanied by compressive biaxial stresses as the crystalline Si substrate prevents lateral expansion of the lithiated layer. The electrode, however, is free to expand in the out of plane direction causing a volume expansion ratio of about 400% at the fully lithiated state ($\text{Li}_{15}\text{Si}_4$). We adopt the one-dimensional Cahn-Hilliard¹¹⁹ phase field model previously described by Hulikal et al.⁵² and calibrate the kinetic parameters with our experimental data. Our model predicts the Li transport, phase nucleation and propagation, and the stresses developed inside the electrode. To avoid the local exhaustion of Li ions in the electrolyte due to fast consumption at the surface of electrode, it is assumed that the rate of transport of Li atoms in the electrolyte is much larger than the rate of its consumption. Also, the Si atoms are assumed to form an immobile frame and movement of Li atoms are considered in the model. The Li content is described by $c = \frac{\rho_{\text{Li}}}{\rho_{\text{Si}}}$, the ratio of molar densities of Li and Si. In the following, the equations governing the mechanical deformation, thermodynamics, and kinetics of Li diffusion inside the electrode, and the electrochemical reactions at the electrode/electrolyte interface are described.

4.2.1. Mechanical Deformation

A schematic of our one-dimensional diffusion problem and the coordinate system is given in figure 4.1. The thickness of the sample is H . The crystalline Si part ahead of the phase boundary is shown in solid orange and the lithiated Li_xSi part behind the phase boundary is shown with dotted orange pattern. Insertion of Li is happening at $x=0$. The Si electrode is modeled as an isotropic elastic-plastic solid with a concentration dependent biaxial modulus B and yield stress σ_0 . Expansion of the electrode in the x direction causes material points initially located at x to move to a new position X with a displacement $u = X - x$. The corresponding deformation can be described by a logarithmic true strain

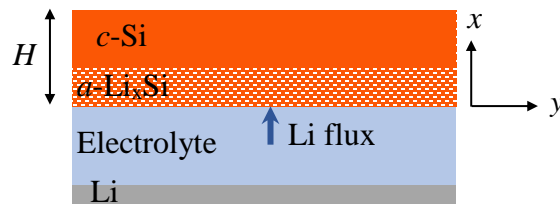


Figure 4.1. Schematic representing the one-dimensional model of the Li-Si system. The total thickness of the sample is H . The crystalline Si electrode is partially lithiated. The $c\text{-Si}$ part ahead of the phase boundary is shown in solid orange and the lithiated Li_xSi part behind the phase boundary is shown with dotted orange pattern.

$$\varepsilon_{xx} = \log\left(1 + \frac{\partial u}{\partial x}\right), \varepsilon_{yy} = \varepsilon_{zz} = 0 \quad (4.1)$$

This deformation is assumed to occur due to three underlying mechanisms; 1) The infinitesimal elastic distortion of the Si lattice ($\varepsilon_{xx}^e, \varepsilon_{yy}^e = \varepsilon_{zz}^e$) which leads to stresses. 2) The isotropic volume expansion of Si when a molar concentration, c , of Li is inserted and alloyed, $\frac{dV}{dV_0} = 1 + \beta(c)c$, which gives a true strain of $\frac{1}{3}\log(1 + \beta c)$. $\beta(c)$ is the volume expansion ratio of the stress-free state due to the insertion of Li. Its argument is being dropped for the sake of simplicity. 3) The irreversible, volume preserving plastic deformation, ε^p , characterized by the plastic stretch ratio λ^p . The strains must satisfy the compatibility conditions

$$\varepsilon_{xx}^e + \frac{1}{3}\log(1 + \beta c) - 2\log(\lambda^p) = \log\left(1 + \frac{\partial u}{\partial x}\right) \quad (4.2)$$

$$\varepsilon_{yy}^e + \frac{1}{3}\log(1 + \beta c) + \log(\lambda^p) = \varepsilon_{zz}^e + \frac{1}{3}\log(1 + \beta c) + \log(\lambda^p) = 0 \quad (4.3)$$

The lithiated Si goes through an equi-biaxial state of stress described by the Kirchhoff stress $\sigma_{yy} = \sigma_{zz} = \sigma$ with the elastic constitutive equation

$$\sigma = B(c)\varepsilon_{yy}^e = B(c)\left[-\frac{1}{3}\ln(1 + \beta c) - \ln(\lambda^p)\right] \quad (4.4)$$

The biaxial modulus, $B(c)$, of the lithiated Si is assumed to have a logarithmic dependence on the concentration $B(c) = B_0 + B_1\ln(1 + B_2c)$. B_0 is the biaxial modulus of pristine Si and B_1 and

B_2 are constants (See Table 4.1). These constants are obtained by fitting the above expression to the results from a computational analysis of the elastic constants of $a\text{-Li}_x\text{Si}$ by Shenoy et al.⁷⁶. The constitutive law governing the viscoplastic deformation of the lithiated Si is assumed to be

$$\dot{\epsilon}^p = \frac{d}{dt} \ln(\lambda^p) = \begin{cases} 0 & , |\sigma| < \sigma_0 \\ \frac{\dot{\epsilon}_0}{2} \left(\frac{|\sigma|}{\sigma_0} - 1 \right)^m \frac{\sigma}{|\sigma|} & , |\sigma| \geq \sigma_0 \end{cases} \quad (4.5)$$

with characteristic strain rate $\dot{\epsilon}_0$ and stress exponent m (greater than 1). The concentration-dependent yield stress is defined as $\sigma_0 = s_0 + s_1 \ln(1 + s_2 c)$, where s_0 is the yield stress of $c\text{-Si}$ ⁷⁸ and s_1 and s_2 are constants (See Table 4.1). These constants are obtained by fitting the above expression to the values reported by Fan et al.⁵⁸ for the yield stress of lithiated Si at various states of charge. They used molecular dynamic simulations with reactive force field to characterize the mechanical properties of amorphous Li_xSi alloys.

Table 4.1. parameters used in defining the evolution of the biaxial modulus and the yield stress of silicon during lithiation

parameter	value
B_0 (GPa)	180.7
B_1 (GPa)	-33.39
B_2	18.4
s_0 (GPa)	6.36
s_1 (GPa)	-5.6
s_2	0.46

4.2.2. Thermodynamics and kinetics of Li transport- a phase field approach

Thermodynamic driving forces such as the change in the chemical potential, the interfacial energy, and the elastic energy can prompt spontaneous phase transformation to accommodate drastic evolution in the free energy. Kinetic mechanisms such as diffusion can also contribute to the characteristics of the phase transformation. The state variable used here is the concentration, which is a conserved quantity, i.e. its total amount is constant in the specified volume. Therefore, a Cahn-Hilliard phase field method is applicable for the study of diffusion. A brief introduction to the derivation of the Cahn-Hilliard formulation is given in the appendix.

Hulikal et al.⁵² have adapted a Cahn-Hilliard description of the evolution of the spinodal decomposition to define the changes in the chemical potential (μ) during diffusion of Li in tin electrodes:

$$\mu = \frac{d\psi_0}{dc} - \kappa \frac{d^2c}{dx^2}, j = -M \frac{\partial \mu}{\partial x} \quad (4.6)$$

Where κ is the gradient energy coefficient that determines the interface energy, sharpness of the interface, and the thickness of a diffuse interface. If $\kappa = 0$, Fick's law for interstitial diffusion can be recovered. M is the mobility of Li ions in the lithiated layer. In the modified Cahn-Hilliard theory used here, the mobility is a function of the concentration gradient. The first term in the chemical potential represents the energy of mixing and the second term represents the interfacial energy. The free energy function for the Li-Si system with two separable phases can be described by a homogeneous double-well thermodynamic potential with a derivative of the form

$$\frac{d\psi_0}{dc}(c) = \frac{\Gamma}{(c_1 - c_0)^2} (c - c_0)(c - c_1)(\omega c - c_0 - c_1) + \mu^{eq} \quad (4.7)$$

With c_0 and c_1 the equilibrium concentrations of the two phases, Γ determining the curvature at the equilibrium concentrations, ω a constant that determines the location of the spinodal, and μ^{eq} the equilibrium chemical potential.

Bower et al.⁹³ provided the contribution of the stress terms to the chemical potential through the addition of $-\frac{\sigma^2}{\rho} \frac{\partial}{\partial c} \left(\frac{1}{B} \right) - \frac{2\sigma}{3\rho} \frac{\partial \varepsilon_V^c}{\partial c}$ terms to the chemical potential with ρ representing the molar density of Si and ε_V^c the volumetric strain due to lithium insertion, $\varepsilon_V^c = \varepsilon_{xx}^c + \varepsilon_{yy}^c + \varepsilon_{zz}^c = \ln[1 + \beta c]$ and $\frac{\partial \varepsilon_V^c}{\partial c} = \frac{\beta + \frac{d\beta}{dc}c}{1 + \beta c}$. Ignoring the derivatives of the volume expansion ratio and assuming an average value¹⁵ of $\beta = 0.7$, the final form of the chemical potential is

$$\mu = \frac{d\psi_0}{dc} - \kappa \frac{d^2c}{dx^2} - \frac{\sigma^2}{\rho} \frac{\partial}{\partial c} \left(\frac{1}{B} \right) - \frac{2\sigma}{3\rho} \frac{\beta}{1 + \beta c} \quad (4.8)$$

The classical Cahn-Hilliard equation has ignored the non-equilibrium behavior of the interface which is important in small scale electrodes. According to this classical description, interface has infinite mobility and phase transformation is controlled by the diffusion of the species in the bulk material. In order to incorporate the driving forces for the bulk diffusion and the local processes at the interface, Langer and Sekerka¹²⁸ solved the diffusion problem at two length scales; the thickness of the interface and the length of bulk diffusion. And, defined a phenomenological

mobility function with a concentration-gradient dependence. The time dependence of the concentration is related to the gradient in the chemical potential through the mobility function $M =$

$$\frac{M_0}{1 + \frac{\chi}{\Delta c_0} \left| \frac{\partial c}{\partial x} \right|}$$

$$\frac{\partial c}{\partial t} = \frac{\partial}{\partial x} M \frac{\partial \mu}{\partial x} \quad (4.9)$$

where M_0 is the Li mobility in the bulk phase when the concentration gradients are small and χ determines the mobility of the a -Li _{χ} Si/ c -Si interface. The resistivity to the motion is localized to, while varying smoothly throughout the interface region. The resulting chemical potential profile is determined by the mobility M . There appears to be no obvious way in the classical Cahn-Hilliard formulation to control the phase boundary mobility independent of the mobility of the transporting species, although the phase boundary mobility may depend on the shape of the free energy function and the value of κ . If the mobility is concentration dependent, it would be possible to block or slow down the transport of species into the phase boundary. It would also influence the transport across the phase boundary.

4.2.3. A general sharp interface model⁵²

Studying the sharp interface limit allows careful calibration of the behavior at the interface and the model parameters. To do so, an energetic formulation of the problem is considered to identify the kinetic variables and their conjugate forces for diffusion in the bulk and at the interface. It is

followed by a perturbation analysis of the governing equations of the Cahn-Hilliard model. Combination of the two approaches provides Cahn-Hilliard's kinetic relations at the interface.

4.2.3.1. Energetic formulation

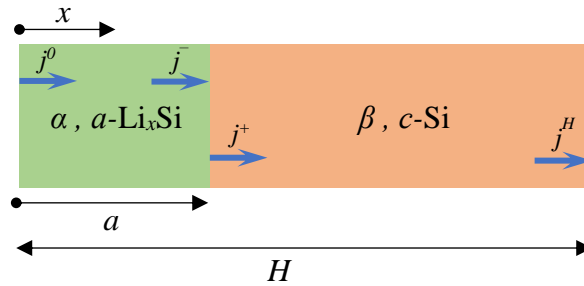


Figure 4.2. Schematic representing the one-dimensional two-phase model for the diffusion of Li in partially lithiated crystalline Si. The amorphous and the crystalline phases are named the α and β , the phase boundary is at a distance “a” from the free surface and the thickness of the sample is H . The flux at the surface, behind and ahead of the interface and at $x=H$ are marked with j^0 , j^- , j^+ , and j^H , respectively.

A schematic of the sharp interface problem is shown in figure 4.2. The figure illustrates a partially lithiated Si of thickness H and area A with a phase boundary at $x = a$. The regions behind and ahead of the phase boundary are colored in green and orange, respectively. The free energy of the partially lithiated crystalline Si is

$$U = A \left[\int_0^a \psi_\alpha(c(x)) dx + \int_a^H \psi_\beta(c(x)) dx + U^H + U^0 \right] \quad (4.10)$$

U^0 and U^H are the energies associated with the surfaces of the sample at $x=0$ and $x=H$, that do not change with time. α and β represent the a -Li_xSi and c -Si phases, respectively, with free energy densities of ψ_α and ψ_β . Taking the time derivative of the total free energy

$$\frac{dU}{dt} = \dot{U} = A \left[\int_0^a \frac{d\psi_\alpha}{dc} \frac{\partial c}{\partial t} dx + \int_a^H \frac{d\psi_\beta}{dc} \frac{\partial c}{\partial t} dx + \left(\psi_\alpha(c^-) - \psi_\beta(c^+) \right) \frac{da}{dt} \right] \quad (4.11)$$

We have $\mu = \frac{d\psi}{dc} - f(\sigma, c)$, $f(\sigma, c) = \frac{\sigma^2}{\rho} \frac{\partial}{\partial c} \left(\frac{1}{B} \right) + \frac{2\sigma\beta}{3(1+\beta c)\rho}$, and $\frac{\partial c}{\partial t} = -\frac{\partial j}{\partial x}$. Integration by parts

gives

$$\dot{U} = A \left[-\int_0^a \mu \frac{\partial j}{\partial x} dx - \int_a^H \mu \frac{\partial j}{\partial x} dx - \int_0^a f(\sigma, c) \frac{\partial j}{\partial x} dx - \int_a^H f(\sigma, c) \frac{\partial j}{\partial x} dx + \left(\psi_\alpha(c^-) - \psi_\beta(c^+) \right) \frac{da}{dt} \right] \quad (4.12)$$

$$\dot{U} = A \left[\int_0^H j \frac{\partial \mu}{\partial x} dx + \mu^+ j^+ - \mu^- j^- + \mu^0 j^0 - \mu^H j^H - \int_0^a f(\sigma, c) \frac{\partial j}{\partial x} dx - \int_a^H f(\sigma, c) \frac{\partial j}{\partial x} dx + \left(\psi_\alpha(c^-) - \psi_\beta(c^+) \right) \frac{da}{dt} \right] \quad (4.13)$$

The superscripts 0, H , +, $-$ represents the quantities at the boundaries and just ahead and before the interface. So, the changes in the energy in the bulk (\dot{U}_{bulk}) and at the interface (\dot{U}_{int}) are given by

$$\begin{aligned} \dot{U}_{bulk} = & A \int_0^H j \frac{\partial \mu}{\partial x} dx - A \left[\int_0^a f(\sigma, c) \frac{\partial j}{\partial x} dx + \int_a^H f(\sigma, c) \frac{\partial j}{\partial x} dx \right] = -A \int_0^H \frac{j^2}{M_0} dx - \\ & A \left[\int_0^a f(\sigma, c) \frac{\partial j}{\partial x} dx + \int_a^H f(\sigma, c) \frac{\partial j}{\partial x} dx \right] \end{aligned} \quad (4.14)$$

$$\dot{U}_{int} = A \left[\mu^+ j^+ - \mu^- j^- + \left(\psi_\alpha(c^-) - \psi_\beta(c^+) \right) \frac{da}{dt} \right] \quad (4.15)$$

Using $\mu^+ j^+ - \mu^- j^- = \frac{\mu^+ + \mu^-}{2} (j^+ - j^-) + (\mu^+ - \mu^-) \frac{j^+ + j^-}{2}$ and mass conservation $\frac{da}{dt} (c^+ - c^-) = j^+ - j^-$, Eq. 4.15 can be written as

$$\dot{U}_{int} = A \left[(\mu^+ - \mu^-) \frac{j^+ + j^-}{2} + (j^+ - j^-) \left(\frac{\mu^+ + \mu^-}{2} - \frac{\psi_\beta(c^+) - \psi_\alpha(c^-)}{c^+ - c^-} \right) \right] \quad (4.16)$$

The above equation identifies the driving force conjugates for the average flux and the jump in the flux (proportional to the interface velocity). At equilibrium, the driving force is zero and the chemical potential at the interface is equal to $\frac{d\psi}{dc} (c^{eq})$. The common tangent rule gives

$$\mu^{eq+} = \mu^{eq-} = \frac{d\psi_\alpha}{dc} (c^{eq-}) = \frac{d\psi_\beta}{dc} (c^{eq+}) = \frac{\psi_\beta(c^{eq+}) - \psi_\alpha(c^{eq-})}{c^{eq+} - c^{eq-}} \quad (4.17)$$

From Eq. 4.16 and assuming linear interface kinetics, we can define the driving force conjugates for the average flux and interface velocity as:

$$j^+ + j^- = -K_1(\mu^+ - \mu^-) \text{ and } j^+ - j^- = -2K_2\left(\frac{\mu^+ + \mu^-}{2} - \frac{\psi_\beta(c^+) - \psi_\alpha(c^-)}{c^+ - c^-}\right) \quad (4.18)$$

If we consider a small perturbation from equilibrium, the change in the free energy is negligible, while $\mu^+ = \mu^{eq+} + \delta\mu^+$ and $\mu^- = \mu^{eq-} + \delta\mu^-$, therefore

$$j^+ + j^- = -K_1(\delta\mu^+ - \delta\mu^-) \text{ and } j^+ - j^- = -K_2(\delta\mu^+ + \delta\mu^-) \quad (4.19)$$

Finally, the interface dissipation for small deviations from the equilibrium is

$$\dot{U}_{int} = -A \left[K_1 \frac{(\delta\mu^+ - \delta\mu^-)^2}{2} + K_2 \frac{(\delta\mu^+ + \delta\mu^-)^2}{2} \right] = -A \left[\frac{(j^+ + j^-)^2}{2K_1} + \frac{(j^+ - j^-)^2}{2K_2} \right] \quad (4.20)$$

4.2.3.2. *Perturbation analysis of the Cahn-Hilliard equations*

We found the driving force conjugates for the average flux and the jump in the flux at the interface for a general sharp interface model. In this section, we use a perturbation analysis on the governing equations of our Cahn-Hilliard model to find the relation between the kinetics of the phase boundary interpreted by the two models. Langer and Sekerka¹²⁸ developed a model for small departure from the local equilibrium at a moving interface. They introduced the boundary

conditions for the governing equations (Eq. 4.6) at the interface based on the jumps in the concentration and flux and the interface velocity v

$$\delta c^- = -\frac{v[c^{eq}]\vartheta \xi}{3D} + \frac{\vartheta \xi}{D}(j^+ + j^-) \quad (4.21)$$

$$\delta c^+ = -\frac{v[c^{eq}]\vartheta \xi}{3D} - \frac{\vartheta \xi}{D}(j^+ + j^-) \quad (4.22)$$

where δc is the deviation from the equilibrium concentration, $[c^{eq}]$ is the jump in the equilibrium concentration at the interface, ϑ is a parameter accounting for extra resistivity and is proportional to the gradient of c , ξ is the thickness of the interface, and $D = M\Gamma$ is the diffusivity with $\Gamma = \frac{d^2\psi_0(c)}{dc^2}$.

For small perturbations, $\delta c = \delta\mu/\Gamma$ and mass conservation gives $[c^{eq}] = [j]/v$. Substituting these relations for δc and $[c^{eq}]$ in equations 4.21 and 4.22 and rearranging gives

$$\delta\mu^- = -\frac{(j^+ - j^-)\vartheta\xi}{3M} + \frac{\vartheta\xi}{M}(j^+ + j^-) = \frac{2}{3}\frac{\vartheta\xi}{M}j^+ + \frac{4}{3}\frac{\vartheta\xi}{M}j^- \quad (4.23)$$

$$\delta\mu^+ = -\frac{(j^+ - j^-)\vartheta\xi}{3M} - \frac{\vartheta\xi}{M}(j^+ + j^-) = -\frac{4}{3}\frac{\vartheta\xi}{M}j^+ - \frac{2}{3}\frac{\vartheta\xi}{M}j^- \quad (4.24)$$

Defining the parameter $\chi = \frac{\vartheta\xi}{4}$, equations 4.23 and 4.24 are simplified as

$$\delta\mu^- = \frac{\chi}{6M}j^+ + \frac{\chi}{3M}j^- \quad (4.25)$$

$$\delta\mu^+ = -\frac{\chi}{3M}j^+ - \frac{\chi}{6M}j^- \quad (4.26)$$

Now, the interface kinetics from the sharp interface model (Eq. 4.19) can be compared with those from the Cahn-Hilliard model (Eq. 4.25 and 4.26). A zero-valued χ reduced the mobility function to $M = M_0$ and recovers the classical Cahn-Hilliard governing formulation from Eq. 4.6. If $\chi = 0$ in the sharp interface model, the interface would be at local equilibrium ($\delta\mu^\pm = \delta c^\pm = 0$). To solve the phase transformation problem in the sharp interface model, the equations of diffusion in the bulk must be solved with the boundary conditions introduced by equations 4.25 and 4.26. The parameter χ represents the interface mobility and a non-zero χ gives non-zero values for the deviations of the concentration and the chemical potential at the interface from equilibrium.

Combining equations 4.19, 4.25 and 4.26, gives $K_1 = \frac{2M_0}{\chi}$ and $K_2 = \frac{6M_0}{\chi}$. This indicates that the Cahn-Hilliard formulation is a special case of the general kinetics law with $K_2 = 3K_1$. Moreover, in the classical interpretation of the Cahn-Hilliard equations with infinite interface mobility ($\chi \rightarrow 0, K_1, K_2 \rightarrow \infty$), the energy dissipation at the interface (Eq. 4.20) is ignored.

4.2.4. Electrochemistry at the electrode/ electrolyte interface

The rate of the reaction at the electrode/electrolyte interface depends on the treatment of the electrode surface, composition of the electrolyte and the electrode potential. The latter is

characterized by the surface overpotential η defined as the potential of the working electrode relative to a reference electrode placed in the same solution or the difference between potential of the electrode (V) (relative to the solution) and its value at equilibrium¹³⁰. The equilibrium potential (U_0) depends on the chemical potential of Li at the surface of the electrode through

$$U_0 = -\frac{1}{F}(\mu^\theta + \mu) \quad (4.27)$$

where $U^\theta = \frac{\mu^\theta}{F}$ is the standard or the open-circuit potential. The relation between the current density which characterizes the reaction rate at the surface, overpotential, and the concentration close to the surface of the electrode is given by the Butler-Volmer equation

$$i = i_0 \left[\exp\left(\frac{\alpha_a F \eta}{RT}\right) - \exp\left(-\frac{\alpha_c F \eta}{RT}\right) \right] \quad (4.28)$$

This equation relates the net reaction rate to the sum of the anodic and cathodic reactions with charge transfer coefficients α_a and α_c , respectively and exponential dependence on η . Following the common practice, we take $\alpha_c = 1 - \alpha_a = 0.5$. The exchange current density i_0 depends on the composition of the electrolyte near the electrode, Li concentration at the surface of the electrode, temperature, and the surface properties of the electrode. F is the Faraday constant, R is the universal gas constant, and T is the temperature. The current density at the surface of the electrode is related to the flux through $i = -\rho F j$.

The boundary conditions used for solving the moving phase boundary problem (Fig. 4.1) are

- At $x=H$, we assumed a zero-flux condition: $\frac{\partial c}{\partial x} = 0$ and $\frac{\partial \mu}{\partial x} = 0$.
- At the electrode/electrolyte interface ($x = 0$), we have: $\frac{\partial c}{\partial x} = 0$ and $\frac{\partial \mu}{\partial x} = -\frac{J}{M}$, where the flux J is related to the externally applied current through $J = -\frac{i}{\rho F}$.

The finite element implementation of the model is described in section 4.4.2.

4.2.4.1. Steady state diffusion

We can use the results from the perturbation analysis of our modified Cahn-Hilliard equation in section 4.2.3.2 to determine the model parameters. If the bulk diffusion is at steady state due to small lithiation rate, the chemical potential will have a linear profile in the bulk material of each phase with $j^- = j$ and $j^+ = 0$. We can write the governing equation 4.6 as

$$j^- = -M_0 \frac{\mu^- - \mu^0}{x_{int}}, \quad j^+ = -M_0 \frac{\mu^H - \mu^+}{H - x_{int}} \quad (4.29)$$

where x_{int} is the position of the interface. Using $\mu^- = \mu^{eq} + \delta\mu^-$ and Eq. 4.25,

$$\frac{1}{M_0} (x_{int} + \frac{\chi}{3}) j = \mu^0 - \mu^{eq} \quad (4.30)$$

We can Linearize the Butler-Volmer equation (4.28) for small currents,

$$i = i_0 \frac{\eta F}{RT} = i_0 \frac{VF + \mu^\theta + \mu^0}{RT} \quad (4.31)$$

substituting the relation between the flux and the externally applied current density ($i = -\rho j F$) in Eq. 4.30 and combining it with equation 4.31, we have

$$V = -\frac{\mu^\theta + \mu^{eq}}{F} + \frac{i}{F} \left[\frac{x_{int}}{FM_0\rho} + \frac{\chi}{3FM_0\rho} + \frac{RT}{i_0} \right] \quad (4.32)$$

According to Eq. 4.32, during constant current experiments, the voltage (V) varies linearly with the position of the interface (x_{int}) and the slope of the curve is related to the mobility (M_0) of Li. Additionally, the exchange current density (i_0) and the interface-mobility parameter (χ) can be determined from the relation between the applied current (i) and the voltage (V) during constant current experiments (refer to the next section for further details).

4.3. Model Behavior

The next task is to extract the values of the unknown parameters including the free energy parameters, exchange current density, phase boundary mobility, and mobility of Li in Li_xSi . We calibrate the unknown parameters in our modified Cahn-Hilliard model by fitting the model output

to our experimental results. The concentration-gradient dependence of the mobility in our model enables us to explore a wide range of phase propagating cases from the interface limited (with $\chi \rightarrow \infty$) where the phase boundary is immobile, to the diffusion limited case (with $\chi \rightarrow 0$) where the phase boundary has infinite mobility. The standard Cahn-Hilliard formulation is limited to the problems with infinite phase boundary mobility.

The experiments are done on Si wafers with {100} and {110} orientations. The samples are lithiated according to the following procedure:

- i. A constant current is applied to bring the potential down to 120 (140[§]) mV.
- ii. A total charge of 5400 C/m² is passed to the Si electrode by applying constant current density of 30, 20, or 10 $\mu\text{A}/\text{cm}^2$ to nucleate and grow the amorphous Li_xSi layer.

During this step, Li diffuses into Si until its concentration at the surface reaches the lower spinodal where the nucleation happens, and the phase boundary starts propagating inside the bulk Si leaving an amorphous phase behind it.

- iii. The cell is held at open circuit for 5 hours.
- iv. The voltage is held at 100 (120) mV for 5 hours.
- v. The cell is relaxed during another five-hour open circuit step.
- vi. The second potentiostatic step applies a voltage of 80 (100) mV at the surface of Si for 5 hours.
- vii. Open circuit measurement is done for 5 hours.

In the classical Cahn-Hilliard formulation, with constant mobility, the chemical potential is at its equilibrium value across the phase boundary during potentiostatic lithiation; however, the

[§] The numbers given in the parenthesis are the values used in the experiments done on the {110} oriented Si wafers

finite interface mobility imposed by the modified Cahn-Hilliard equations, results in a jump in the chemical potential at the interface. The magnitude of this jump decreases as the current decreases during the potentiostatic hold (Refer to Fig. 4.10).

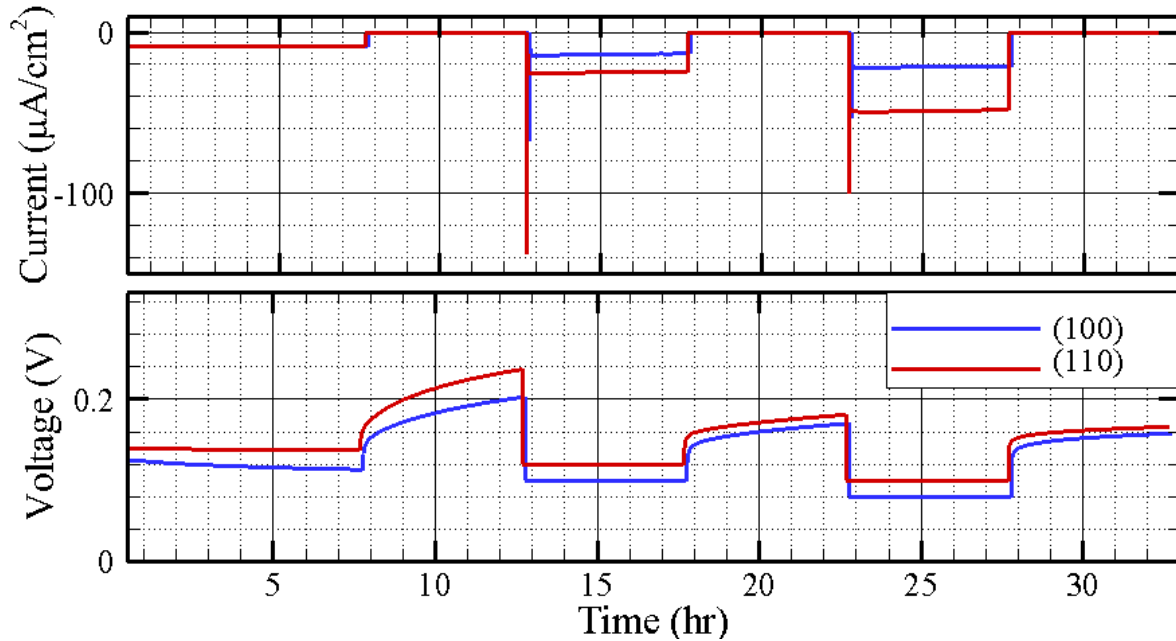


Figure 4.3. Current and voltage evolution during galvanostatic, potentiostatic, and open-circuit experiments used to calibrate and determine the Cahn-Hilliard model parameters.

Lithiation Recipe for {100} orientation:	Lithiation Recipe for {110} orientation:
<ul style="list-style-type: none"> • Lithiate at $25 \mu\text{A}/\text{cm}^2$ till voltage $<0.12\text{V}$ • Lithiate at $30/20/10 \mu\text{A}/\text{cm}^2$ for 5 /7.5/15 hrs (consumes~100nm <i>c</i>-Si) • OCP for 5 hrs • Potentiostatic hold at 0.1V • OCP for 5 hrs • Potentiostatic hold at 0.08V • OCP for 5 hrs 	<ul style="list-style-type: none"> • Lithiate at $25 \mu\text{A}/\text{cm}^2$ till voltage $<0.14\text{V}$ • Lithiate at $30/20/10 \mu\text{A}/\text{cm}^2$ for 5/7.5/15 hrs (consumes~120nm <i>c</i>-Si) • OCP for 5 hrs • Potentiostatic hold at 0.12V • OCP for 5 hrs • Potentiostatic hold at 0.1V • OCP for 5 hrs

The variations of voltage and current with time for two sets of experiments done on the {100} and {110} oriented wafers with galvanostatic lithiations at $20 \mu\text{A}/\text{cm}^2$ are shown in Fig. 4.3. These experimental measurements are used as the basis for fitting the model predictions in order to extract the kinetic parameters controlling the phase transformation in Si during lithiation.

We now turn our attention to finding the unknown parameters:

4.3.1. Free Energy

The equilibrium chemical potential can be determined from Eq. 4.27,

$$\frac{d\psi_0}{dc} = \mu^{eq} = -F(U^\theta + V) \quad (4.33)$$

where U^θ is the open circuit potential and V is the plateau potential with respect to Li/Li^+ during phase propagation. The free energy potential must satisfy the following conditions:

The energy has minima ($\frac{d\psi_0}{dc} = 0$) at $c = 0$ and $c = 3.75$ which correspond to the stoichiometric phases of pure c -Si and $\text{Li}_{3.75}\text{Si}$. The curvature of the free energy function at these concentrations must be positive. The concentrations at the spinodal point where the nucleation happens is reported to be about $0.1^{55, 129}$ for the Li-Si system. We have defined the parameter ω in the definition of the derivative of the free energy density (Eq. 4.7) to control the position of the spinodal point. Based on the abovementioned criteria, the maximum possible value for ω is about 3, which positions the

lower spinodal ($\frac{d^2\psi_0}{dc^2} = 0$) at a concentration of $c = 0.8$. Additionally, the equilibrium concentration values are calculated to be $c_0 = 0.287$ and $c_1 = 3.948$. The parameters related to these fittings are summarized in Table 4.2. After calibrating the free energy parameters base on experimental results, the free energy and its derivative (described by Eq 4.7) demonstrate the profiles shown in Figure 4.2.

Table 4.2. phase field model parameters calibrated based on experimental results

Parameter	{100}	{110}
U^θ (V)	3.25	3.27
V (V)	0.1	0.12
ω	3	3
c_0	0.287	0.287
c_1	3.948	3.948
μ^{eq} (MJ/mol)	0.304	0.305
Γ (MJ/mol)	0.846	0.848
$i_{0,min}$ ($\mu A/cm^2$)	39	110
χ_{max} (μm)	1.27	2.15
i_0 ($\mu A/cm^2$)	700	2815
χ (μm)	1.20	2.06
V_{ref} (V)	0.416	0.419
κ ($\mu m^2 mol/J$)	22.86	22.90

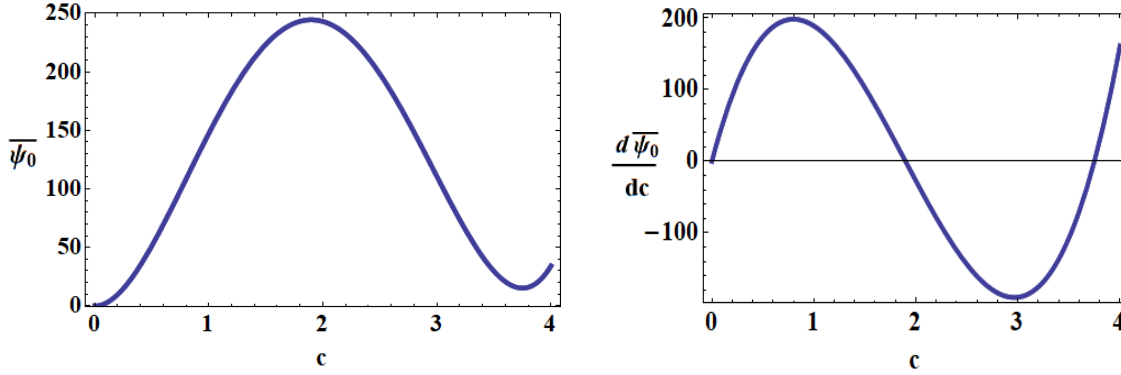


Figure 4.4. (a) Normalized homogeneous free energy and (b) its derivative based on calibrations for the free energy function. The energy minima are at $c = 0$ and 3.75 and the lower spinodal point is at $c = 0.8$.

4.3.2. Lithium mobility in the lithiated layer

To determine the lithium mobility M_0 in the lithiated layer, we use the results from the galvanostatic lithiation experiment. From Eq. 4.32, the slope of the voltage vs the position of the interface is

$$\frac{dV}{dx_{int}} = \frac{i}{M_0 \rho F^2} \quad (4.34)$$

The position of the interface is calculated from the velocity of the phase boundary at the applied current density (Table 3.1) and a volume expansion ratio of 3.75. The slope of the linear fit gives a value of $M_0 = 8.8 \times 10^{-21}, 4.2 \times 10^{-20} \frac{m^2.mol}{J.s}$ normal to the $\{100\}$ and $\{110\}$ orientations (Fig. 4.3). Ding et al.¹³¹ used galvanostatic intermittent titration technique on composite electrodes containing nano-Si particles to study the diffusivity of Li in Li_xSi during. By fitting the results of experimental measurement to the model developed by Weppner and Huggins¹³², they estimated

the diffusion coefficient to be about $10^{-16} \frac{m^2}{s}$. Using the relation between the diffusivity and mobility in the bulk $D = M_0RT$, mobility of Li in lithiated nano-Si would be $4 \times 10^{-20} \frac{m^2.mol}{J.s}$. Pell (1960)¹³³ determined the diffusion coefficient of Li in Si at room temperature to be about $2 \times 10^{-18} \frac{m^2}{s}$ which gives the mobility in the bulk of *c*-Si of about $8.1 \times 10^{-22} \frac{m^2.mol}{J.s}$. These reports suggest that the mobility of Li atoms in crystalline Si is smaller than the corresponding value in *a*-Li_xSi. To reduce the mobility of Li atoms before and during nucleation (from the values in *a*-Li_xSi to those corresponding to *c*-Si), we have introduced a correcting factor to the mobility function:

$$M = \frac{M_0}{1 + \frac{\chi}{\Delta c_0} \left| \frac{\partial c}{\partial x} \right|} \left(\frac{\tan^{-1}[10(c-1.1)]}{3.39} - \tan^{-1}[-0.61] \right) \quad (4.35)$$

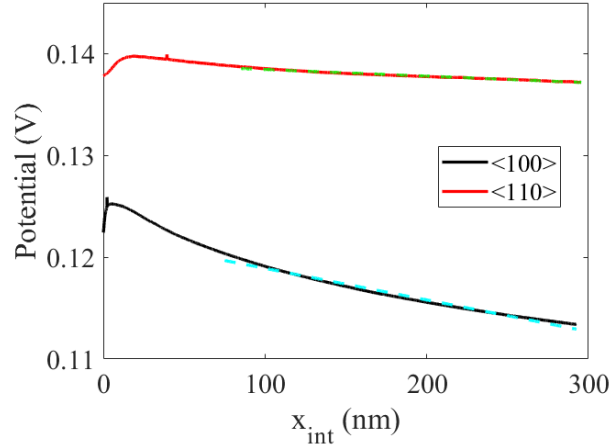


Figure 4.5. Linear fit to the evolution of the potential with interface position during constant current experiments at $20 \mu A/cm^2$ on the (100) and (110) oriented Si wafers.

The slope of potential with current density in Eq. 4.32 gives a relation between the exchange current density (i_0) and the interface-mobility parameter (χ).

$$\frac{dV}{di} = \frac{1}{F} \left[\frac{x_{int}}{FM_0\rho} + \frac{\chi}{3FM_0\rho} + \frac{RT}{i_0} \right] \quad (4.36)$$

So, we can determine the expected range for these parameters by considering the limiting cases of diffusion-controlled ($\chi \rightarrow 0$) and interface-reaction-controlled ($i_0 \rightarrow \infty$) phase transformation behaviors. Galvanostatic lithiation of Si at different current densities shows that the average value of the potential at every specified state of charge varies linearly with the current density. The plots of voltage with charge density for the {100} oriented Si are given in Figure 4.6a. Using these average voltage values and Eq. 4.32, we can derive the relation between the voltage and current density as shown in Figure 4.6b. The calculated values for $i_{0,min}$ and $\chi_{,max}$ are given in Table 4.2.

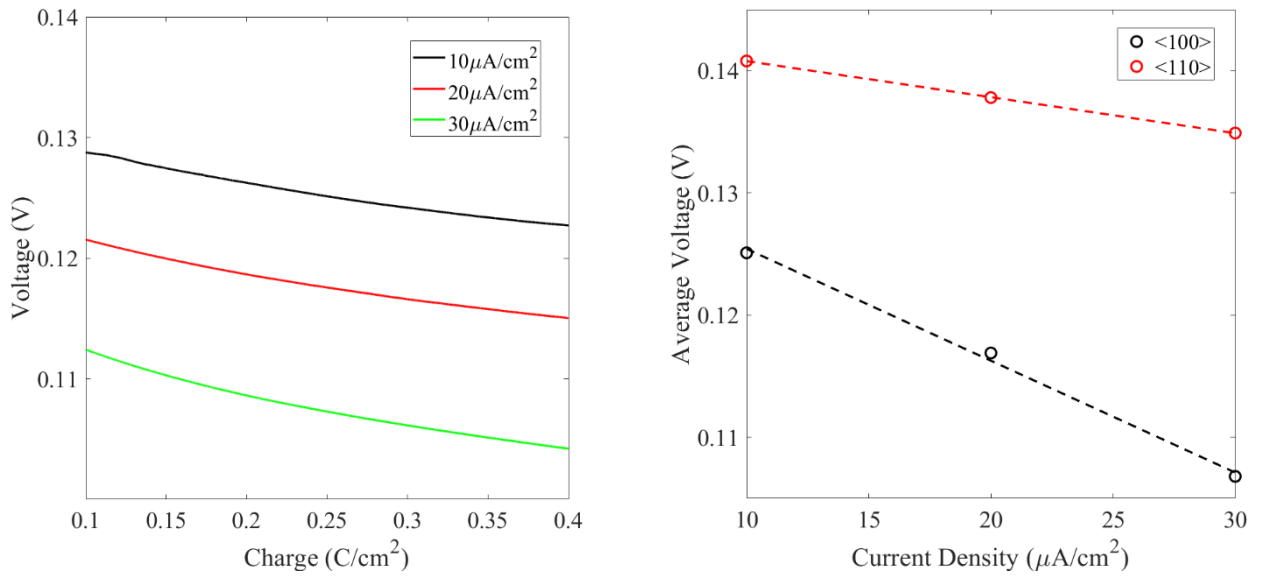


Figure 4.6. (a) Voltage evolution with state of charge during galvanostatic lithiation of (100) oriented Si at 10, 20, and 30 $\mu\text{A}/\text{cm}^2$. (b) relation between the average value of the voltage at a specified state of charge (as shown in (a)) and the current density during constant current experiments on the (100) and (110) oriented Si.

4.3.3. Exchange current density, interface mobility and velocity of the phase boundary

To calibrate the kinetic parameters i_0 , χ , and V_{ref} , we compare the results from experiments and simulations during the galvanostatic and the first potentiostatic lithiation steps. V_{ref} decides the magnitude of the voltage plateau during the galvanostatic step. The evolution of current during the potentiostatic step is controlled by i_0 and χ ; The exchange current density (i_0) determines the transient behavior at the beginning and the interface mobility parameter (χ) determines the behavior at later times. The fitted parameters are given in Table 4.2. In these simulations, we have assumed a phase boundary with a thickness of $h = 3$ nm (See section 4.3.5.1 For details). This assumption determines the value of κ in Eq. 4.8 for the chemical potential through the relation introduced by Langer and Sekerka¹²⁸

$$\left. \frac{d^2\psi_0}{dc^2} \right|_{c=c_0} + \left. \frac{d^2\psi_0}{dc^2} \right|_{c=c_1} = \frac{h^2}{\kappa} \quad (4.37)$$

The amount of charge loss to the side reaction must be included in our charge measurements. The reported values in the literature vary significantly according to the experimental conditions. Chan et al.²⁴ reported a first cycle capacity loss of 1153 mAh/g during lithiation of Si nanowires and Nadimpalli et al.⁹ reported a value of 1488 mAh/g for the lithiation of Si thin films. Considering a total capacity of 3759 mAh/g for Si, the abovementioned studies report a loss of 31% and 40%, respectively. Yoon et al.¹⁰⁹ considered the effect of the electrolyte composition on the formation

of SEI. They reported charge losses during lithiation of *a*-Si thin films to be about 451 and 673 mAh/g for electrolytes composed of 1.2 M LiPF₆ in EC^{**} and 1.2 M LiPF₆ in PC^{††}, respectively. In order to find the portion of the charge that is contributing to the phase transformation processes in our experimental setup, we calibrate the velocity of the phase boundary propagation from our simulations with the velocity measured experimentally using the PU technique during galvanostatic and potentiostatic lithiation of Si (Table 3.1). Velocity of the phase boundary propagation is derived from dividing the change in its location by the change in time. In our model, this velocity is directly proportional to the flux at the surface, therefore, we can estimate the portion of the applied current that is consumed in side reactions including SEI formation. We assume that the loss happens at a constant rate during the first cycle of lithiation. The calibration reveals that, on average, about 55% (58% and 53% for reactions normal to the {100} and {110} orientations, respectively) of the charge is consumed in side reactions.

The calculated values for the velocity of the phase boundary propagation using simulations after correcting for the Li loss and PU experiments are given in Table 4.3. Our model is able to predict the diversities in the kinetics of the phase boundary propagation through different crystallographic orientations of Si. The velocity of the phase boundary during galvanostatic lithiation show good agreement with those observed in experiments. The values change proportionally to the applied current density as expected from the mass conservation at the interface ($[c^{eq}] = [j]/v$). The velocity of the phase boundary propagation during the potentiostatic lithiation is mainly controlled by the interface mobility parameter. Larger χ allows the Li atoms to propagate with less resistance throughout the thickness of the interface. This larger mobility in the interfacial zone leads to higher

** ethylene carbonate

†† propylene carbonate

velocity of phase boundary in the $\langle 110 \rangle$ direction compared to the $\langle 100 \rangle$ direction. The influence of the interface mobility parameter has led to the nonuniform lithiation through different facets of Si nanopillars used in an experimental study by Lee et al.⁶⁰ (Refer to Fig. 1.3). The $\{110\}/\{100\}$ ratio of the simulated velocities at each potential is on average 40% larger than that observed in the experiment. The model's prediction for the velocity of the phase propagation during the first hour of potentiostatic lithiation is on average 27% and 47% smaller than the experimental measurement on phase propagation in the $\langle 100 \rangle$ and $\langle 110 \rangle$ directions, respectively. This could be due to the inefficiency of the model in predicting the evolution of the current at the beginning of the potentiostatic step.

Table 4.3. Comparison between the experimentally measured and computationally simulated values of the velocity of the phase boundary propagation normal to the $\{100\}$ and $\{110\}$ orientations during different galvanostatic and potentiostatic lithiation conditions. The velocities are reported in pm/s.

		{100}		{110}		{110}/{100} ratio	
		Experiment	Simulation	Experiment	Simulation	Experiment	Simulation
Galvanostatic	10 $\mu\text{A}/\text{cm}^2$	1.66	1.79	1.62	1.58	1.02	0.88
	20 $\mu\text{A}/\text{cm}^2$	2.94	3.58	3.34	3.15	1.13	0.88
	30 $\mu\text{A}/\text{cm}^2$	4.67	5.38	5.78	4.73	1.24	0.88
Potentiostatic	80 mV	35.6	15.83	106.1	60.01	2.98	3.79
	95 mV	25.7	10.47	79.4	46.34	3.09	4.42
	100 mV	5.8	8.66	19.1	41.71	3.29	4.81

Now that the portion of the current density that is used in the SEI growth is distinguished from the part that enters the electrode, other kinetic parameters of the model can be calibrated. Sethuraman et al.³⁶ reported an exchange current density of 10^{-10} mA/cm² for the reactions happening at the surface during cycling of Si thin films deposited with pulsed laser. Swamy and Chiang¹³⁴ used electrochemical impedance measurements and determined an exchange current density of 0.1 mA/cm² for surface reactions during lithiation of (100) and (111) oriented Si wafers. Calibrating the prediction of our model with experimental data on current evolution during potentiostatic lithiation of (100) and (110) wafers suggests values of 0.7 and 2.8 mA/cm², respectively for the exchange current densities at the surface of the Si electrodes. The variations of the current and voltage in Si samples with (100) and (110) orientations based on the predictions of our model and experimental measurements are plotted in figures 4.7 and 4.8, respectively. The model captures the essential electrochemical response of the system very well during galvanostatic and potentiostatic lithiation normal to the {100} and {110} crystallographic planes of Si. The largest discrepancy between experiments and simulations occurs in the open-circuit steps. The double layer capacitance drives the reactions inside the electrode plus the side reactions and leads to a relaxation process during these steps³⁶. This fact encourages further modifications in the model to identify the underlying mechanisms for the relaxation process in $a\text{-Li}_x\text{Si}$. Accordingly, the exchange current density introduced in the Butler-Volmer equations may be optimized for this specific system to capture the evolution of the portion of the applied current density that is consumed in the side reactions.

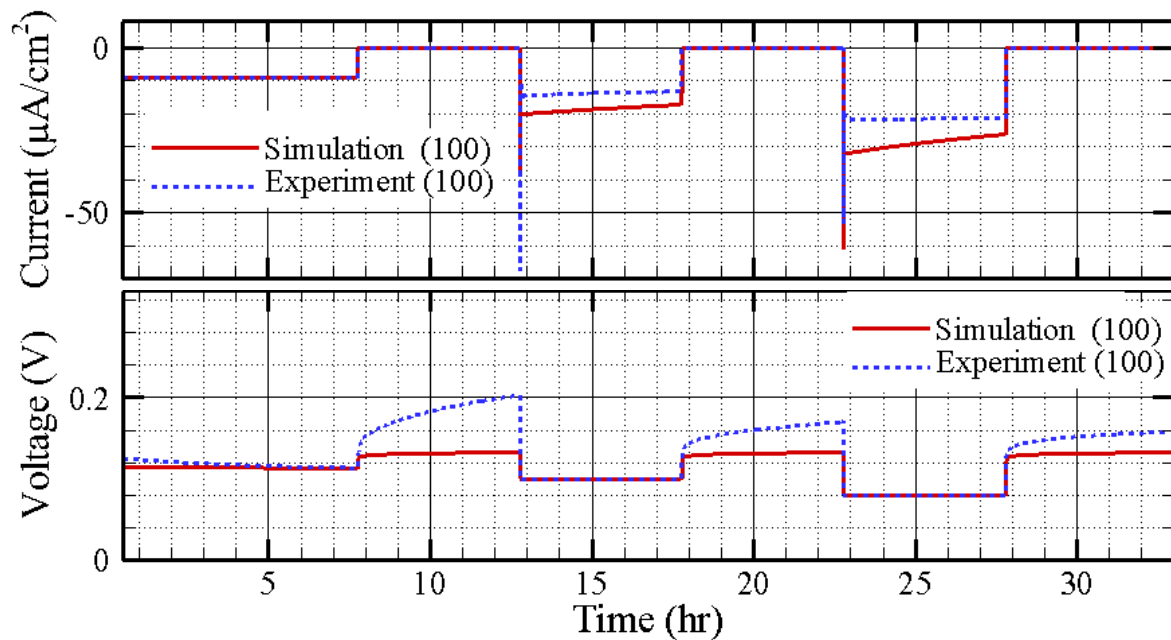


Figure 4.7. comparison between experimental measurements (dashed lines) and model predictions (solid lines) for the voltage and current density profiles during lithiation normal to (100) planes.

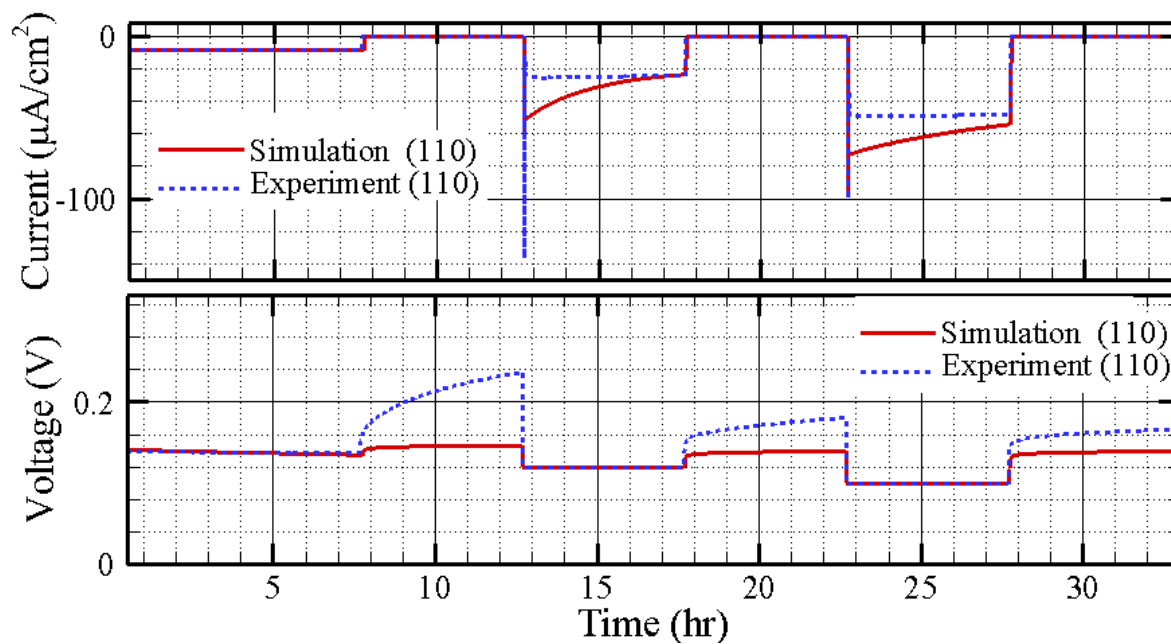


Figure 4.8. comparison between experimental measurements (dashed lines) and model predictions (solid lines) for the voltage and current density profiles during lithiation normal to (110) planes.

4.3.4. Chemical potential, concentration, stress and strain profiles

Now that the model parameters are calibrated, we can focus on the prediction of the model for the evolution in the chemical potential, concentration, stress, and plastic strain during galvanostatic and potentiostatic lithiation of crystalline Si with (100) and (110) orientations. In this section we investigate these quantities before/during nucleation in addition to their behavior at later stages of phase propagation.

The early stages of lithiation of the Si samples are shown in figure 4.9. The concentration in the electrode starts from $c=0$ and rises during the lithiation process. As the concentration of Li in crystalline Si reaches $c > 0.15$, the resulting compressive stresses exceed the elastic limit and permanent plastic deformation is observed near the free surface (shown with dark blue lines in Fig. 4.9). Chemical potential increases continuously as the derivative of the free energy increases. As soon as the free energy derivative reaches the lower spinodal, a distinct phase separation is observed in the chemical potential (Figs. 4.9a and 4.9c) and concentration profiles (marked with purple arrows in Fig. 4.9); the concentration behind the phase boundary jumps to the equilibrium concentration of Li in the lithiated phase (marked with the blue arrows in Fig. 4.9b and 4.9d) as determined by location of the minimum in the free energy. Ahead of the phase boundary the concentration goes down to the equilibrium concentration of Li in c -Si. The location of the phase boundary is marked with crosses on the chemical potential profiles in Figs. 4.9a and 4.9c. During nucleation ($c > c_{spinodal} = 0.8$) the biaxial modulus and the yield stress of the host Si are reduced significantly from the corresponding values in the crystalline phase to those of amorphous Li_xSi

(See section 4.2.1 for more details). During nucleation of the (100) oriented Si, the concentration of Li ahead of the phase boundary is very small ($c < 0.1$). Consequently, the plastic strains are zero in the crystalline phase and the stresses remain below the elastic limit ($x/H > 0.15$ in figure 4.9b). However, behind the phase boundary the stress and strain are equal to the flow stress and plastic strain corresponding to the equilibrium concentration of α -Li_xSi. The sharp change in the plastic strain at the phase boundary causes a compressive peak in the stress at the phase boundary (the locations are labeled with pink arrows in Fig. 4.9b). This peak in the stress continues to advance as the phase boundary propagates inside Si. Similar peaks are observed during lithiation of the (110)-oriented Si (the peaks are labeled with pink arrows in Fig. 4.9d). Larger mobility in the $\langle 110 \rangle$ direction allows larger concentrations of Li to diffuse deeper inside the bulk material. The accumulation of this large concentration of Li induces plastic stresses ahead of the phase boundary ($x/H > 0.15$ in figure 4.9d). Moreover, mobility dominates the time of nucleation in these samples. The smaller mobility of Li in the (100) direction slows the diffusion of Li and results in higher accumulation of Li at the surface, i.e. the concentration at the surface of (100) reaches the spinodal point at an earlier time ($0.05 < t < 0.07$ hr) than the (110) oriented Si ($0.07 < t < 0.12$ hr).

Representative plots of the chemical potential, concentration, stress, and plastic strain profiles during lithiation of {110} oriented Si at constant current density of $20 \mu\text{A}/\text{cm}^2$ ($0.2 < t < 7.7$ hr), constant voltage of 120 mV ($12.7 < t < 17.7$ hr), and constant voltage of 100 mV ($22.7 < t < 27.7$ hr) are shown in Fig. 4.10. To facilitate comparisons between the two Si orientations, snapshots of the chemical potential, concentration, stress, and plastic strain profiles inside {100} oriented Si during galvanostatic lithiation at a current density of $20 \mu\text{A}/\text{cm}^2$ ($0.2 < t < 7.7$ hr), potentiostatic at a voltage of 100 mV ($12.7 < t < 17.7$ hr), and potentiostatic at a voltage of 80 mV ($22.7 < t < 27.7$ hr) are provided in Fig. 4.11. The plots are overlaid in figure 4.16 in the appendix. During the

galvanostatic lithiation, flux is constant. According to Eq. 4.6, the slope of the chemical potential in the lithiated layer is also constant and proportional to the flux divided by the Li mobility. At the interface, the concentration-gradient dependence of the mobility leads to the discontinuity observed in the chemical potential (See Figs. 4.10a and 4.11a). From Eq. 4.18, the jump in the chemical potential at the interface is equal to $\frac{j\chi}{2M_0}$. Substituting the values corresponding to χ and M_0 from our calibrations, we conclude that during galvanostatic lithiation at each current density, the jump in the chemical potential in the $\langle 100 \rangle$ direction is about 2.7 times that in the $\langle 110 \rangle$ direction. This relation is also seen in figures 4.10a and 4.11a. Larger jumps in the chemical potential are expected during the potentiostatic lithiation steps which apply larger currents to the surface of anode.

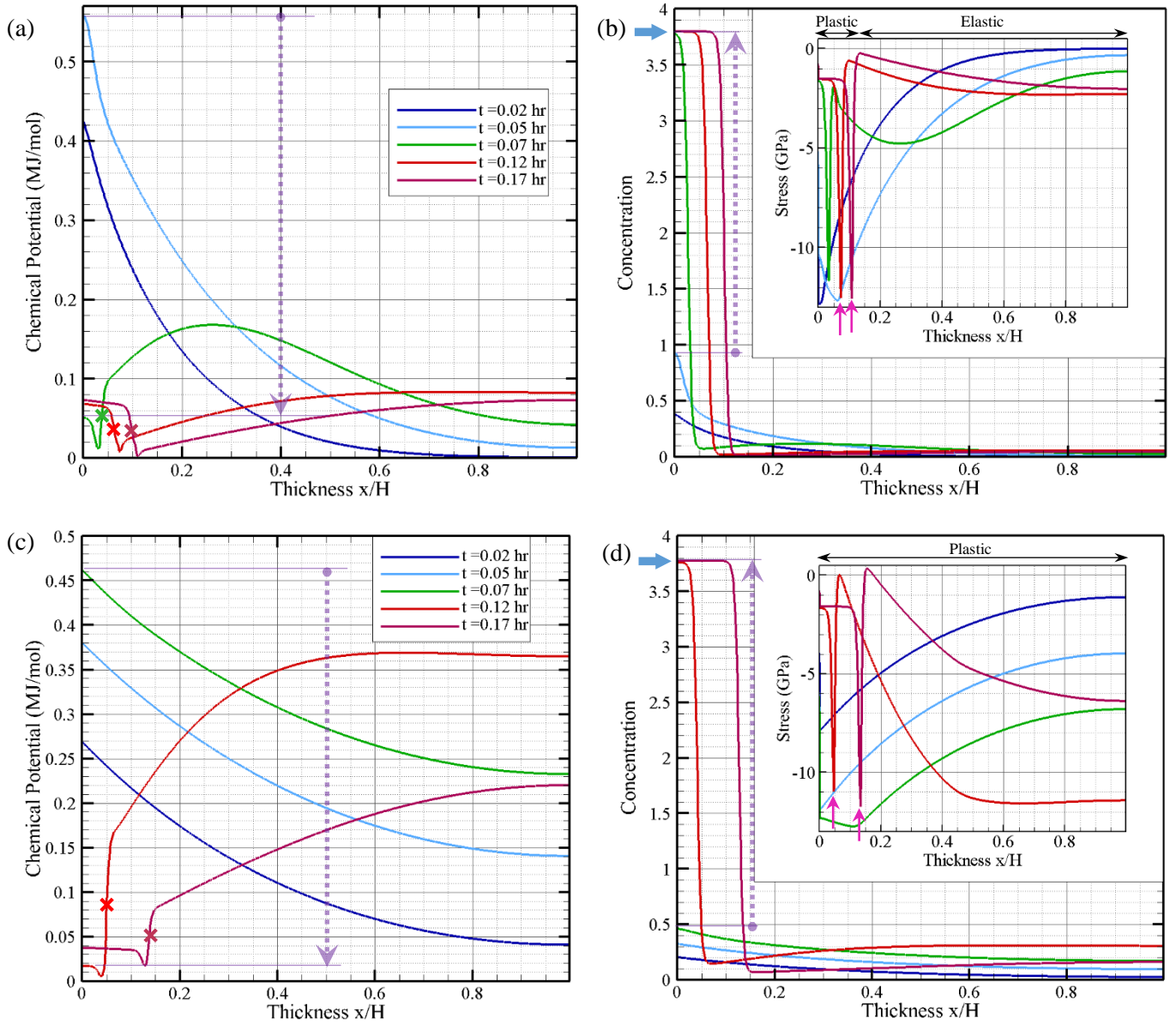


Figure 4.9. Evolution in the (a, c) chemical potential, (b, d) concentration and stress profiles before ($t \leq 0.07$) and after nucleation during lithiation of Si normal to the $\{100\}$ (a, b) and $\{110\}$ (c, d) orientations. The dashed-purple arrows show the jump happening in the chemical potential and concentration near the surface of Si upon nucleation. The blue arrows mark the equilibrium concentration in the $a\text{-Li}_x\text{Si}$ layer. The compressive peaks in the stress at the phase boundary are pointed with pink arrows in (b) and (d). The elastic and plastic regions are indicated at time $t = 0.17$ hr in (b) and (d). The position of the phase boundary at different times is marked with crosses on the chemical potential profiles in (a) and (c).

During potentiostatic lithiation, the flux starts from higher values and decreases with time; the slope of the chemical potential profile varies accordingly. During the second potentiostatic lithiation, a lower voltage is applied to the surface of Si compared to the preceding steps. This induces a higher concentration of Li at the surface and leads to a larger chemical potential (due to the increase in $\frac{d\psi_0}{dc}$) compared to other steps (See Figs. 4.10a and 4.11a). The slightly smaller Li mobility in the $\langle 100 \rangle$ direction causes a higher concentration build-up behind the phase boundary and slightly higher values of chemical potential than those observed in the $\langle 110 \rangle$ direction. The concentration profiles in Fig. 4.10b and 4.11b display the spinodal decomposition imposed by the homogeneous double-well free energy function; with the concentration behind the phase boundary at the equilibrium value of $\text{Li}_{3.75}\text{Si}$ and that ahead of the phase boundary at the equilibrium concentration of pure Si. The propagation of the phase boundary profiles with time gives the velocity of the reaction front with different lithiation processes. Figures 4.10 and 4.11, (c) and (d), display the evolution in the stresses and strains. The bulk materials in the amorphized and crystalline regions show almost constant stresses of c.a. -1.50 and -0.75 GPa, respectively. Chon et al.³⁹ reported a compressive stress of about 0.5 GPa in the amorphous $\text{Li}_{3.5}\text{Si}$ layer using a wafer curvature measurement technique during lithiation of Si wafers. Bucci et al.¹⁵ used a combination of experiments and computation to determine the stresses developed during de/lithiation of *a*-Si thin films. They reported compressive biaxial stress values between 1.5 and 0.5 GPa depending on the charging conditions. Our results match well with these reports on the stresses developed during first cycle lithiation of Si.

Due to higher mobility of Li in the $\{110\}$ direction, the concentration of Li increases, leading to a larger compressive stress inside the electrode before nucleation. Therefore, larger amount of Li is extracted from the regions ahead of the nucleation core and an initial tensile stress is observed in

the stress profiles of {110} oriented Si. The plastic strain profiles (Fig. 4.11d) show that these regions are beyond the elastic limit. No plasticity is detected ahead of the phase boundary in the {100} direction (Fig. 4.10d).

In this section, we explored the nucleation and phase transformation due to diffusion of Li in Si with different crystallographic orientations. Our modified Cahn-Hilliard model can successfully predict the kinetics, mechanics, and thermodynamics during this alloying reaction. Insertion of Li at the surface, increases the concentration up to the lower spinodal point ($c = 0.8$) when a sudden spinodal decomposition happens; the concentration and chemical potential behind the phase boundary jump to the values corresponding to the α -Li_xSi phase, while ahead of the phase boundary the values corresponding to the c -Si phase are retrieved. The interface mobility parameter induces a discontinuity in the chemical potential at the phase boundary. The stress in the lithiated layer stays constant at -1.5 GPa that is determined by the flow stress corresponding to the equilibrium concentration of the α -Li_xSi layer. The large gradient in the plastic strain at the interface creates a compressive peak in the stresses at the phase boundary. Smaller mobility of Li normal to the (100) planes compared to the (110) planes, localizes the Li accumulation at the surface of the (100)-oriented Si and expedites the nucleation. On the other hand, larger mobility in the $\langle 110 \rangle$ direction increases the Li concentration at longer distances from the surface that arises plastic stresses in those regions.

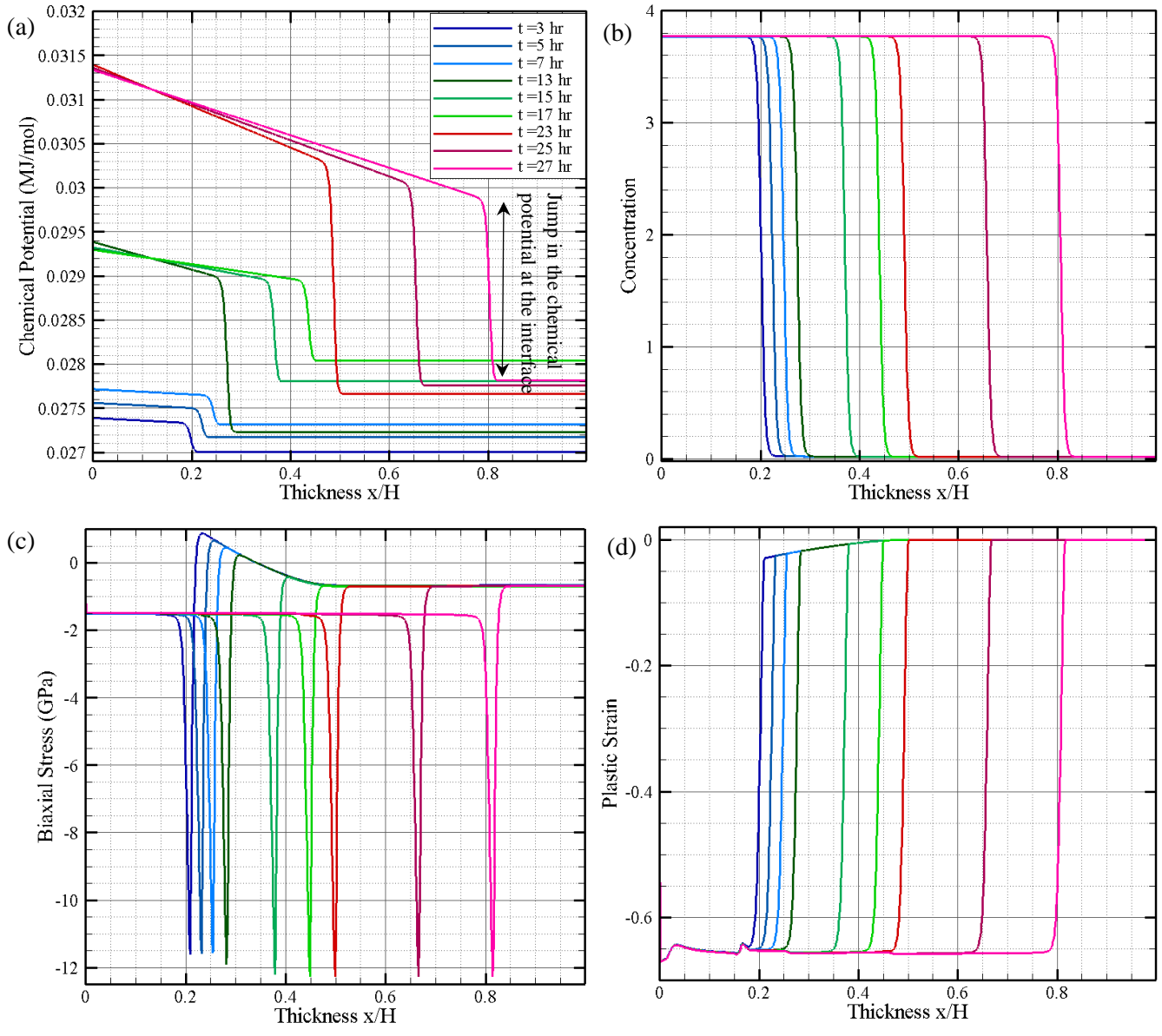


Figure 4.10. The evolution in (a) chemical potential, (b) concentration, (c) biaxial stress, and (d) plastic strain at different stages of lithiation of Si wafer with (110) orientation. Snapshots during galvanostatic $0.2 < t < 7.7$ hr, first potentiostatic $12.7 < t < 17.7$ hr at 0.12 V, and second potentiostatic $22.7 < t < 27.7$ hr at 0.1 V are shown in blue, green, and red colors, respectively.

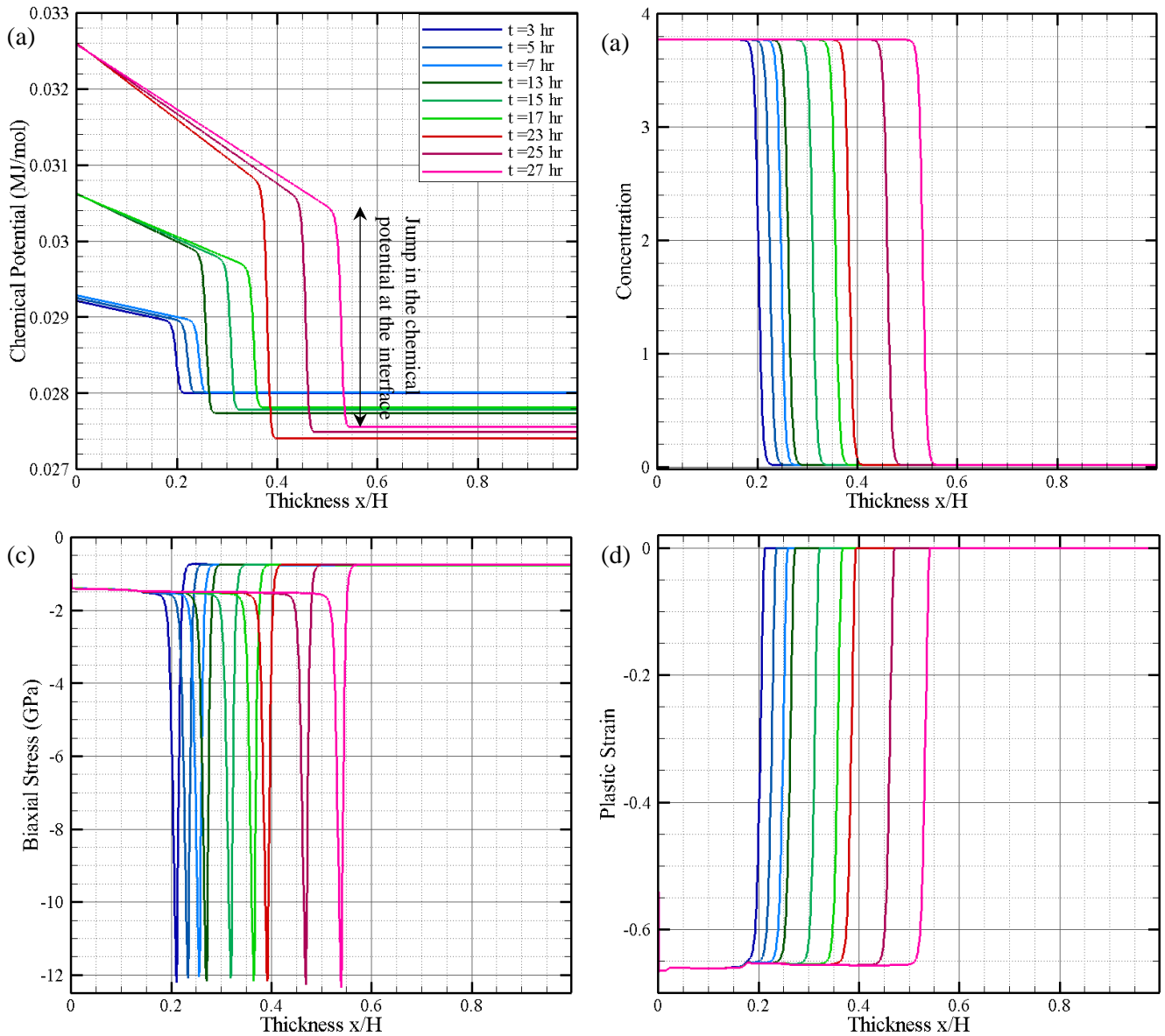


Figure 4.11. The evolution in (a) chemical potential, (b) concentration, (c) biaxial stress, and (d) plastic strain at different stages of lithiation of Si wafer with (100) orientation. Snapshots during galvanostatic $0.2 < t < 7.7$ hr, first potentiostatic $12.7 < t < 17.7$ hr at 0.12 V, and second potentiostatic $22.7 < t < 27.7$ hr at 0.1 V are shown in blue, green, and red colors, respectively.

4.3.5. Variations in the model parameters

In this section we examine the effect of variations in the model parameters on its prediction for the behavior of the system. Accordingly, the rationale behind the choice of the interface thickness is explained. The effect of different combinations of the exchange current density and the interface mobility parameter on the electrochemical response is established and the predictions of the model for the electrochemical and mechanical behaviors are investigated using various viscoplastic parameters. The results are compared with the experimental observations and the sensitivity of the model to changes in the parameters is analyzed.

4.3.5.1. *Interface gradient energy coefficient (κ)*

This term is directly dependent on the thickness of the interface and determines the sharpness of the interface between *c*-Si and *a*-Li_xSi. The larger the value of κ , the interface becomes more diffuse. Past works employing high resolution transmission electron microscopy (HRTEM) to measure the thickness of the interface reported a thickness of about 1 nm^{39, 54}. As shown in figure 4.12, we have examined interface thicknesses of 1, 3, 10, and 20 nm which correspond to κ values of 2.54, 22.90, 254.44, 1017.73 $\mu\text{m}^2\text{J/mol}$. Changes in κ do not show significant modulation in the predictions for the electrochemical or mechanical fields. However, thinner interfaces come with

larger computational costs. Therefore, we have chosen an interface thickness of 3 nm for our simulations.

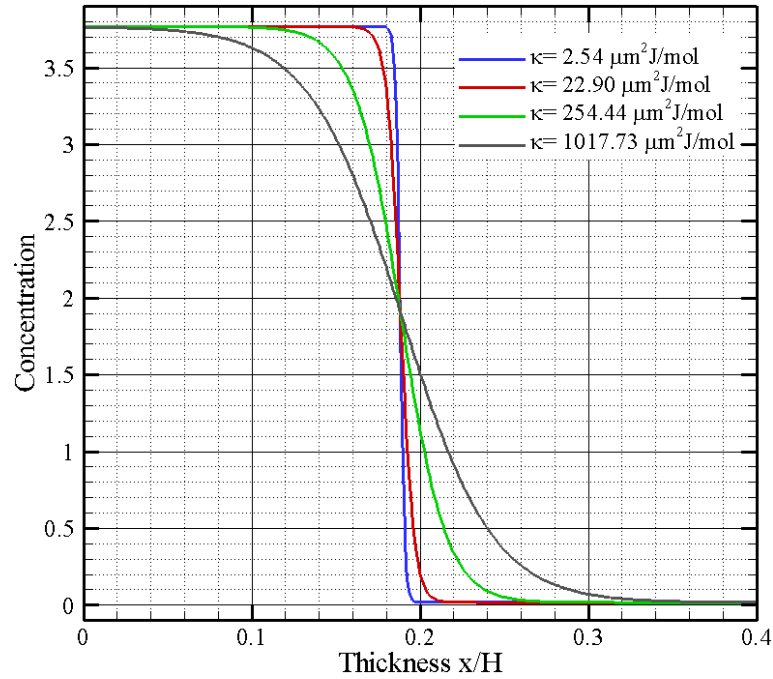


Figure 4.12. Effect of kappa on the sharpness of the interface.

4.3.5.2. Interface mobility and exchange current density

The relation between the exchange current density (i_0) and the interface mobility parameter (χ) is governed by equation 4.32. We used the experimental results from galvanostatic lithiation of Si samples to find the extrema of these parameters (See section 4.3.2 For more details). However, our analysis did not separate the effects of these parameters. The phase transformation in the Li-Si system is controlled by the rate of reactions at the interface^{54, 59}. Therefore, we introduced large resistivities to the motion of the phase boundary in our simulation by choosing χ close to its maximum value. The exchange current density is subsequently determined by substituting χ in Eq.

4.32. Figure 4.13 shows an examination of the effect of i_0 and χ on the prediction of the model for the electrochemical response of the (100) oriented Si during lithiation. Changing these parameters does not have a significant influence on the voltage evolution during galvanostatic lithiation, however, approaching the interface-controlled limit (larger i_0 and χ) leads to improved matching of the voltage profile during open-circuit measurements and the evolution in the current profiles during the potentiostatic step. The peak current observed after the voltage step is related to the charging of the double-layer at the interface of the electrode and electrolyte. The magnitude of this peak in the experimental results is significantly influenced by the response time of the potentiostat. For computational purposes, imposing a sudden jump causes an instability in the solution. Therefore, we did not try to capture the peak current in this study. The small hump in the current after the initial peak corresponds to a supersaturation in the layers close to the surface of the electrode. Levi et al.¹³⁵ explained that propagation of the new phase happens after this hump in the current.

4.1.1.1. *Effect of stress*

Bucci et al.¹⁵ used a viscoplastic model to calibrate their experimental stress measurements on the stresses developed in Si thin films during charge/discharge cycles. It was shown that the flow stress in Si is weakly strain rate dependent. To study the rate dependent plasticity used in our model, we compared the results with varying stress exponents ($m=50$ and 100) and strain rate for plastic flow ($\dot{\epsilon}_0 = 6.4 \times 10^{-10}$ and 6.4×10^{-9}) with those obtained by ignoring the contribution of the stresses in the chemical potential and our experimental results (Fig. 4.14 and 4.15). As is seen in Fig. 4.14, changing the strain rate does not have significant influence on the model's prediction for the

electrochemical response. Smaller stress exponents lead to a closer agreement with the experimental data during the open-circuit measurements. Evidently, removing the contribution of the stresses leads to large discrepancies from the experimental measurements. Without the effect of stresses, the model ceases to capture the characteristic hump in the current profile after the initial peak in the potentiostatic lithiation step. Lack of rate dependence also hinders the voltage from rising appreciably during the open-circuit step.

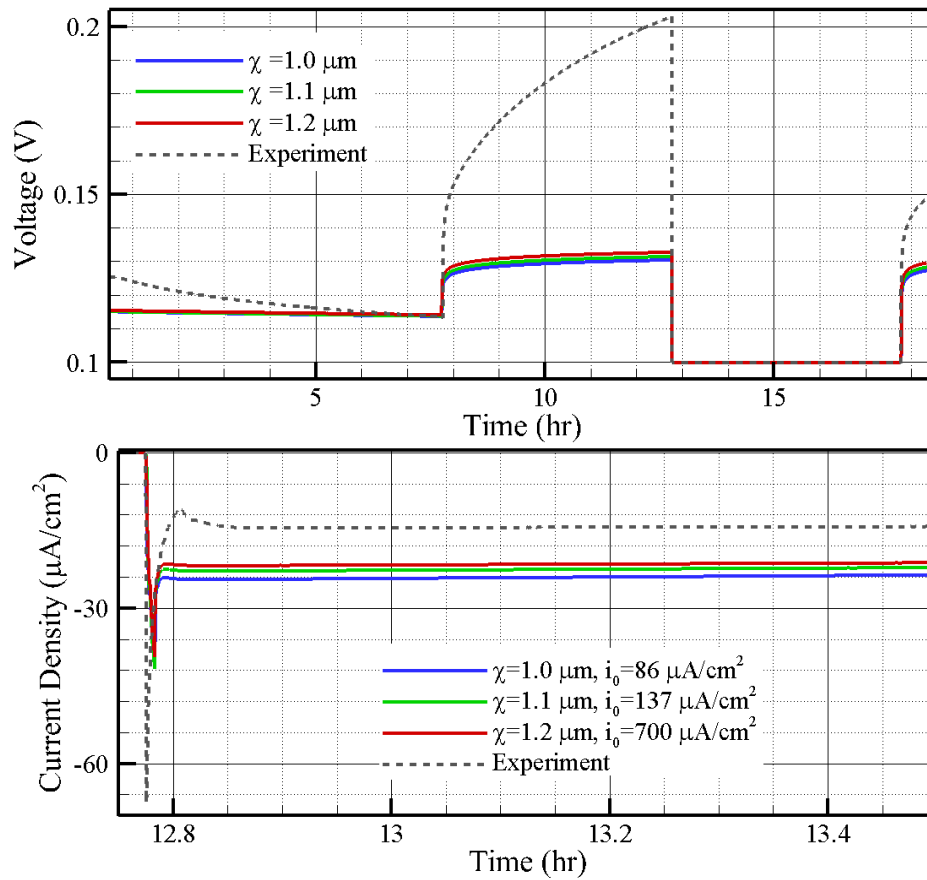


Figure 4.13. Effect of the interface-mobility parameter and exchange current density on the prediction of the model for the electrochemistry of lithiation and comparison with the experimental measurements. (a) voltage profiles during the galvanostatic, first open-circuit, and first potentiostatic (voltage=0.1V) measurements and (b) current density profile during the first potentiostatic lithiation (voltage=0.1V). The experimental results are shown with dashed lines.

Figure 4.15a shows the effect of the stress parameters on the chemical potential inside the electrode at a specific time ($t = 1.5$ hr) during galvanostatic lithiation. Adding the effect of stress increases the magnitude of the chemical potential. It must be noted that comparing the location of the phase boundary between the plots with/without stresses is not valid. We expect compressive stresses to decelerate the influx of lithium and the propagation of the phase boundary. In the no-stress case, smaller currents are needed for nucleation and initial phase propagation before the galvanostatic step and that leads to slower propagation during the very first step of nucleation. The effect of the viscoplastic parameters on the stress peak at the interface is examined in Fig. 4.15b. As discussed before, the stresses are not significantly rate dependent. Increasing the rate sensitivity exponent and the reference strain rate leads to smaller compressive stresses (Fig. 4.15b) and plastic strains (Fig. 4.15c).

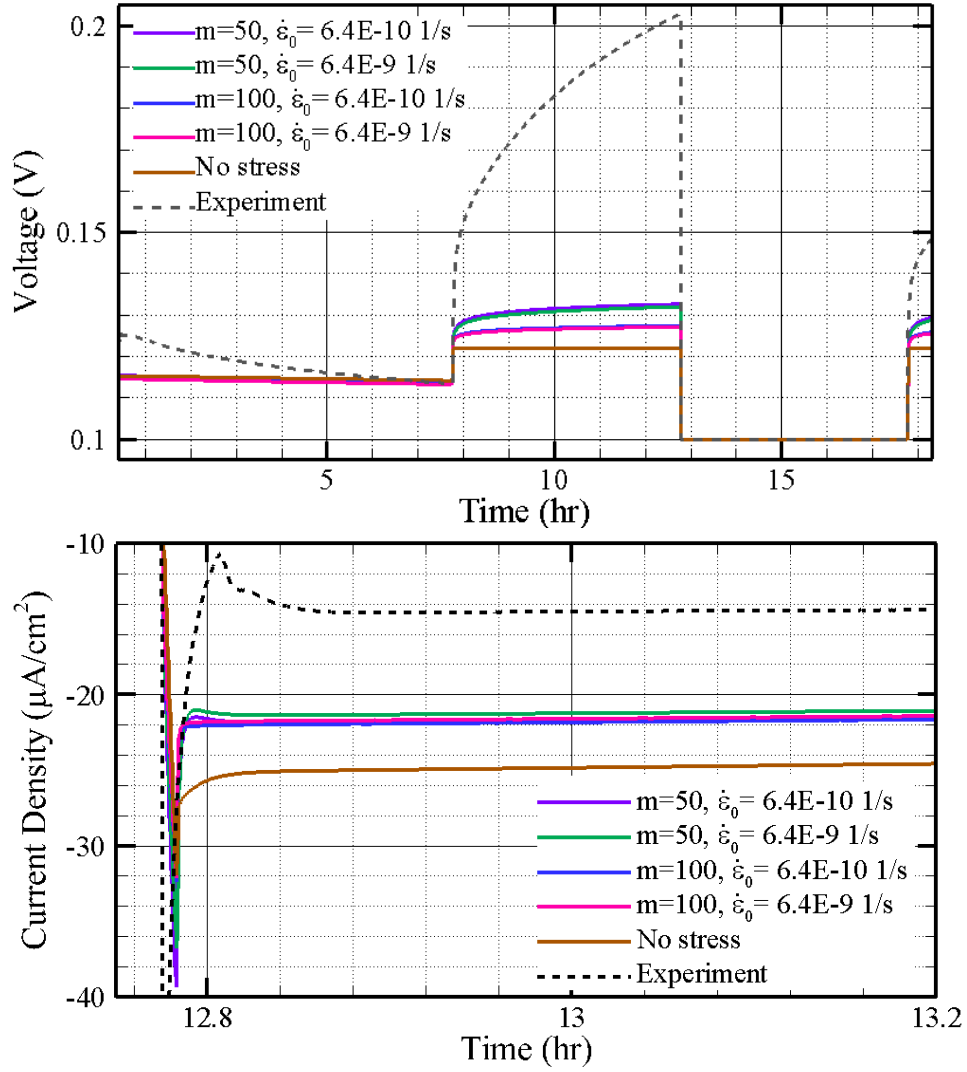


Figure 4.14. Effect of stress and viscoplastic parameters on the prediction of the model for the changes in (a) the voltage profiles during the galvanostatic lithiation and the first open circuit measurement and (b) the current density profiles during the first potentiostatic lithiation with Voltage=0.1 V. Experimental measurements are shown in dashed lines.

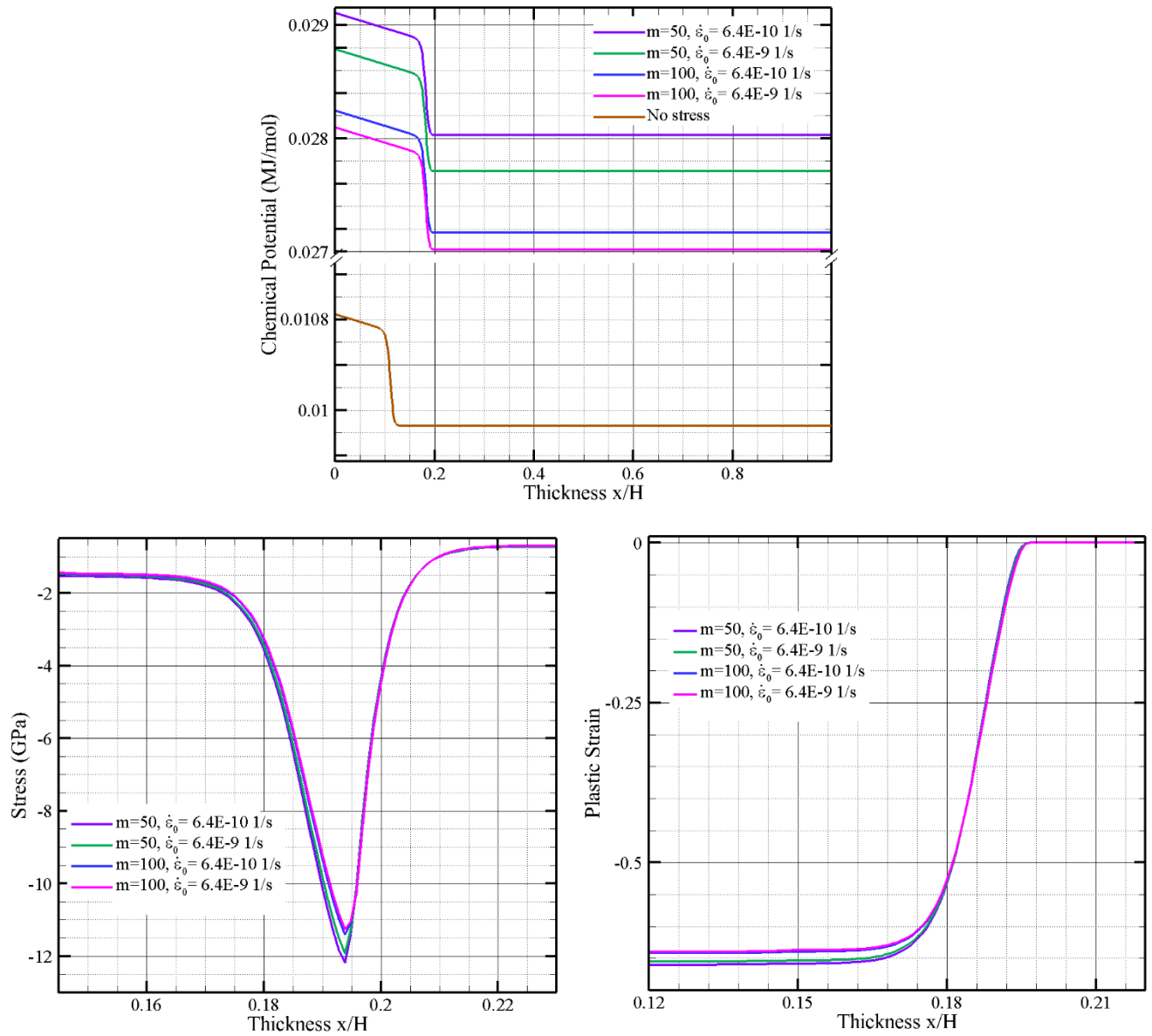


Figure 4.15. Effect of stress exponent and plastic strain rate on (a) the chemical potential, (b) the biaxial stress, and (c) the plastic strain. All the snapshots are taken during the galvanostatic lithiation at $t=1.5$ hr.

4.3.6. Energy dissipation in the cell

The modified Cahn-Hilliard model includes the role of interface in the phase transforming behavior. Phase boundary propagation is accompanied by dissipation and energy loss due to internal resistance to the motion of the interface. The interface mobility parameter in our model accounts for such resistance. From Eqs. 4.14 and 4.20, the energy dissipation at the interface due to phase propagation and the dissipation in the bulk due to diffusion are described by

$$\dot{U}_{int} = -A \left[\frac{(j^+ + j^-)^2}{2K_1} + \frac{(j^+ - j^-)^2}{2K_2} \right]$$

$$\dot{U}_{bulk} = -A \int_0^H \frac{j^2}{M_0} dx - A \left[\int_0^a f(\sigma, c) \frac{\partial j}{\partial x} dx + \int_a^H f(\sigma, c) \frac{\partial j}{\partial x} dx \right]$$

During galvanostatic lithiation at a constant flux j , we have $j = 0$ for $x > a$, $j^+ = 0$, and $j^- = j$.

The gradient of flux in the bulk is zero. Therefore, it can be shown that

$$\dot{U}_{int} = -\frac{Aj^2}{2} \left[\frac{1}{K_1} + \frac{1}{K_2} \right] \tag{4.38}$$

$$\dot{U}_{bulk} = -Aa \frac{j^2}{M_0} \tag{4.39}$$

Conservation of energy in isothermal condition requires that the changes in Helmholtz free energy (Ψ) is equal to or smaller than the stress power

$$\dot{\Psi} \leq \frac{\dot{U}}{AH} + \frac{1}{\rho H} \left(\int_0^H \underline{\sigma} : \dot{\underline{\varepsilon}} dx \right) = \frac{\dot{U}}{AH} + \frac{1}{\rho H} \left(\int_0^H \underline{\sigma}_d : \dot{\underline{\varepsilon}}^p dx + \int_0^H \underline{\sigma} : \dot{\underline{\varepsilon}}^e dx \right) \quad (4.40)$$

where $\underline{\sigma}_d$ is the deviatoric part of the stress tensor. The elastic behavior of solid is described by the Helmholtz free energy,

$$\dot{\Psi} = \frac{1}{\rho H} \int_0^H \underline{\sigma} : \dot{\underline{\varepsilon}}^e dx \quad (4.41)$$

and, dissipation must always be positive

$$\frac{\dot{U}}{AH} + \frac{1}{\rho H} \left(\int_0^H \underline{\sigma}_d : \dot{\underline{\varepsilon}}^p dx \right) \geq 0 \quad (4.42)$$

The deviatoric stress tensor and the plastic strain rate are calculated as follows

$$\underline{\sigma}_d = \underline{\sigma} - \frac{1}{3} tr(\underline{\sigma}) \underline{I} = \frac{1}{3} \sigma \begin{pmatrix} -2 & 0 & 0 \\ 0 & 1 & 0 \\ 0 & 0 & 1 \end{pmatrix} \quad (4.43)$$

$$\dot{\underline{\varepsilon}}^p = \overline{\begin{pmatrix} -2 \ln(\lambda^p) & 0 & 0 \\ 0 & \ln(\lambda^p) & 0 \\ 0 & 0 & \ln(\lambda^p) \end{pmatrix}} = \frac{\dot{\lambda}^p}{\lambda^p} \begin{pmatrix} -2 & 0 & 0 \\ 0 & 1 & 0 \\ 0 & 0 & 1 \end{pmatrix} \quad (4.44)$$

So, $\underline{\sigma}_d : \dot{\underline{\varepsilon}}^p = 2\sigma \frac{\dot{\lambda}^p}{\lambda^p} = 2\sigma \dot{\varepsilon}^p$. With the interface at $x=a$, the dissipation Eq. 4.42 can be written as

$$\frac{1}{\rho H} \left(\int_0^H 2\sigma \dot{\varepsilon}^p dx \right) + \frac{j^2}{2H} \left[\frac{1}{K_1} + \frac{1}{K_2} \right] + a \frac{j^2}{HM_0} \geq 0 \quad (4.45)$$

Using equation 4.5 and considering constant stress values of σ_a and σ_c with associated yield stresses $\sigma_{0,a}$ and $\sigma_{0,c}$ in the bulk material of a -Li_xSi and c -Si, respectively, we can write,

$$\frac{\dot{\varepsilon}_0}{\rho H} \left[-a\sigma_a \left(\frac{|\sigma_a|}{\sigma_{0,a}} - 1 \right)^m - (H-a)\sigma_c \left(\frac{|\sigma_c|}{\sigma_{0,c}} - 1 \right)^m \right] + \frac{j^2}{2H} \left[\frac{1}{K_1} + \frac{1}{K_2} \right] + a \frac{j^2}{HM_0} \geq 0 \quad (4.46)$$

The interface moves from 0 to H during lithiation and the velocity of the phase boundary is given by $v = j/\Delta c$. Integrating the dissipation over time for a modified Cahn-Hilliard case gives

$$-\frac{H\Delta c \dot{\varepsilon}_0}{2\rho j} \left[\sigma_a \left(\frac{|\sigma_a|}{\sigma_{0,a}} - 1 \right)^m + \sigma_c \left(\frac{|\sigma_c|}{\sigma_{0,c}} - 1 \right)^m \right] + \frac{j\Delta c}{M_0} \left(\frac{\chi}{3} + \frac{H}{2} \right) \geq 0 \quad (4.47)$$

So, in the absence of the stresses and with electrode thicknesses smaller than $\frac{2}{3}\chi$, the energy dissipation due to the interface dominates that due to the bulk diffusion. In our calibrated model if χ is larger than its critical value $\chi_c = \frac{3H}{2} \left\{ -\frac{M_0 \dot{\varepsilon}_0}{\rho j^2} \left[\sigma_a \left(\frac{|\sigma_a|}{\sigma_{0,a}} - 1 \right)^m + \sigma_c \left(\frac{|\sigma_c|}{\sigma_{0,c}} - 1 \right)^m \right] + 1 \right\}$, then the interface has a significant energy dissipation compared to other mechanisms. Based on the parameters calibrated and predicted using our model, at a current density of 20 $\mu\text{A}/\text{cm}^2$, the critical value for the interface mobility is about 1.5 μm for both of the orientations. Therefore, the energy dissipation at the interface in the $\{110\}$ direction, and the energy dissipation due to plasticity in the $\{100\}$ direction must be taken into account during phase transformation in the Li-Si system.

4.3.7. Rate-limiting processes during the lithiation of Si

Identifying the rate limiting processes in batteries is an important consideration for designing the charge/discharge cycles. We can define three competing timescales during lithiation based on the modified Cahn-Hilliard model:

$$\tau_{bulk\ diffusion} = \frac{\rho H^2}{\sigma M_0}; \quad \tau_{plastic\ flow} = \frac{1}{\dot{\epsilon}_0}; \quad \tau_{interface\ reaction} = \frac{\chi}{v}; \quad \tau_{surface\ reaction} \propto \frac{1}{i_0}$$

The value of the parameters in different systems determines the rate limiting mechanism. In the case where the bulk diffusion and interface reaction have the same timescales, we can find the critical value of the interface mobility parameter, $\chi_c = \frac{\rho v H^2}{\sigma M_0}$. The effect of interfacial mobility must be included in the electrochemical response of the system if $\chi > \chi_c$. According to our simulations, the critical interface mobilities for the <100> and <110> directions are 17.5 and 4.2 nm, respectively. These values are much smaller than the associated interface mobility values (1.2 and 2.06 μm). Hence, the phase propagation in the Li-Si system is controlled by the reactions at the interface rather than the diffusion in the bulk. Comparison between the timescales for the reaction at the interface and the plastic flow reveals that the plastic strain is happening at a more extended timescale.

4.2. Conclusions

In this study, we have used a modified Cahn-Hilliard model for a moving phase boundary to investigate the kinetics, thermodynamics, and mechanics of the phase boundary propagation in crystalline silicon anodes due to diffusion of lithium. A double-well homogeneous free-energy function regulates the nucleation and phase separation behavior of the phase field model. We have included the contribution of the mechanical stress and plastic strains inside the electrode using a viscoplastic constitutive law and utilized the Butler-Volmer kinetics for insertion of Li at the surface. The model is calibrated through numerical simulations, analytical calculations, and experimental data. The observed behavior suggests that

- (i) the mobility of Li in Li_xSi is about 8.8×10^{-21} and $4.2 \times 10^{-20} \frac{\text{m}^2 \cdot \text{mol}}{\text{J} \cdot \text{s}}$ normal to the {100} and {110} orientations, respectively;
- (ii) the average voltage during galvanostatic charging at different current densities relates the exchange current density and the interface mobility. This relation and the transient and long-term evolution of current during potentiostatic lithiation determines the values of i_0 and χ for lithium insertion at the surface/interfaces normal to the {100} and {110} crystallographic orientations of Si.
- (iii) the simulated results for the velocity of the phase boundary propagation along different crystallographic directions for potentiostatic hold at several voltages and galvanostatic lithiations at multiple current densities match well with previous experimental observations.

- (iv) the evolution of the chemical potential, concentration, stresses, and the plastic strains before and after nucleation and the effect of the spinodal decomposition agree well with the theoretical expectations. During the phase boundary propagation, the chemical potential and concentration ahead of the phase boundary stay at the values corresponding to the lower minimum in the free energy. Behind the phase boundary these quantities jump to the values corresponding to the minimum in the free energy in the lithiated phase ($c \sim 3.75$).
- (v) the stresses in the amorphized and crystalline Si remain almost constant during phase propagation at about -1.50 and -0.75 GPa, respectively.
- (vi) the jump in the plastic strain at the phase boundary – from negative values in the lithiated layer to zero in the crystalline phase – causes a jump in the stresses at the phase boundary.

The effect of changes in the model parameters are studied and the behavior is compared with the cases where the stresses are excluded and the experimental measurements. These comparisons prove that the phase propagating reaction of Li and Si is highly interface controlled and confirm the critical effect of stresses in the electrochemical response of the system. Additionally, the effect of the interface-mobility parameter in the dissipation of energy at the interface and the rate of phase propagation in battery cells are discussed. In the Li-Si system, interface mobility has a significant contribution in the dynamics of the reaction.

we used a double-well free-energy potential and a concentration-gradient dependent mobility to model the phase boundary propagation including the Li insertion at the surface, phase nucleation, phase boundary kinetics, Li diffusion in the bulk, and the mechanical fields. This approach is helpful in qualitative analysis of problems dealing with phase transformation due to diffusion. The

difference in our results from the experimental observations calls for future development of a more accurate phase-field model of the electrochemical evolution in Li ion batteries that can better explain the phase propagation characteristics at the interface and in the bulk material.

4.3. Appendix

4.3.1. Derivation of Cahn-Hilliard formulation

This section provides a brief introduction to the phase field modeling approaches as described by Boettinger et al.¹²⁰

The free energy functional F must decrease in every process. Assuming an isothermal situation,

$$F = \int \left[\psi_0(\phi, c, T) + \frac{\kappa_c^2}{2} |\nabla c|^2 + \frac{\kappa_\phi^2}{2} |\nabla \phi|^2 \right] dV \quad (4.48)$$

with ϕ the phase field, c the concentration, κ_ϕ and κ_c the associated gradient energy coefficients, T the temperature, and $\psi_0(\phi, c, T)$ the free energy density. The phase field and concentration are non-conserved and conserved quantities, respectively.

This free energy functional is minimized at equilibrium, so that $\frac{\delta F}{\delta \phi} = 0$ and $\frac{\delta F}{\delta c} = \text{constant}$. In dynamic systems, the total free energy must decrease with time. The equations that satisfy this criterion are

$$\frac{\partial \phi}{\partial t} = -M_\phi \left[\frac{\partial \psi_0}{\partial \phi} - \kappa_\phi^2 \nabla^2 \phi \right] \quad (4.49)$$

$$\frac{\partial c}{\partial t} = \nabla \cdot \left[M_c \nabla \left(\frac{\partial \psi_0}{\partial c} - \kappa_c^2 \nabla^2 c \right) \right] \quad (4.50)$$

where M_ϕ and M_c are the mobilities related to the interface kinetics and diffusion in the bulk, respectively. The first equation is called the Allen-Cahn equation and the second one is the Cahn-Hilliard equation. A non-zero gradient energy coefficient with a double-well energy density function can model a spinodal decomposition. The terms $\left(\frac{\partial \psi_0}{\partial c} - \kappa_c^2 \nabla^2 c \right)$ represent the chemical potential during the diffusion. Langer and Sekerka¹²⁸ used Eq. 4.49 to describe the interface motion.

4.3.2. Finite element implementation for the model equations

Given ε_n , ε_n^p , and $\sigma_{0,n}$ at time t_n , $\varepsilon_{n+1} = \varepsilon_n + \Delta \varepsilon$ and $t_{n+1} = t_n + \Delta t$, the task is to determine σ_{n+1} , $\sigma_{0,n+1}$, and ε_{n+1}^p .

$$c_{n+1} = c_n + \Delta c \quad (4.51)$$

$$\sigma_{0,n+1} = s_0 + s_1 \ln(1 + s_2 c_{n+1}) \quad (4.52)$$

$$\varepsilon_{n+1}^p = \varepsilon_n^p + \Delta t \dot{\varepsilon}_{n+1}^p \quad (4.53)$$

A backward Euler (implicit) scheme gives:

$$\begin{aligned} \sigma_{n+1} &= \sigma_n + \left[\frac{\partial \sigma_{n+1}}{\partial c} \Delta c + \frac{\partial \sigma_{n+1}}{\partial t} \Delta t \right] \\ \sigma_{n+1} &= B(c_{n+1})(\varepsilon_{n+1} - \varepsilon_n^p - \Delta t \dot{\varepsilon}_{n+1}^p) \\ \dot{\varepsilon}_{n+1}^p &= \frac{\dot{\varepsilon}_0}{2} \left(\frac{|\sigma_{n+1}|}{\sigma_{0,n+1}} - 1 \right)^m \frac{|\sigma_{n+1}|}{\sigma_{n+1}} \\ \varepsilon_{n+1} &= -\frac{1}{3} \ln(1 + \beta c_{n+1}) \end{aligned} \quad (4.54)$$

Combining the above equations, we have

$$\sigma_{n+1} = \sigma_n + \left\{ B \frac{\partial}{\partial c} \left(\frac{1}{B} \right) \sigma_n - B \frac{\beta}{3(1+\beta c_{n+1})} \right\} \Delta c - B \Delta t \frac{\dot{\varepsilon}_0}{2} \left(\frac{|\sigma_{n+1}|}{\sigma_{0,n+1}} - 1 \right)^m \frac{|\sigma_{n+1}|}{\sigma_{n+1}} \quad (4.55)$$

Solving for σ_{n+1} using the Newton-Raphson method:

$$\begin{aligned} f &= \sigma_{n+1} - \sigma_n - B \left[\left\{ \frac{\partial}{\partial c} \left(\frac{1}{B} \right) \sigma_n - \frac{\beta}{3(1+\beta c_{n+1})} \right\} \Delta c - \Delta t \frac{\dot{\varepsilon}_0}{2} \left(\frac{|\sigma_{n+1}|}{\sigma_{0,n+1}} - 1 \right)^m \frac{|\sigma_{n+1}|}{\sigma_{n+1}} \right] \\ \frac{df}{d\sigma_{n+1}} &= 1 + B m \Delta t \frac{\dot{\varepsilon}_0}{2} \left(\frac{|\sigma_{n+1}|}{\sigma_{0,n+1}} - 1 \right)^{m-1} \frac{1}{\sigma_{0,n+1}} \frac{|\sigma_{n+1}|}{\sigma_{n+1}} \\ ds &= -\frac{f}{df/d\sigma_{n+1}} \end{aligned} \quad (4.56)$$

Then update all the variables

$$\sigma_{n+1} = \sigma_n + ds$$

$$\varepsilon_{n+1}^p = \varepsilon_n^p + \Delta t \frac{\dot{\varepsilon}_0}{2} \left(\frac{|\sigma_{n+1}|}{\sigma_{0,n+1}} - 1 \right)^m \frac{|\sigma_{n+1}|}{\sigma_{n+1}}$$

$$\varepsilon_{n+1}^e = -\frac{1}{3} \ln(1 + \beta c_{n+1}) - \varepsilon_{n+1}^p \quad (4.57)$$

Expressing the governing equation for the chemical potential (Eq. 4.8) in a weak form

$$\int_0^H \mu \delta\mu \, dx = \int_0^H \frac{d\psi_0}{dc} \delta\mu + \kappa \frac{dc}{dx} \frac{d\delta\mu}{dx} - \left[\frac{\sigma^2}{\rho} \frac{\partial}{\partial c} \left(\frac{1}{B} \right) + \frac{2\sigma}{3\rho} \frac{\beta}{1+\beta c} \right] \delta\mu \, dx \quad (4.58)$$

And, introducing interpolation functions $\delta\mu = N^a \delta\mu^a$ and $\mu \rightarrow \mu + \Delta\mu$, $c \rightarrow c + \Delta c$, the residual will have the form:

$$R_a^\mu = \int_0^H \left(\mu + \Delta\mu - \frac{d\psi_0}{dc} + \left[\frac{\sigma^2}{\rho} \frac{\partial}{\partial c} \left(\frac{1}{B} \right) + \frac{2\sigma}{3\rho} \frac{\beta}{1+\beta c} \right] \right) N^a - \kappa \frac{d(c+\Delta c)}{dx} \frac{dN^a}{dx} \, dx = 0 \quad (4.59)$$

On the other hand, we have Eq. 4.9 for the balance of species $\frac{\partial c}{\partial t} = \frac{\partial}{\partial x} M \frac{\partial \mu}{\partial x}$. Converting it to a weak

form, taking into account the boundary conditions at $x = 0$, $J = -M \frac{\partial \mu}{\partial x}$, and at $x = H$, $\frac{\partial \mu}{\partial x} = 0$.

$$\int_0^H \frac{\partial c}{\partial t} \delta c = - \int_0^H M \frac{\partial \mu}{\partial x} \frac{\partial \delta c}{\partial x} \, dx + M \frac{\partial \mu}{\partial x} \delta c \Big|_0^H = - \int_0^H M \frac{\partial \mu}{\partial x} \frac{d\delta c}{dx} \, dx + J \delta c(0) \quad (4.60)$$

Adopting a semi-implicit time integration scheme, $\frac{\Delta c}{\Delta t} = (1 - \theta)f(c, t) + \theta f(c + \Delta c, t + \Delta t)$.

$0 < \theta < 1$ (we have used $\theta = 0.75$ to maintain the stability of the solution) and $\delta c = N^a \delta c^a$

(keeping the interpolation for c and μ the same), the second residual equation will be

$$R_a^c = \int_0^H \frac{\Delta c}{\Delta t} N^a + M \frac{\partial(\mu + \theta \Delta \mu)}{\partial x} \frac{\partial N^a}{\partial x} dx - J N^a(0) = 0 \quad (4.61)$$

The following equation must be solved to get the stiffness components ($K_{ab}^{c\mu}$)

$$R_a^c(c + \Delta c, \mu + \Delta \mu) = R_a^c(c, \mu) + \frac{\partial R_a^c}{\partial c^b} \Delta c^b + \frac{\partial R_a^c}{\partial \mu^b} \Delta \mu^b = 0 \quad (4.62)$$

Substitute $\mu, c, \Delta \mu, \Delta c$ with interpolations of the form $\mu = N^b \mu^b$ and differentiate w.r.t μ^b or c^b

($K_{ab}^{c\mu} = \frac{\partial R_a^c}{\partial \mu^b}$) as appropriate to build all the equations necessary for solving for the incremental

degrees of freedom ($\Delta \mu^a, \Delta c^a, \Delta \mu^b, \Delta c^b$)

$$\begin{bmatrix} K_{aa}^{\mu\mu} & K_{aa}^{\mu c} & K_{ab}^{\mu\mu} & K_{ab}^{\mu c} \\ K_{aa}^{c\mu} & K_{aa}^{cc} & K_{ab}^{c\mu} & K_{ab}^{cc} \\ K_{ab}^{\mu\mu} & K_{ab}^{\mu c} & K_{bb}^{\mu\mu} & K_{bb}^{\mu c} \\ K_{ab}^{c\mu} & K_{ab}^{cc} & K_{bb}^{c\mu} & K_{bb}^{cc} \end{bmatrix} \begin{pmatrix} \Delta \mu^a \\ \Delta c^a \\ \Delta \mu^b \\ \Delta c^b \end{pmatrix} = - \begin{pmatrix} R_a^\mu \\ R_a^c \\ R_b^\mu \\ R_b^c \end{pmatrix} \quad (4.63)$$

With the following definitions:

$$K_{ab}^{\mu\mu} = \int_0^H N^a N^b dx$$

$$K_{ab}^{\mu c} = \int_0^H \left(-\frac{d^2\psi_0}{dc^2} + \frac{\partial}{\partial c} \left[\frac{\sigma^2}{\rho} \frac{\partial}{\partial c} \left(\frac{1}{B} \right) + \frac{2\sigma}{3\rho} \frac{\beta}{1+\beta c} \right] \right) N^a N^b - \kappa \frac{dN^a}{dx} \frac{dN^b}{dx} dx$$

$$K_{ab}^{c\mu} = \int_0^H \theta M \frac{\partial N^a}{\partial x} \frac{\partial N^b}{\partial x} dx$$

$$K_{ab}^{cc} = \int_0^H \frac{1}{\Delta t} N^a N^b dx$$

Total degrees of freedom are defined as $\begin{pmatrix} \mu^a \\ c^a \\ \mu^b \\ c^b \end{pmatrix}$. Also, define **B**, **P**, and **D** matrices as

$$\mathbf{B} = \begin{bmatrix} N^a & 0 & N^b & 0 \\ \frac{dN^a}{dx} & 0 & \frac{dN^b}{dx} & 0 \\ 0 & N^a & 0 & N^b \\ 0 & \frac{dN^a}{dx} & 0 & \frac{dN^b}{dx} \end{bmatrix}$$

$$\mathbf{P} = \begin{bmatrix} \mu + \Delta\mu - \frac{d\psi_0}{dc} + \left[\frac{\sigma^2}{\rho} \frac{\partial}{\partial c} \left(\frac{1}{B} \right) + \frac{2\sigma}{3\rho} \frac{\beta}{1+\beta c} \right] \\ -\kappa \frac{d(c+\Delta c)}{dx} \\ \frac{\Delta c}{\Delta t} \\ M \frac{\partial(\mu+\theta \Delta\mu)}{\partial x} \end{bmatrix}$$

$$\mathbf{D} = \begin{bmatrix} 1 & 0 & -\frac{d^2\psi_0}{dc^2} + \frac{\partial}{\partial c} \left[\frac{\sigma^2}{\rho} \frac{\partial}{\partial c} \left(\frac{1}{B} \right) + \frac{2\sigma}{3\rho} \frac{\beta}{1+\beta c} \right] & 0 \\ 0 & 0 & 0 & -\kappa \\ 0 & 0 & 0 & 0 \\ 0 & \theta M & 1/\Delta t & 0 \end{bmatrix}$$

So that we can build the residual vector $R = \begin{pmatrix} R_a^\mu \\ R_a^c \\ R_b^\mu \\ R_b^c \end{pmatrix} = \mathbf{B}^T \mathbf{P}$ and stiffness matrix $\mathbf{K} = \mathbf{B}^T \mathbf{D} \mathbf{B}$.

Then we will have

$$\mathbf{B} \cdot \begin{pmatrix} \mu^a \\ c^a \\ \mu^b \\ c^b \end{pmatrix} = \begin{pmatrix} \Sigma N^a \mu^a \\ \Sigma N'^a \mu^a \\ \Sigma N^a c^a \\ \Sigma N'^a c^a \end{pmatrix} = \begin{pmatrix} \mu \\ d\mu/dx \\ c \\ dc/dx \end{pmatrix} \quad \text{and} \quad \mathbf{B} \cdot \begin{pmatrix} \Delta \mu^a \\ \Delta c^a \\ \Delta \mu^b \\ \Delta c^b \end{pmatrix} = \begin{pmatrix} \Delta \mu \\ d\Delta \mu/dx \\ \Delta c \\ d\Delta c/dx \end{pmatrix}$$

at each integration point, where $\begin{pmatrix} \mu \\ d\mu/dx \\ c \\ dc/dx \end{pmatrix}$ is the nodal degrees of freedom.

\mathbf{K} , R , and F (force vector) are assembled for all the elements degree of freedoms which yields the standard finite element system of equations $\mathbf{R}(\mathbf{u}) = \mathbf{F}$. It is solved by Newton-Raphson iterations through solving the system of linear equations $\mathbf{K} \Delta u^n = \mathbf{F} - R(u^{n-1})$ where Δu^n is the correction to the degree of freedom vector u^n at the n^{th} iteration.

4.3.3. The evolution of electrochemical and mechanical fields during lithiation of Si wafer with (100) and (110) orientations

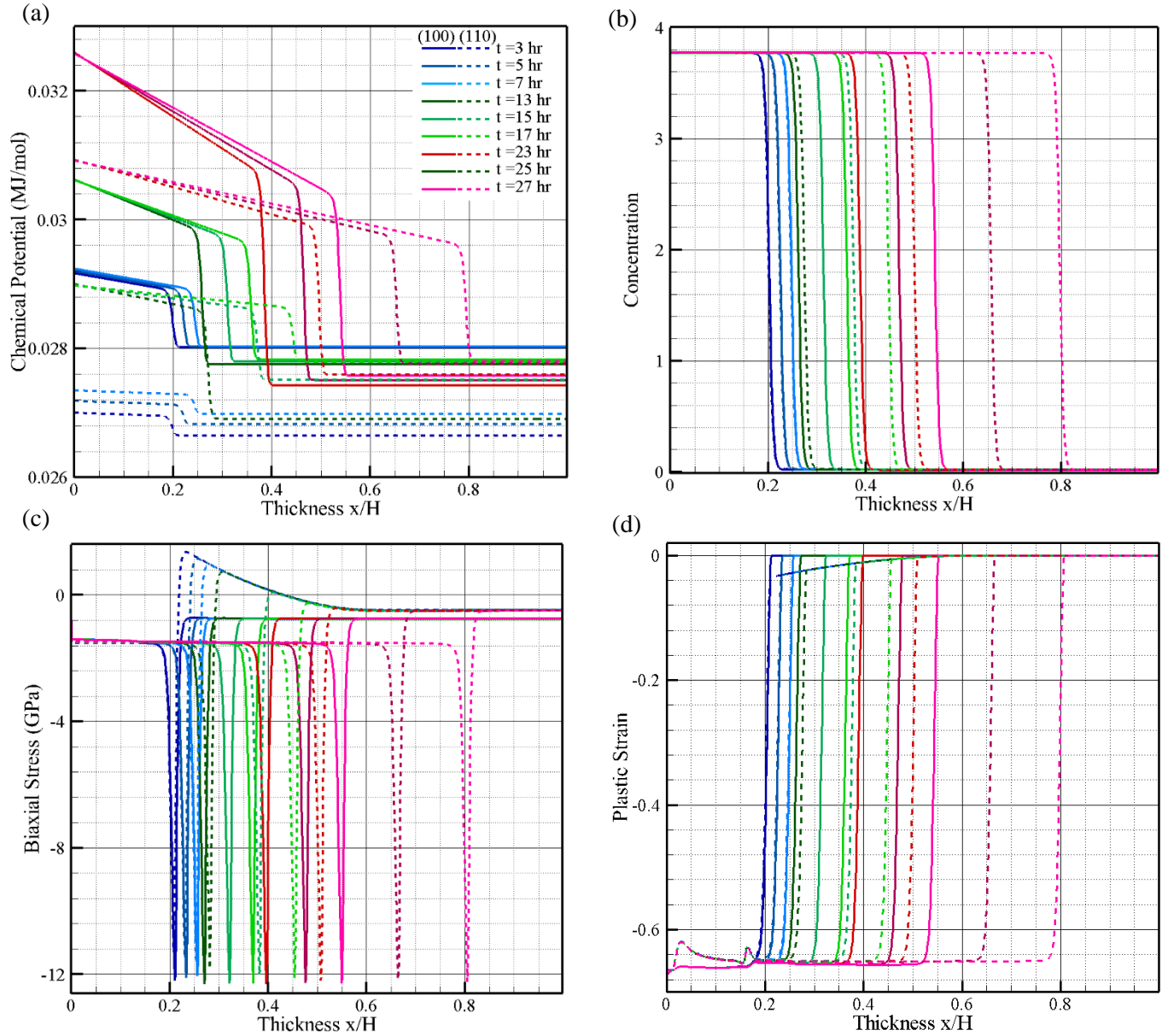


Figure 4.16. The evolution in (a) chemical potential, (b) concentration, (c) biaxial stress, and (d) plastic strain at different stages of lithiation of Si wafer. $\langle 100 \rangle$ and $\langle 110 \rangle$ directions are shown in solid and dashed lines, respectively. Snapshots during galvanostatic $0.2 < t < 7.7$ hr, first potentiostatic $12.7 < t < 17.7$ hr at 0.12 V, and second potentiostatic $22.7 < t < 27.7$ hr at 0.1 V are shown in blue, green, and red colors, respectively.

5. Summary and future works

5.1. Summary

We performed a systematic study on the phase transformation due to Li diffusion during the first cycle lithiation of crystalline Si anodes. Elucidating the kinetics of this binary phase transformation is not possible without precise measurement of the velocity of the phase boundary propagation. We introduced the picosecond ultrasonics technique as an accurate approach for measuring the velocity of the phase boundary propagation during lithiation of crystalline Si. The proper procedure for setting up and aligning the apparatus for conducting PU measurements and the theoretical background including the physics of the generation and detection of acoustic waves are covered. Combination of PU with electrochemical setups are explained in terms of the design of the electrochemical cell, samples, and measurements. We demonstrated the versatility of our method through multiple examples of galvanostatic and potentiostatic lithiation of Si samples with different crystallographic orientations and compared the results with the reported values in the literature. A unique in situ AFM technique for establishing the relationship between the volume expansion and state of charge during lithiation of Si with different crystallographic orientations is also introduced. The results of these experiments led the way for developing and calibrating a modified Cahn-Hilliard type phase-field model of the diffusion of Li in Si. Using this model,

thermodynamics of the phase transformation and mechanical stress and strain fields inside the crystalline Si and amorphous Li_xSi are identified.

The main results of this work are:

- Study of the phase boundary propagation in electrode materials during de/lithiation cycles requires precise characterization of the phase boundary propagation under well-defined electrochemical and kinetic conditions. In situ experiments on simple planar geometries such as single crystalline Si wafers facilitate this necessary requirement.
- We introduced picosecond ultrasonics technique as a non-invasive in situ method with a resolution of about ten nanometers for monitoring the position of the phase boundary between crystalline Si with different crystallographic orientations and the lithiated Si layer.
- The constant current experiments demonstrated constant velocity of phase boundary propagation regardless of the crystallographic orientation which confirmed the linear relation between the flux and the velocity of the phase boundary. During constant potential experiments, the dissimilarity of the thermodynamics of lithiation through different crystallographic orientations of Si dictates different driving forces at the phase boundary. The higher velocity of the phase boundary propagation along the $\langle 110 \rangle$ direction compared to other crystallographic directions supports the reported experimental and computational observations on the lithiation of Si micro/nanostructures^{54, 59, 64, 83}.
- We devised in situ AFM experiments for measuring the volumetric strains during lithiation of Si samples with different crystallographic orientations. These experiments eliminated the contribution of the SEI thickness through specific sample design. The measurements demonstrated that regardless of the kinetics of the phase propagation, the volume expansion

of fully lithiated $a\text{-Li}_x\text{Si}$ depends on the concentration of Li provided at the surface during cycling.

- We carefully established the thermodynamics, kinetics, and mechanics of phase propagation through different crystallographic orientations of Si through calibrating a moving phase boundary problem with our experimental data. The free energy potential, exchange current density of the reactions at the surface, mobility of Li in the $a\text{-Li}_x\text{Si}$ layer, and mobility of the phase boundary are determined for lithiation along different crystallographic directions of Si. Furthermore, the resulting concentration and chemical potential profiles, biaxial stress, and plastic strain are studied during nucleation of the amorphous phase. The behavior of these parameters in the crystalline and amorphous phases and at the phase boundary is characterized during later stages of the phase propagation.

5.2. Future works

The work of this thesis can be continued from both the experimental and computational aspects.

From the experimental point of view, the application of the PU method for investigation of other phase transforming electrode materials including cathodes like LiFePO_4 and anodes such as Ge and Sn can open new windows to the phase transforming mechanisms in Li ion batteries and provide opportunities for optimization of their performance.

Another area of interest would be the study of SEI formation in terms of physical properties including the mass density and thickness in addition to the mechanical properties such as elastic

modulus. Despite being one of the major sources for capacity loss, properties of the SEI is still far from being fully understood. The information from these experiments can pave the way for improving the cyclability of Li ion batteries.

From the computational point of view, extending the phase-field model to incorporate the diffusion of Li into more complicated geometries such as Si particles and nanowires would be an area of interest. Development of 2D and 3D moving phase boundary models facilitate identification of the variations in the materials properties of polycrystalline or multifaceted single crystalline configurations. Using the kinetic parameters from the present study, predictive simulation of such geometries can clarify the reason behind the inhomogeneous volume expansion of Si structures with different crystallographic facets.

References

1. Rezazadeh-Kalehbasti, S.; Liu, L. W.; Maris, H. J.; Guduru, P. R., In Situ Measurement of Phase Boundary Kinetics during Initial Lithiation of Crystalline Silicon through Picosecond Ultrasonics. *J. Experimental Mech.* **2019**.
2. Dahn, J.; Fong, R.; Spoon, M., Suppression of staging in lithium-intercalated carbon by disorder in the host. *Physical Review B* **1990**, *42* (10), 6424.
3. Satoh, A.; Takami, N.; Ohsaki, T., Electrochemical intercalation of lithium into graphitized carbons. *Solid State Ionics* **1995**, *80* (3-4), 291-298.
4. Takami, N.; Satoh, A.; Hara, M.; Ohsaki, T., Structural and kinetic characterization of lithium intercalation into carbon anodes for secondary lithium batteries. *Journal of The Electrochemical Society* **1995**, *142* (2), 371-379.
5. Kasavajjula, U.; Wang, C.; Appleby, A. J., Nano- and bulk-silicon-based insertion anodes for lithium-ion secondary cells. *J. Power Sources* **2007**, *163*, 37.
6. Mukhopadhyay, A.; Sheldon, B. W., Deformation and stress in electrode materials for Li-ion batteries. *Progress in Materials Science* **2014**, *63*, 58-116.
7. Zhang, W.-J., A review of the electrochemical performance of alloy anodes for lithium-ion batteries. *J. Power Sources* **2011**, *196* (1), 13-24.
8. Besenhard, J.; Yang, J.; Winter, M., Will advanced lithium-alloy anodes have a chance in lithium-ion batteries? *Journal of Power Sources* **1997**, *68* (1), 87-90.
9. Nadimpalli, S. P. V.; Sethuraman, V. A.; Dalavi, S.; Lucht, B.; Chon, M. J.; Shenoy, V. B.; Guduru, P. R., Quantifying Capacity Loss due to Solid-Electrolyte-Interphase Layer Formation on Silicon Negative Electrodes in Lithium-ion Batteries. *J. Power Sources* **2012**, *215*, 7.
10. Li, J.; Dahn, J. R., An In Situ X-Ray Diffraction Study of the Reaction of Li with Crystalline Si. *J. Electrochem. Soc.* **2007**, *154* (3), 6.
11. Kim, H.; Seo, M.; Park, M. H.; Cho, J., A critical size of silicon nano-anodes for lithium rechargeable batteries. *Angewandte Chemie International Edition* **2010**, *49* (12), 2146-2149.
12. Chandrasekaran, R.; Magasinski, A.; Yushin, G.; Fuller, T. F., Analysis of Lithium Insertion/Deinsertion in a Silicon Electrode Particle at Room Temperature. *J. Electrochem. Soc.* **2010**, *157* (10), 13.

13. Obrovac, M. N.; Krause, L. J., Reversible Cycling of Crystalline Silicon Powder. *J. Electrochem. Soc.* **2007**, *154* (2), 6.
14. Liu, W.-R.; Guo, Z.-Z.; Young, W.-S.; Shieh, D.-T.; Wu, H.-C.; Yang, M.-H.; Wu, N.-L., Effect of electrode structure on performance of Si anode in Li-ion batteries: Si particle size and conductive additive. *J. power sources* **2005**, *140* (1), 139-144.
15. Bucci, G.; Nadimpalli, S. P. V.; Sethuraman, V. A.; Bower, A. F.; Guduru, P. R., Measurement and modeling of the mechanical and electrochemical response of amorphous Si thin film electrodes during cyclic lithiation. *J. Mech. Phys. Sol.* **2014**, *62*, 23.
16. Sethuramana, V. A.; Chon, M. J.; Shimshak, M.; Srinivasan, V.; Guduru, P. R., In situ measurements of stress evolution in silicon thin films during electrochemical lithiation and delithiation. *J. Power Sources* **2010**, *195*, 5.
17. Kulova, T. L.; Skundin, A. M.; Pleskov, Y. V.; Kon'kov, O. I.; Terukov, E. I.; Trapeznikova, I. N., The Li Insertion/Extraction Characteristics of Amorphous Silicon Thin Films. *Chem. Biochem. Eng. Q.* **2007**, *21* (4), 10.
18. Beaulieu, L. Y.; Hatchard, T. D.; Bonakdarpour, A.; Fleischauer, M. D.; Dahn, J. R., Reaction of Li with Alloy Thin Films Studied by In Situ AFM. *J. Electrochem. Soc.* **2003**, *150* (11), 8.
19. Takamura, T.; Ohara, S.; Uehara, M.; Suzuki, J.; Sekine, K., A vacuum deposited Si film having a Li extraction capacity over 2000 mAh/g with a long cycle life. *J. Power Sources* **2004**, *129* (1), 96-100.
20. Kim, H.; Han, B.; Choo, J.; Cho, J., Three-dimensional porous silicon particles for use in high-performance lithium secondary batteries. *Angewandte Chemie International Edition* **2008**, *47* (52), 10151-10154.
21. Zhao, Y.; Liu, X.; Li, H.; Zhai, T.; Zhou, H., Hierarchical micro/nano porous silicon Li-ion battery anodes. *Chemical Communications* **2012**, *48* (42), 5079-5081.
22. Goldman, J. L.; Long, B. R.; Gewirth, A. A.; Nuzzo, R. G., Strain Anisotropies and Self-Limiting Capacities in Single-Crystalline 3D Silicon Microstructures: Models for High Energy Density Lithium-Ion Battery Anodes. *Advanced functional materials* **2011**, *21*, 11.
23. Szczech, J. R.; Jin, S., Nanostructured silicon for high capacity lithium battery anodes. *Energy & Environmental Science* **2011**, *4* (1), 56-72.
24. Chan, C. K.; Peng, H.; Liu, G.; McIlwrath, K.; Zhang, X. F.; Huggins, R. A.; Cui, Y., High-performance lithium battery anodes using silicon nanowires. *Nat. Nanotechnology* **2008**, *3*, 5.
25. McDowell, M. T.; Lee, S. W.; Ryu, I.; Wu, H.; Nix, W. D.; Choi, J. W.; Cui, Y., Novel Size and Surface Oxide Effects in Silicon Nanowires as Lithium Battery Anodes. *Nano Letters* **2011**.
26. Park, M.-H.; Kim, M. G.; Joo, J.; Kim, K.; Kim, J.; Ahn, S.; Cui, Y.; Cho, J., Silicon nanotube battery anodes. *Nano letters* **2009**, *9* (11), 3844-3847.
27. Cui, L.-F.; Yang, Y.; Hsu, C.-M.; Cui, Y., Carbon-silicon core-shell nanowires as high capacity electrode for lithium ion batteries. *Nano lett.* **2009**, *9* (9), 3370-3374.

28. Wu, H.; Chan, G.; Choi, J. W.; Ryu, I.; Yao, Y.; McDowell, M. T.; Lee, S. W.; Jackson, A.; Yang, Y.; Hu, L., Stable cycling of double-walled silicon nanotube battery anodes through solid–electrolyte interphase control. *Nature nanotechnology* **2012**, *7* (5), 310.
29. Zhou, X.-y.; Tang, J.-j.; Yang, J.; Xie, J.; Ma, L.-l., Silicon@ carbon hollow core–shell heterostructures novel anode materials for lithium ion batteries. *Electrochimica Acta* **2013**, *87*, 663-668.
30. Liu, N.; Wu, H.; McDowell, M. T.; Yao, Y.; Wang, C.; Cui, Y., A yolk-shell design for stabilized and scalable Li-ion battery alloy anodes. *Nano Lett.* **2012**, *12* (6), 3315-3321.
31. Liu, N.; Lu, Z.; Zhao, J.; McDowell, M. T.; Lee, H.-W.; Zhao, W.; Cui, Y., A pomegranate-inspired nanoscale design for large-volume-change lithium battery anodes. *Nature nanotechnology* **2014**, *9* (3), 187.
32. Obrovac, M.; Christensen, L.; Le, D. B.; Dahn, J. R., Alloy design for lithium-ion battery anodes. *Journal of The Electrochemical Society* **2007**, *154* (9), A849-A855.
33. Winter, M.; Besenhard, J. O., Electrochemical lithiation of tin and tin-based intermetallics and composites. *Electrochimica Acta* **1999**, *45* (1-2), 31-50.
34. Tian, H.; Xin, F.; Wang, X.; He, W.; Han, W., High capacity group-IV elements (Si, Ge, Sn) based anodes for lithium-ion batteries. *Journal of Materiomics* **2015**, *1* (3), 153-169.
35. Lee, K.-L.; Jung, J.-Y.; Lee, S.-W.; Moon, H.-S.; Park, J.-W., Electrochemical characteristics of a-Si thin film anode for Li-ion rechargeable batteries. *Journal of Power Sources* **2004**, *129* (2), 270-274.
36. Sethuraman, V. A.; Srinivasan, V.; Newman, J., Analysis of Electrochemical Lithiation and Delithiation Kinetics in Silicon. *J. Electrochem. Soc.* **2013**, *162* (2), 10.
37. Nadimpalli, S. P. V.; Rajasekhar, T.; Sethuraman, V. A., Real-time stress measurements in germanium thin film electrodes during electrochemical Lithiation/Delithiation cycling. *J. Electrochem. Soc.* **2015**, *162* (14), 7.
38. Ui, K.; Kikuchi, S.; Kadoma, Y.; Kumagai, N.; Ito, S., Electrochemical characteristics of Sn film prepared by pulse electrodeposition method as negative electrode for lithium secondary batteries. *Journal of Power Sources* **2009**, *189* (1), 224-229.
39. Chon, M. J.; Sethuraman, V. A.; McCormick, A.; Srinivasan, V.; Guduru, P. R., Real-Time Measurement of Stress and Damage Evolution during Initial Lithiation of Crystalline Silicon. *Phys. Rev. Lett.* **2011**, *107*, 4.
40. Hu, D. M. Z. C. A., Si-Based Anode Materials for Li-Ion Batteries: A Mini Review. *Nano-Micro Letters* **2014**, *6* (4), 12.
41. Lim, L. Y.; Liu, N.; Cui, Y.; Toney, M. F., Understanding phase transformation in crystalline Ge anodes for Li-ion batteries. *Chemistry of Materials* **2014**, *26* (12), 3739-3746.
42. Liu, Y.; Zhang, S.; Zhu, T., Germanium-Based Electrode Materials for Lithium-Ion Batteries. *ChemElectroChem* **2014**, *1* (4), 7.

43. Pharr, M.; Choi, Y. S.; Lee, D.; Oh, K. H.; Vlassak, J. J., Measurements of stress and fracture in germanium electrodes of lithium-ion batteries during electrochemical lithiation and delithiation. *Journal of Power Sources* **2016**, *304*, 164-169.
44. Chen, C.-H.; Chason, E.; Guduru, P. R., Measurements of the Phase and Stress Evolution during Initial Lithiation of Sn Electrodes. *J. Electrochem. Soc.* **2017**, *164* (4), 6.
45. L. Y. Beaulieu, a., * K. W. Eberman,b,** R. L. Turner,b,** L. J. Krause,b, and J. R. Dahna, Colossal Reversible Volume Changes in Lithium Alloys. *Electrochemical and Solid-State Letters* **2001**, *4* (9), 4.
46. Hu, R.; Liu, H.; Zeng, M.; Liu, J.; Zhu, M., Progress on Sn-based thin-film anode materials for lithium-ion batteries. *Chinese Science Bulletin* **2012**, *57* (32), 4119-4130.
47. Ryu, J. H.; Kim, J. W.; Sung, Y.-E.; Oh, S. M., Failure modes of silicon powder negative electrode in lithium secondary batteries. *Electrochemical and solid-state letters* **2004**, *7* (10), 4.
48. Oumellal, Y.; Delpuech, N.; Mazouzi, D.; Dupe, J.; Gaubicher, P.; Moreau, P.; Soudan, P.; Lestriez, B.; Guyomard, D., The failure mechanism of nano-sized Si-based negative electrodes for lithium ion batteries. *J. Mater. Chem.* **2011**, *21*, 8.
49. Yoon, S.; Park, C.-M.; Sohn, H.-J., Electrochemical characterizations of germanium and carbon-coated germanium composite anode for lithium-ion batteries. *Electrochemical and Solid-State Letters* **2008**, *11* (4), A42-A45.
50. Li, X.; Yang, Z.; Fu, Y.; Qiao, L.; Li, D.; Yue, H.; He, D., Germanium anode with excellent lithium storage performance in a germanium/lithium-cobalt oxide lithium-ion battery. *ACS nano* **2015**, *9* (2), 1858-1867.
51. Chia-Yun Choua, G. S. H., On the origin of anisotropic lithiation in crystalline silicon overgermanium: A first principles study. *Applied Surface Science* **2014**, *323*, 4.
52. Hulikal, S.; Chen, C.-H.; Chason, E.; Bower, A. F., Experimental Calibration of a Cahn-Hilliard Phase-Field Model for Phase Transformations in Li-Sn Electrodes. *J. Electrochem. Soc.* **2016**, *163* (13), 13.
53. Zhao, K.; Pharr, M.; Wan, Q.; Wang, W. L.; Kaxiras, E.; Vlassak, J. J.; Suo, Z., Concurrent Reaction and Plasticity during Initial Lithiation of Crystalline Silicon in Lithium-Ion Batteries. *J. Electrochem. Soc.* **2012**, *159* (3), 6.
54. Liu, X. H.; Wang, J. W.; Huang, S.; Fan, F.; Huang, X.; Liu, Y.; Krylyuk, S.; Yoo, J.; Dayeh, S. A.; Davydov, A. V.; Mao, S. X.; Picraux, S. T.; Zhang, S.; Li, J.; Zhu, T.; Huang, J. Y., In situ atomic-scale imaging of electrochemical lithiation in silicon. *Nat. Nanotechnology* **2012**, *7*, 8.
55. Limthongkul, P.; Jang, Y.-I.; Dudney, N. J.; Chiang, Y.-M., Electrochemically-driven solid-state amorphization in lithium-silicon alloys and implications for lithium storage. *Acta Materialia* **2003**, *51*, 11.
56. Wen, C. J.; Huggins, R. A., Chemical diffusion in intermediate phases in the lithium-silicon system. *Journal of solid state chemistry* **1981**, *37* (3), 271-278.

57. Rhodes, K.; Dudney, N.; Lara-Curzio, E.; Daniel, C., Understanding the degradation of silicon electrodes for lithium-ion batteries using acoustic emission. *J. Electrochem. Soc.* **2010**, *157* (12), A1354-A1360.
58. Fan, F.; Huang, S.; Yang, H.; Raju, M.; Datta, D.; Shenoy, V. B.; van Duin, A. C. T.; Zhang, S.; Zhu, T., Mechanical properties of amorphous Li_xSi alloys: a reactive force field study. *Modelling Simul. Mater. Sci. Eng.* **2013**, *21*, 15.
59. Pharr, M.; Zhao, K.; Wang, X.; Suo, Z.; Vlassak, J. J., Kinetics of Initial Lithiation of Crystalline Silicon Electrodes of Lithium-Ion Batteries. *Nano Letters* **2012**, *12*, 9.
60. Lee, S. W.; McDowell, M. T.; Choi, J. W.; Cui, Y., Anomalous Shape Changes of Silicon Nanopillars by Electrochemical Lithiation. *Nano Lett.* **2011**, *11*, 6.
61. Lee, S.; Berla, L. A.; McDowell, M. T.; Nix, W. D.; Cui, Y., Reaction Front Evolution during Electrochemical Lithiation of Crystalline Silicon Nanopillars. *Isr. J. Chem.* **2012**, *52*, 6.
62. An, Y.; Wood, B. C.; Ye, J.; Chiang, Y.-M.; Wang, Y. M.; Tang, M.; Jiang, H., Mitigating mechanical failure of crystalline silicon electrodes for lithium batteries by morphological design. *Phys. Chem. Chem. Phys.* **2015**, *17*, 11.
63. Sethuraman, V. A.; Chon, M. J.; Shimshak, M.; Winkle, N. V.; Guduru, P. R., In situ measurement of biaxial modulus of Si anode for Li-ion batteries. *Electrochem. Communications* **2010**, *12*, 4.
64. Fister, T. T.; Goldman, J. L.; Long, B. R.; Nuzzo, R. G.; Gewirth, A. A.; Fenter, P. A., X-ray diffraction microscopy of lithiated silicon microstructures. *Appl. Phys. Lett.* **2013**, *102*, 4.
65. Cao, C.; Steinrück, H.-G.; Shyam, B.; Stone, K. H.; Toney, M. F., In Situ Study of Silicon Electrode Lithiation with Xray Reflectivity. *Nano Lett.* **2016**, *16*, 7.
66. Seidlhofer, B.-K.; Jerliu, B.; Trapp, M.; Hüger, E.; Risse, S.; Cubitt, R.; Schmidt, H.; Steitz, R.; Ballauff, M., Lithiation of Crystalline Silicon As Analyzed by Operando Neutron Reflectivity. *ACS Nano* **2016**, *10*, 9.
67. Yang, H.; Fan, F.; Liang, W.; Guo, X.; Zhu, T.; Zhang, S., A chemo-mechanical model of lithiation in silicon. *J. Mech. Phys. Sol.* **2014**, *70*, 13.
68. Key, B.; Bhattacharyya, R.; Morcrette, M.; Seznec, V.; Tarascon, J.-M.; Grey, C. P., Real-Time NMR Investigations of Structural Changes in Silicon Electrodes for Lithium-Ion Batteries. *J. Am. Chem. Soc.* **2009**, *131*, 11.
69. Trill, J.-H.; Tao, C.; Winter, M.; Passerini, S.; Eckert, H., NMR investigations on the lithiation and delithiation of nanosilicon-based anodes for Li-ion batteries. *Journal of Solid State Electrochemistry* **2011**, *15* (2), 349-356.
70. Liu, X. H.; Zheng, H.; Zhong, L.; Huang, S.; Karki, K.; Zhang, L. Q.; Liu, Y.; Kushima, A.; Liang, W. T.; Wang, J. W.; Cho, J.-H.; Epstein, E.; Dayeh, S. A.; Picraux, S. T.; Zhu, T.; Li, J.; Sullivan, J. P.; Cumings, J.; Wang, C.; Mao, S. X.; Ye, Z. Z.; Zhang, S.; Huang, J. Y., Anisotropic Swelling and Fracture of Silicon Nanowires during Lithiation. *Nano Letters* **2011**, *11*, 7.

71. Liu, X. H.; Zhong, L.; Huang, S.; Mao, S. X.; Zhu, T.; Huang, J. Y., Size-dependent fracture of silicon nanoparticles during lithiation. *Acs Nano* **2012**, *6* (2), 1522-1531.
72. Di Leo, C. V.; Rejovitzky, E.; Anand, L., A Cahn-Hilliard-type phase-field theory for species diffusion coupled with large elastic deformations: Application to phase-separating Li-ion electrode materials. *J. Mech. Phys. Sol.* **2014**, *70*, 29.
73. Cui, Z.; Gao, F.; Qu, J., Interface-reaction controlled diffusion in binary solids with applications to lithiation of silicon in lithium-ion batteries. *J. Mech. Phys. Sol.* **2013**, *61*, 18.
74. Wan, W.; Zhang, Q.; Cui, Y.; Wang, E., First principles study of lithium insertion in bulk silicon. *J. Phys.: Condensed Matter* **2010**, *22* (41), 415501.
75. Kim, H.; Chou, C.-Y.; Ekerdt, J. G.; Hwang, G. S., Structure and Properties of Li-Si Alloys: A First-Principles Study. *J. Phys. Chem. C* **2011**, *115*, 8.
76. Shenoy, V. B.; Johari, P.; Qi, Y., Elastic softening of amorphous and crystalline Li-Si Phases with increasing Li concentration: A first-principles study. *J. Power Sources* **2010**, *195*, 6.
77. Chan, M. K. Y.; Wolverton, C.; Greeley, J. P., First Principles Simulations of the Electrochemical Lithiation and Delithiation of Faceted Crystalline Silicon. *J. Am. Chem. Soc.* **2012**, *134*, 14362.
78. Zhang, Q.; Cui, Y.; Wang, E., First-principles Approaches to Simulate Lithiation in Silicon electrodes. *Modelling and Simulation in Materials Science and Engineering* **2013**, *21* (7).
79. Zhang, Q.; Zhang, W.; Wan, W.; Cui, Y.; Wang, E., Lithium insertion in silicon nanowires: an ab initio study. *Nano letters* **2010**, *10* (9), 3243-3249.
80. Zhao, K.; Wang, W. L.; Gregoire, J.; Pharr, M.; Suo, Z.; Vlassak, J. J.; Kaxiras, E., Lithium-assisted plastic deformation of silicon electrodes in lithium-ion batteries: a first-principles theoretical study. *Nano letters* **2011**, *11* (7), 2962-2967.
81. Jung, S. C.; Han, Y.-K., Ab initio molecular dynamics simulation of lithiation-induced phase-transition of crystalline silicon. *Electrochimica Acta* **2012**, *62*, 73-76.
82. Dahn, V. L. C. J. R., First Principles Model of Amorphous Silicon Lithiation. *J. Electrochem. Soc.* **2009**, *156* (6), 5.
83. Kim, S.-P.; Datta, D.; Shenoy, V. B., Atomistic Mechanisms of Phase Boundary Evolution during Initial Lithiation of Crystalline Silicon. *J. Phys. Chem. C* **2014**, *118*, 7.
84. Alireza Ostadhossein, a. E. D. C., b Georgios A. Tritsarlis, b Efthimios Kaxiras, Sulin Zhanga and Adri C. T. van Duin, Stress effects on the initial lithiation of crystalline silicon nanowires: reactive molecular dynamics simulations using ReaxFF. *Phys.Chem.Chem.Phys* **2015**, *17*, 9.
85. Zhang, X.; Shyy, W.; Sastry, A. M., Numerical simulation of intercalation-induced stress in Li-ion battery electrode particles. *Journal of the Electrochemical Society* **2007**, *154* (10), A910-A916.
86. McDowell, M. T.; Ryu, I.; Lee, S. W.; Wang, C.; Nix, W. D.; Cui, Y., Studying the kinetics of crystalline silicon nanoparticle lithiation with in situ transmission electron microscopy. *Advanced Materials* **2012**, *24* (45), 6034-6041.

87. Liu, X. H.; Fan, F.; Yang, H.; Zhang, S.; Huang, J. Y.; Zhu, T., Self-limiting lithiation in silicon nanowires. *Acs Nano* **2013**, *7* (2), 1495-1503.
88. Cheng, Y.-T.; Verbrugge, M. W., Diffusion-induced stress, interfacial charge transfer, and criteria for avoiding crack initiation of electrode particles. *J. Electrochem. Soc.* **2010**, *157* (4), A508-A516.
89. Cheng, Y.-T.; Verbrugge, M. W., Evolution of stress within a spherical insertion electrode particle under potentiostatic and galvanostatic operation. *J. Power Sources* **2009**, *190* (2), 453-460.
90. Christensen, J.; Newman, J., Stress generation and fracture in lithium insertion materials. *J. Sol. State Electrochem.* **2006**, *10* (5), 293-319.
91. Ryu, I.; Choi, J. W.; Cui, Y.; Nix, W. D., Size-dependent fracture of Si nanowire battery anodes. *J. Mech. Phys. Sol.* **2011**, *59* (9), 1717-1730.
92. Gao, Y.; Zhou, M., Strong stress-enhanced diffusion in amorphous lithium alloy nanowire electrodes. *J. Appl. Phys.* **2011**, *109* (1), 014310.
93. Bower, A. F.; Guduru, P. R.; Sethuraman, V. A., A finite strain model of stress, diffusion, plastic flow, and electrochemical reactions in a lithium-ion half-cell. *J. Mech. Phys. Sol.* **2011**, *59*, 25.
94. Cui, Z.; Gao, F.; Qu, J., A finite deformation stress-dependent chemical potential and its applications to lithium-ion batteries. *J. Mech. Phys. Sol.* **2012**, *60*, 16.
95. Anand, L., A Cahn–Hilliard-type theory for species diffusion coupled with large elastic–plastic deformations. *J. Mech. Phys. Sol.* **2012**, *60*, 20.
96. Zhao, K.; Pharr, M.; Cai, S.; Vlassak, J. J.; Suo, Z., Large plastic deformation in high-capacity lithium-ion batteries caused by charge and discharge. *J. Am. Ceramic Soc.* **2011**, *94*, s226-s235.
97. Pharr, M.; Suo, Z.; Vlassak, J. J., Measurements of the fracture energy of lithiated silicon electrodes of Li-ion batteries. *Nano letters* **2013**, *13* (11), 5570-5577.
98. Lin, H. N.; Stoner, R. J.; Maris, H. J.; Tauc, J., Phonon attenuation and velocity measurements in transparent materials by picosecond acoustic interferometry. *J. Appl. Phys.* **1991**, *69*, 7.
99. Maris, H., Picosecond Ultrasonics. *Scientific American* **1998**, 4.
100. Miao, Q.; Liu, L.-W.; Grimsley, T. J.; Nurmikko, A. V.; Maris, H. J., Picosecond ultrasonic measurements using an optical mask. *Ultrasonics* **2015**, *56*, 7.
101. Rossignol, C.; Chigarev, N.; Ducouso, M.; Audoin, B.; Forget, G.; Guillemot, F.; Durrieu, M. C., In Vitro picosecond ultrasonics in a single cell. *App. Phys. Lett.* **2008**, *93*, 3.
102. Ducouso, M.; Zouani, O. E.; Chanseau, C.; Chollet, C.; Rossignol, C.; Audoin, B.; Durrieu, M.-C., Evaluation of mechanical properties of fixed bone cells with sub-micrometer thickness by picosecond ultrasonics. *Eur. Phys. J. Appl. Phys.* **2013**, *61* (1), 10.
103. Casset, F.; Devos, A.; Sadtler, S.; Le Louarn, A.; Emery, P.; Le Rhun, G.; Ancey, P.; Fanget, S.; Defaÿ, E., Young modulus and Poisson ratio of PZT thin film by Picosecond Ultrasonics. *2012 IEEE Int. Ultrasonics Symposium Proceedings* **2012**, 4.

104. Mante, P. A.; Robillard, J. F.; Devos, A., Complete thin film mechanical characterization using picosecond ultrasonics and nanostructured transducers: experimental demonstration on SiO₂. *Appl. Phys. Lett.* **2008**, *93*, 3.
105. Msall, M. E.; Wright, O. B.; Matsuda, O., Seeking shear waves in liquids with picosecond ultrasonics. *J. Phys: Conference Series* **2007**, *92*, 4.
106. Thomsen, C.; Grahn, H. T.; Maris, H. J.; Tauc, J., Surface generation and detection of phonons by picosecond light pulses. *Phys. Rev. B* **1986**, *34* (6), 10.
107. EPOXY TECHNOLOGY, I., EPO-TEK302-3M Technical Data Sheet. **2017**.
108. Tim T. Fister, J. L. G., Brandon R. Long, Ralph G. Nuzzo, Andrew A. Gewirth, and Paul A. Fenter, X-ray diffraction microscopy of lithiated silicon microstructures. *Appl. Phys. Lett.* **2013**, *102*, 5.
109. Yoon, I.; Abraham, D. P.; Lucht, B. L.; Bower, A. F.; Guduru, P. R., In Situ Measurement of Solid Electrolyte Interphase Evolution on Silicon Anodes Using Atomic Force Microscopy. *Adv. Energy Mater.* **2016**, *6* (12), 9.
110. Deal, B. E.; Grove, A. S., General Relationship for the Thermal Oxidation of Silicon. *J. Appl. Phys.* **1965**, *36* (12), 9.
111. Astrova, E. V.; Rumyantsev, A. M.; Li, G. V.; Nashchekin, A. V.; Kazantsev, D. Y.; Ber, B. Y.; Zhdanov, V. V., Electrochemical Lithiation of Silicon with Varied Crystallographic Orientation. *Physics of Semiconductor Devices* **2016**, *50*, 7.
112. Kao, D.-B.; McVittie, J. P.; Nix, W. D.; Saraswat, K. C., Two-dimensional thermal oxidation of silicon—I. Experiments. *IEEE Transactions on Electron Devices* **1987**, *34* (5), 1008-1017.
113. Madou, M. J., *Fundamentals of microfabrication: the science of miniaturization*. CRC press: 2002.
114. Choi, Y. S.; Pharr, M.; Oh, K. H.; Vlassak, J. J., A simple technique for measuring the fracture energy of lithiated thin-film silicon electrodes at various lithium concentrations. *J. Power Sources* **2015**, *294*, 159-166.
115. Obrovacz, M. N.; Christensen, L., Structural Changes in Silicon Anodes during Lithium Insertion/Extraction. *Electrochemical and Solid-State Letters* **2004**, *7* (5), 4.
116. Purkayastha, R.; McMeeking, R. M., A Linearized Model for Lithium Ion Batteries and Maps for their Performance and Failure. *Journal of Applied Mechanics* **2012**, *79* (3).
117. Haftbaradaran, H.; Song, J.; Curtin, W.; Gao, H., Continuum and atomistic models of strongly coupled diffusion, stress, and solute concentration. *J. Power Sources* **2011**, *196* (1), 361-370.
118. Huang, S.; Zhu, T., Atomistic mechanisms of lithium insertion in amorphous silicon. *Journal of Power Sources* **2011**, *196* (7), 3664-3668.
119. Cahn, J. W.; Hilliard, J. E., Free Energy of a Nonuniform System. I. Interfacial Free Energy. *J. Chem. Phys.* **1958**, *28* (2), 10.
120. Boettinger, W. J.; Warren, J. A.; Beckermann, C.; Karma, A., Phase-field simulation of solidification. *Annual review of materials research* **2002**, *32* (1), 163-194.

121. Chen, L.-Q., Phase-field models for microstructure evolution. *Annual review of materials research* **2002**, 32 (1), 113-140.
122. Burch, D.; Bazant, M. Z., Size-dependent spinodal and miscibility gaps for intercalation in nanoparticles. *Nano letters* **2009**, 9 (11), 3795-3800.
123. Tang, M.; Huang, H.-Y.; Meethong, N.; Kao, Y.-H.; Carter, W. C.; Chiang, Y.-M., Model for the particle size, overpotential, and strain dependence of phase transition pathways in storage electrodes: application to nanoscale olivines. *Chemistry of Materials* **2009**, 21 (8), 1557-1571.
124. Han, B.; Van der Ven, A.; Morgan, D.; Ceder, G., Electrochemical modeling of intercalation processes with phase field models. *Electrochimica Acta* **2004**, 49 (26), 4691-4699.
125. Singh, G. K.; Ceder, G.; Bazant, M. Z., Intercalation dynamics in rechargeable battery materials: General theory and phase-transformation waves in LiFePO₄. *Electrochimica Acta* **2008**, 53 (26), 7599-7613.
126. Cogswell, D. A.; Bazant, M. Z., Coherency strain and the kinetics of phase separation in LiFePO₄ nanoparticles. *ACS nano* **2012**, 6 (3), 2215-2225.
127. Bai, P.; Cogswell, D. A.; Bazant, M. Z., Suppression of phase separation in LiFePO₄ nanoparticles during battery discharge. *Nano lett.* **2011**, 11 (11), 4890-4896.
128. Langer, J.; Sekerka, R., Theory of departure from local equilibrium at the interface of a two-phase diffusion couple. *Acta Metallurgica* **1975**, 23 (10), 1225-1237.
129. Wan, W.; Zhang, Q.; Cui, Y.; Wang, E., First principles study of lithium insertion in bulk silicon. *J. Phys.: Condensed Matter* **2010**, 22, 9.
130. Newman, J.; Thomas-Alyea, K. E., *Electrochemical systems*. John Wiley & Sons: 2012.
131. Ding, N.; Xu, J.; Yao, Y.; Wegner, G.; Fang, X.; Chen, C.; Lieberwirth, I., Determination of the diffusion coefficient of lithium ions in nano-Si. *Solid State Ionics* **2009**, 180 (2-3), 222-225.
132. Weppner, W.; Huggins, R. A., Determination of the kinetic parameters of mixed-conducting electrodes and application to the system Li₃Sb. *Journal of The Electrochemical Society* **1977**, 124 (10), 1569-1578.
133. Pell, E., Diffusion rate of Li in Si at low temperatures. *Physical Review* **1960**, 119 (4), 1222.
134. Swamy, T.; Chiang, Y.-M., Electrochemical charge transfer reaction kinetics at the silicon-liquid electrolyte interface. *Journal of The Electrochemical Society* **2015**, 162 (13), A7129-A7134.
135. Levi, M. D.; Markevich, E.; Wang, C.; Aurbach, D., Chronoamperometric measurements and modeling of nucleation and growth, and moving boundary stages during electrochemical lithiation of graphite electrode. *J. Electroanalytical Chem.* **2007**, 600, 10.